The search for Low Scale Technicolor in the $Z + \gamma$ channel using 7 TeV ATLAS Data

DISSERTATION

Presented in Partial Fulfillment of the Requirements for the Degree Doctor of Philosophy in the Graduate School of The Ohio State University

By

Matthew Fisher, B.A.

Graduate Program in Physics

The Ohio State University

2012

Dissertation Committee:

Professor Harris Kagan, Advisor

Richard Kass

Junko Shigemitsu

Tom Humanic

ABSTRACT

A search for low scale technicolor (LSTC) particles, ρ_T and ω_T, decaying to a Z boson and a photon with the Z decaying to electrons or muons, is presented. The search was conducted using 4.7 fb^{-1} of 7 TeV data collected by the ATLAS detector at the Large Hadron Collider. Two different sets of LSTC parameters were considered, one was excluded at the 95% confidence level for ρ_T/ω_T masses from 200 GeV to 280 GeV and the other from 200 GeV to 480 GeV. An upper limit is measured for the cross section times branching fraction of any new narrow resonance decaying to the same final state for masses between 200 and 500 GeV. The Standard Model cross section times branching fraction was measured to be $1.26 \pm 0.07(stat.) \pm 0.07(syst.)$ pb when the Z boson decays to electrons and $1.24 \pm 0.07(stat.) \pm 0.11(syst.)$ pb when it decays to muons which is consistent with the theoretical prediciton of $1.22 \pm 0.05(syst.)$ pb.

For Hannah, my Motivator-in-Chief.

VITA

November 13, 1980 ....Born—Goshen, IN

August 2003 ...................................B.A., Goshen College, Goshen, IN

September 2003 to present ....Graduate Teaching/Research Associate, Department of Physics, The Ohio State University

Fields of Study

Major Field: Physics

Table of Contents

List of Figures

viii

List of Tables

Chapter 1

INTRODUCTION

1.1 The Standard Model

The Standard Model of particle physics is the current theory we use to explain the fundamental structure of the universe. It describes all the known fundamental particles and their interactions (except gravity). This theory has been a powerful predictive tool in the past. The bottom and top quarks, as well as the W and Z bosons were predicted first by the theory and later found by high energy experiments. The fundamental particles of the Standard Model (see Figure 1.1) include three generations of leptons: the electron, muon, and tau, in order of increasing mass, as well as their corresponding neutrinos, three generations of quarks: up/down, charm/strange, top/bottom, and the force carriers: the photon, gluon, and W and Z bosons. The Standard Model also describes the forces that govern the interactions between particles: the electromagnetic, weak, and strong forces. Although no experiment has ever shown the SM to be incorrect, there is one piece of the Standard Model that has not yet been observed experimentally: the Higgs boson.

1.1.1 The Higgs boson

The Higgs boson is predicted to exist by the Standard Model, but it's existence has not yet been confirmed. It arises as a consequence of the Higgs mechanism which is perhaps the simplest way to explain spontaneous electroweak symmetry breaking (EWSB). Electroweak symmetry breaking is the process by which the $SU(2)_L \otimes U(1)_Y$ invariance of the electroweak theory is broken down to the $U(1)_{EM}$ subgroup of electromagnetism. EWSB allows the W and Z bosons to have mass while the photon remains massless. Over the last several decades multiple experiments have searched for evidence of its existence. At the CERN e^+e^- collider (LEP) a lower limit on the mass of the Higgs was set at 115 GeV [20]. Experiments at the proton-antiproton collider at Fermilab (Tevatron) have also excluded Higgs masses at the 95% CL in two regions: 100 GeV to 106 GeV, and 147 GeV to 179 GeV [21]. The most recent, and highest energy, collider is the new proton-proton collider at CERN (LHC). The
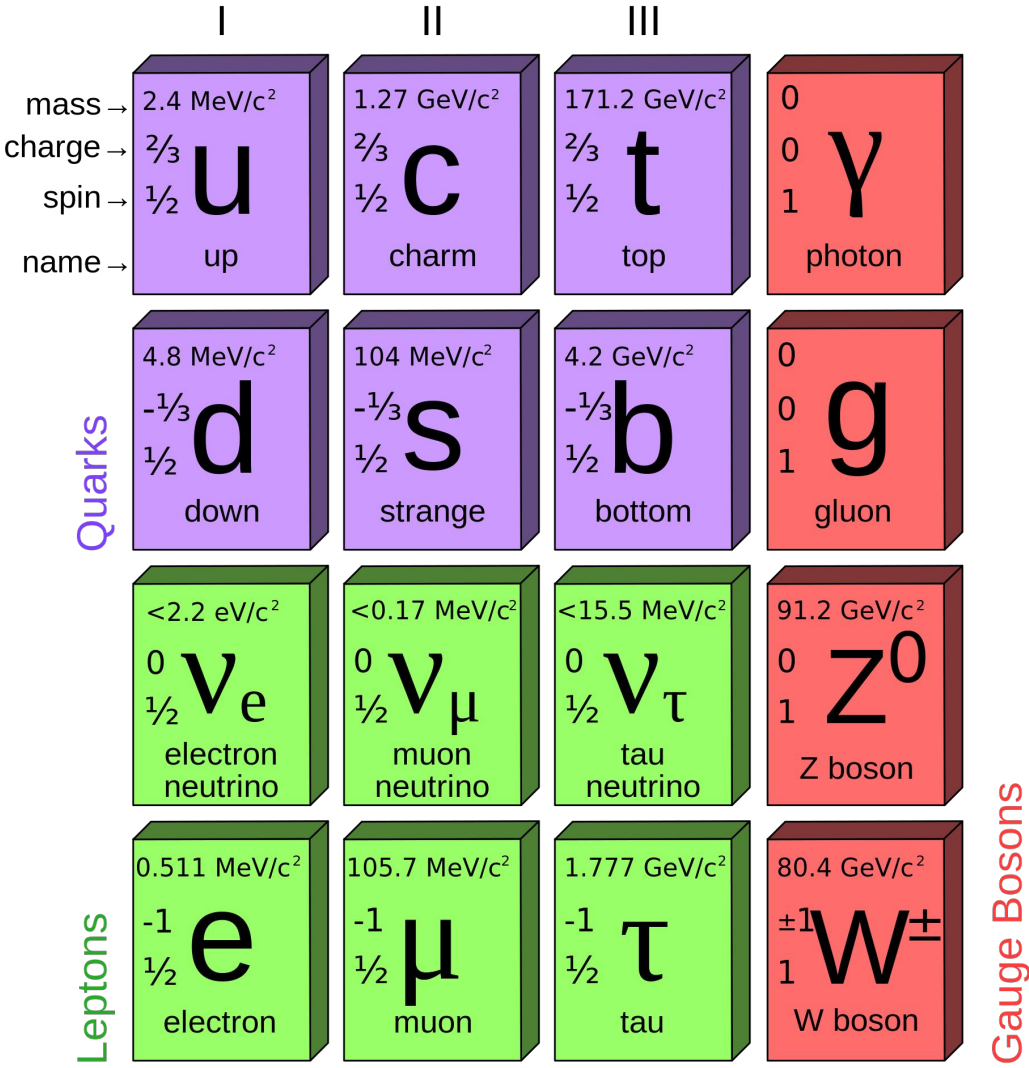
Figure 1.1: Standard Model of particle physics [1].

LHC hosts two experiments that are actively searching for the Higgs, ATLAS and CMS. In December of 2011 the ATLAS experiment published results excluding at the 95% CL a Higgs particle with a mass in the following ranges: 112.9 GeV to 115.5 GeV, 131 GeV to 238 GeV and 251 GeV to 466 GeV. An excess was observed around $\sim$ 126 GeV with a local significance of 3.6σ and a global significance of 2.2σ due to the likelihood to observe a signal of magnitude anywhere in the analyzed region [22]. The CMS experiment excluded a mass range of 127 to 600 GeV at the 95% CL, and reported an excess with a local(global) significance of $3.1\sigma(1.5\sigma)$ at 124 GeV [23].

On July 4 of 2012 CERN announced the observation of a narrow resonance at $\sim$ 126 GeV. The resonance was seen in two channels: decays to two photons as well as decays to two Z bosons which decay leptonically. Although it is still too early to conclude that this is the Standard Model Higgs boson, the measured branching ratios are consistent with the predictions of the Standard Model. ATLAS reports an excess of events near 126.5 GeV with a local significance of 5.0σ and a global significance of 4.6σ [24]. CMS reports a local significance of 5.0σ and global significance of 4.0σ at at a mass of 125.3 GeV [25].

1.1.2 Beyond the Standard Model

Despite the success of the SM, it is not seen as completely satisfactory by many physicists. The Higgs mechanism is not predicted by the theory but is added on to explain the masses of the other SM particles. The masses of the W and Z are on the order of 100 GeV while the Planck mass is of order 10^{19} GeV. This disparity violates the principle of "naturalness" because parameters of the theory must be finely tuned to produce it [26]. If the Higgs boson exists then there will be radiative corrections to its mass that are larger than the mass and need to be cancelled [27]. Theories such as supersymmetry (SUSY) and technicolor attempt to deal with these issues in different ways. Supersymmetry encompasses a wide range of theories where each of the known fundamental particles has a heavier superpartner; the superpartners of bosons are fermions and vice versa. These superpartners can cancel contributions from SM particles to the Higgs boson mass [28]. Technicolor is a theory that accounts for electroweak symmetry breaking without a Higgs boson, instead EWSB is caused by a new strong interaction at a higher energy scale [29]. Both technicolor and SUSY predict the existence of new particles that should be produced at the LHC [30].

1.2 The Large Hadron Collider

The Large Hadron Collider is a particle accelerator and collider located at CERN, the European Organization for Nuclear Research, in Geneva, Switzerland. It is the largest and highest energy proton-proton collider in the world with a circumference of 26 km (see Figure 1.2) and a center of mass collision energy of 7 TeV in 2011 and 8 TeV in 2012, with

a goal of reaching the design energy of 14 TeV by 2018. It was built to collide both protons and atomic nuclei. Since it first turned on it has produced more than 5 fb^{-1} of data at 7 TeV and should produce 15 fb^{-1} of 8 TeV data by the end of 2012. The instantaneous luminosity of the LHC reached a peak of $3.7 \times 10^{33} cm^{-2} s^{-1}$ in 2011. There are four major experiments located at the LHC: ATLAS, CMS, ALICE, and LHCb. Each one is located at a point around the ring where the two counter rotating beams intersect, causing collisions that these experiments detect.
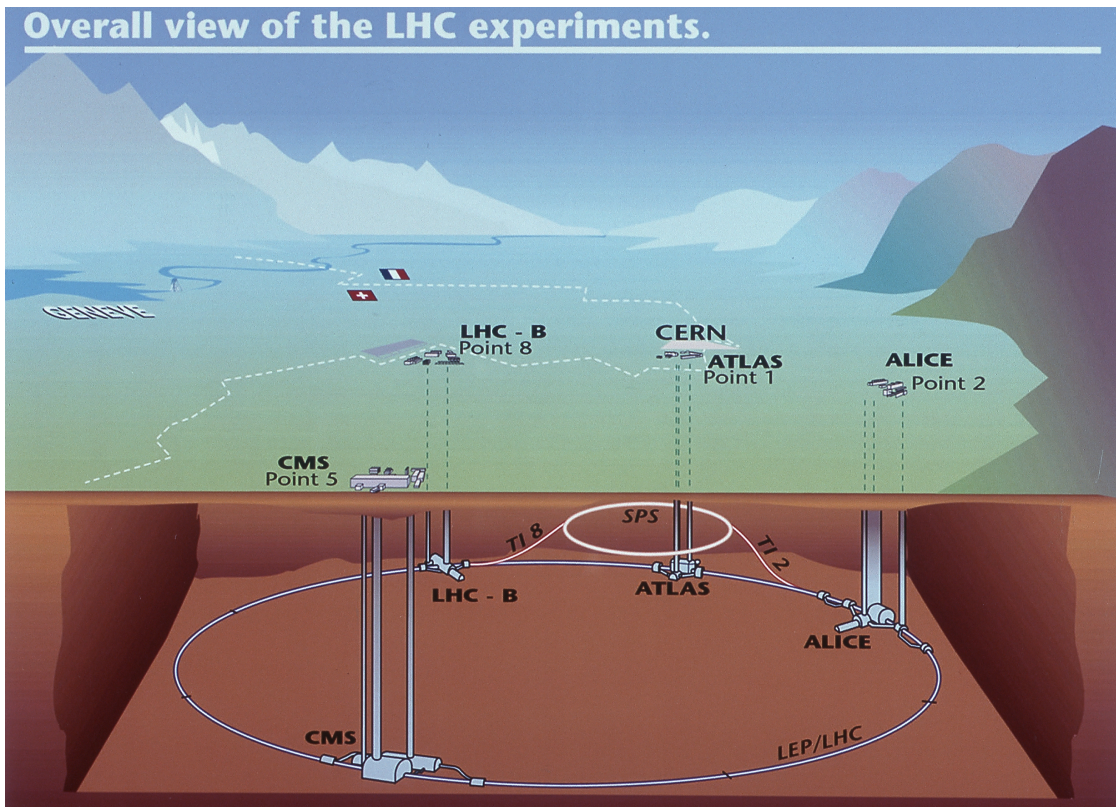
Figure 1.2: Layout of the LHC, showing locations of the experiments. ATLAS Experiment ©2012 CERN

1.3 ATLAS

The ATLAS (A Toroidal Lhc ApparatuS) experiment is one of the two general purpose detectors at the LHC, along with CMS (ALICE is primarily focused on heavy ion collisions and LHCb is focused on B physics.) It is comprised of multiple layers of detectors in concen-

tric rings surrounding the collision point. The primary subdetector systems of ATLAS are, from smallest radius to largest, the inner detector, the calorimeters, and the muon system.

The inner detector is made up of three major components: the pixel dectector, the semi-conducter tracker (SCT), and the transistion radiation tracker (TRT). The inner detector is used primarily for tracking charged particles.

The electromagnetic calorimeter measures the energy of electrons and photons, and the hadronic calorimeter measures the energy of hadrons and jets. Muons only interact minimally, so the muon detectors are at the largest radius, outside the calorimeters. Neutrinos interact only via the weak force and are detected by measuring an energy imbalance in the transverse plane which requires a symmetric design with good hermeticity.

The ATLAS collaboration includes several thousand physicists as well as engineers and other support staff. The analysis efforts of the collaboration cover a wide range of subjects from confirming and measuring various Standard Model parameters, to searching for the Higgs, to looking for evidence for a wide range of more exotic theories. The ATLAS detector will be described in more detail in Chapter 2.

Chapter 2
THE ATLAS DETECTOR

As one of the two general purpose detectors built at the LHC, ATLAS was designed to handle the extreme conditions produced when the two counter rotating beams of the LHC intersect. The LHC provides proton beams of up to 2808 bunches with 10^{11} protons per bunch that will produce 14 TeV collisions at an instantaneous luminosity of $10^{34} cm^{-2} s^{-1}$ during nominal running. The LHC also collides lead ions at up to 5.5 TeV per nucleon pair and an instantaneous luminosity of $10^{27} cm^{-2} s^{-1}$.

2.1 Definitions

A coordinate system for the ATLAS detector is defined such that the origin is at the nominal interaction point (where the two beams intersect) with the z-axis colinear with the beam and the x-y plane perpendicular to the beam. The positive x direction is towards the center of the ring and the positive y direction is up. The detector is split into two sides with Side A defined as the positive z direction and Side C as the negative z direction. The azimuthal angle, ϕ, and polar angle, θ, are defined as normal for a spherical coordinate system. However, instead of using θ, usually the polar angle is parameterized by the pseudorapidity, $\eta = -\ln\tan(\theta/2)$. Rapidity,

$$y = \frac{1}{2}\ln\frac{E + p_z c}{E - p_z c},\qquad(2.1)$$

which reduces to pseudorapidity in the limit of massless particles, is a useful variable for several reasons. Differences in rapidity between particles are invariant under Lorentz boosts along the z-axis. Also, within kinematic limits, particle production is approximately constant with respect to rapidity [31]. Transverse momentum, p_T, transverse energy, E_T, and missing transverse energy, E_T^{miss} or MET, are defined in the x-y plane. Distances are often quoted in terms of ΔR, which is defined as $\Delta R = \sqrt{\Delta\eta^2 + \Delta\phi^2}$.
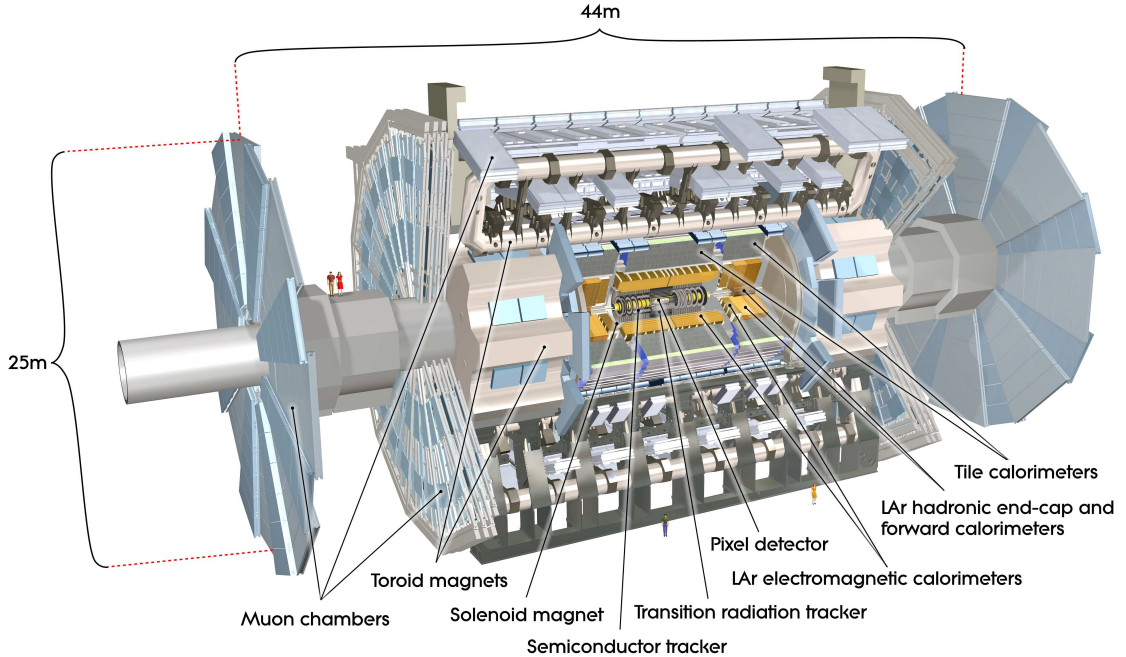
Figure 2.1: Cut-away view of the ATLAS detector. The dimensions of the detector are 25 m in height and 44 m in length. The overall weight of the detector is approximately 7000 tons. [2]

2.2 Design Requirements

The design requirements of the ATLAS detector are determined primarily by the physics goals of the project as well as the challenges provided by the extreme environment of the LHC. [2] Finding and measuring the properties of the Higgs boson is one of the most important tasks of the ATLAS experiment. If the Higgs is low mass, near the lower bound set by LEP, its decay to two photons is one of the primary discovery channels (see Figure 2.3). This requires accurate photon identification as well as precise determination of the photon energy. If the Higgs is a bit heavier then the decay to two Z bosons, where one or both are onshell is quite important. This requires good lepton identification with accurate momentum measurement and charge identification over a wide range of momenta. For a higher mass Higgs boson, the decay to WW or ZZ with final states involving jets and/or neutrinos requires good jet energy measurement as well as E_T^{miss}. While not primary discovery channels for a SM Higgs, if a Higgs-like particle is found, the $H \to \tau^+ \tau^-$ and $H \to b\bar{b}$ decays will need to be measured precisely to determine whether it conforms to SM expectations. This means that τ and b-jet indentification is important, which requires finding secondary vertices. In addition to he Higgs boson, new physics will be investigated by ATLAS. Many versions of

7

supersymmetry predict decays containing a lightest stable supersymmetric particle (LSP), this would result in large amounts of E_T^{miss} along with many leptons and jets in the final state. The cross-sections of all the new physics processes are quite small, which is why the luminosity of the LHC must be so large. However, this comes with a price. The inelastic cross-section is much higher ($\sim$100 mb), and the majority of LHC collisions produce events that involve no new physics (see Figure 2.2). Even when a bunch crossing does produce an interesting candidate event, it has to be disentangled from the inelastic collisions produced in the same bunch crossing ($\sim$ 23/bunch crossing at nominal conditions).

For the ATLAS detector to be successful it has to have fast, radiation hard electronics and sensors with high granularity, especially near the interaction point. The η and ϕ acceptance needs to be as large and symmetric as possible. The tracking detectors need to have good momentum resolution, charge determination, high efficiency and allow for vertex finding down to a very small radius. Calorimeters, both electromagnetic, for electron/photon measurements, and hadronic, for hadrons and jets and E_T^{miss} for neutrinos are needed. Good μ identification and resolution are important over a wide p_T range with no charge ambiquity. A robust trigger system is needed that can deal with the very high rates of the LHC and maintain a high efficiency for events with possible new physics. An additional complication is the need for high magnetic fields for momentum and charge measurements in both the tracking detectors and the muon spectrometer.

2.3   The Inner Detector

The inner detector of ATLAS is comprised of three subsystems: the pixel detector, the semiconductor tracker (SCT) and the transition radiation tracker (TRT), in order of increasing radius. These three subdetectors are immersed in a 2 T field produced by a solenoid magnet. Each of the three subdetectors has a central barrel region made of concentric cylinders around the beam axis as well as endcaps made of disks perpendicular to the beam. Precision tracking is provided by the pixel detector and SCT. They cover a pseudorapidity region of $|\eta| < 2.5$. Figure 2.4 shows the layout of the inner detector.

2.3.1   The Pixel Detector

The pixel detector is made up of 80.4 million silicon pixels in three layers (both barrel and endcaps). The innermost layer of the pixel detector is only 45 mm away from the beam. About 90% of the pixel sensors have a nominal pitch of 50 x 400 μm with the remaining pixels at 50 x 600 μm. The pixel detector has full coverage in ϕ and extends to $|\eta| < 2.5$ in pseudorapidity. A cut-away view of the pixel detector is shown in Figure 2.6.

The high resolution and close proximity to the interaction point is necessary for accurate vertexing. However, since it is the part of the detector closest to the collisions it is also
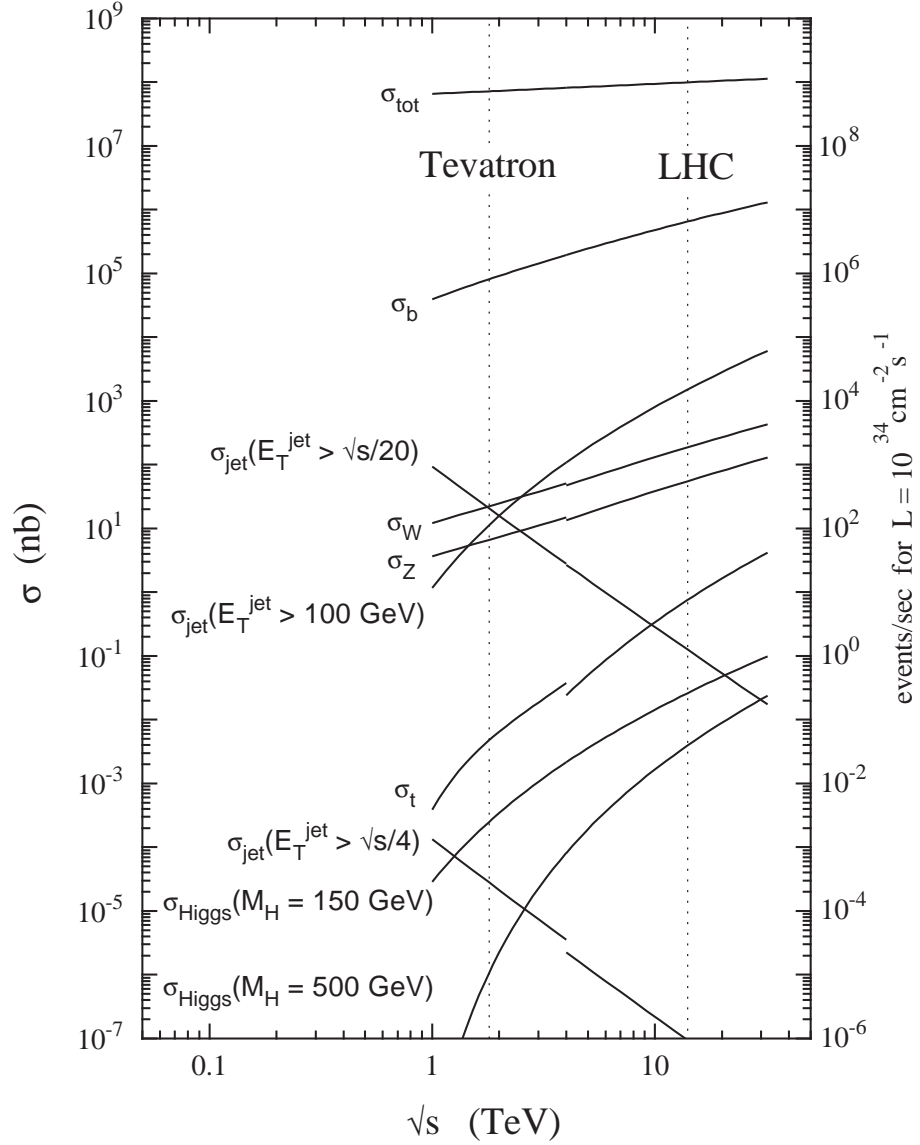
Figure 2.2: Cross-sections of various processes at proton-proton and proton-antiproton colliders as a function of center of mass energy [3].
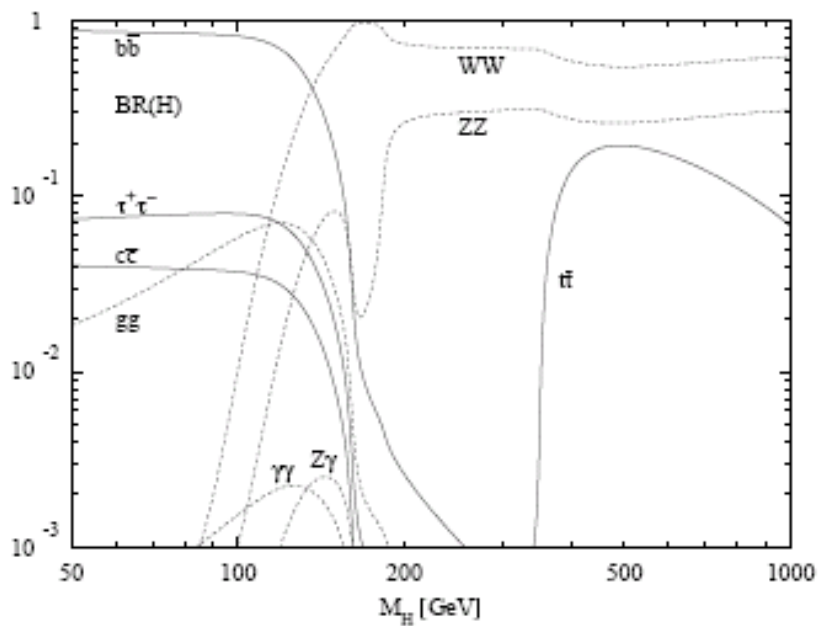
Figure 2.3: Branching ratios for the Higgs as a function of mass [4].
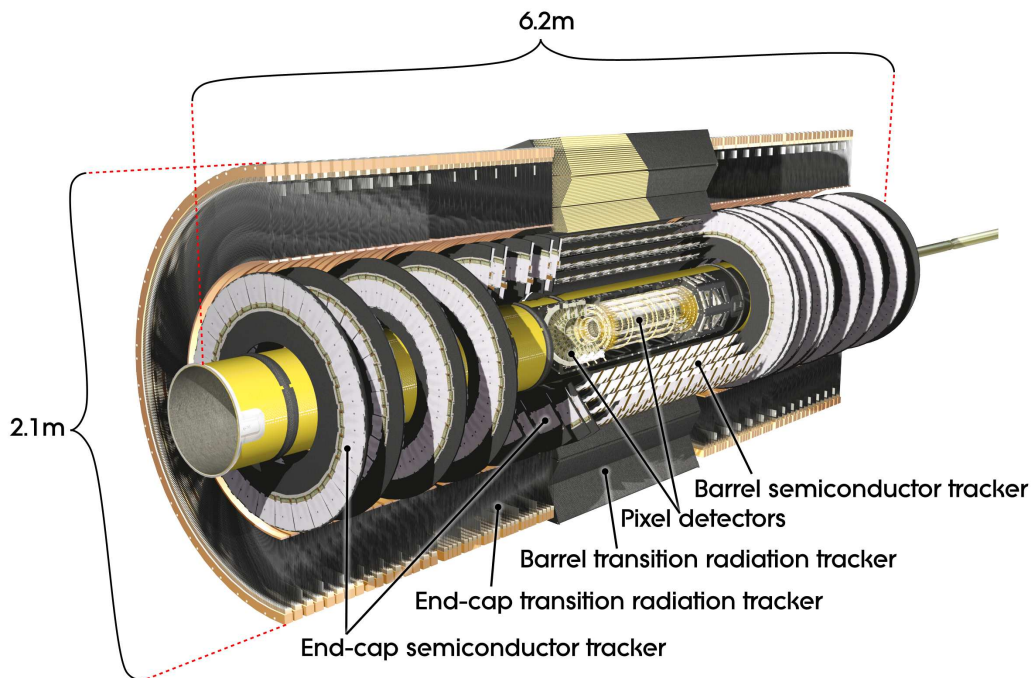
Figure 2.4: Cut-away view of the ATLAS Inner Detector. [2]
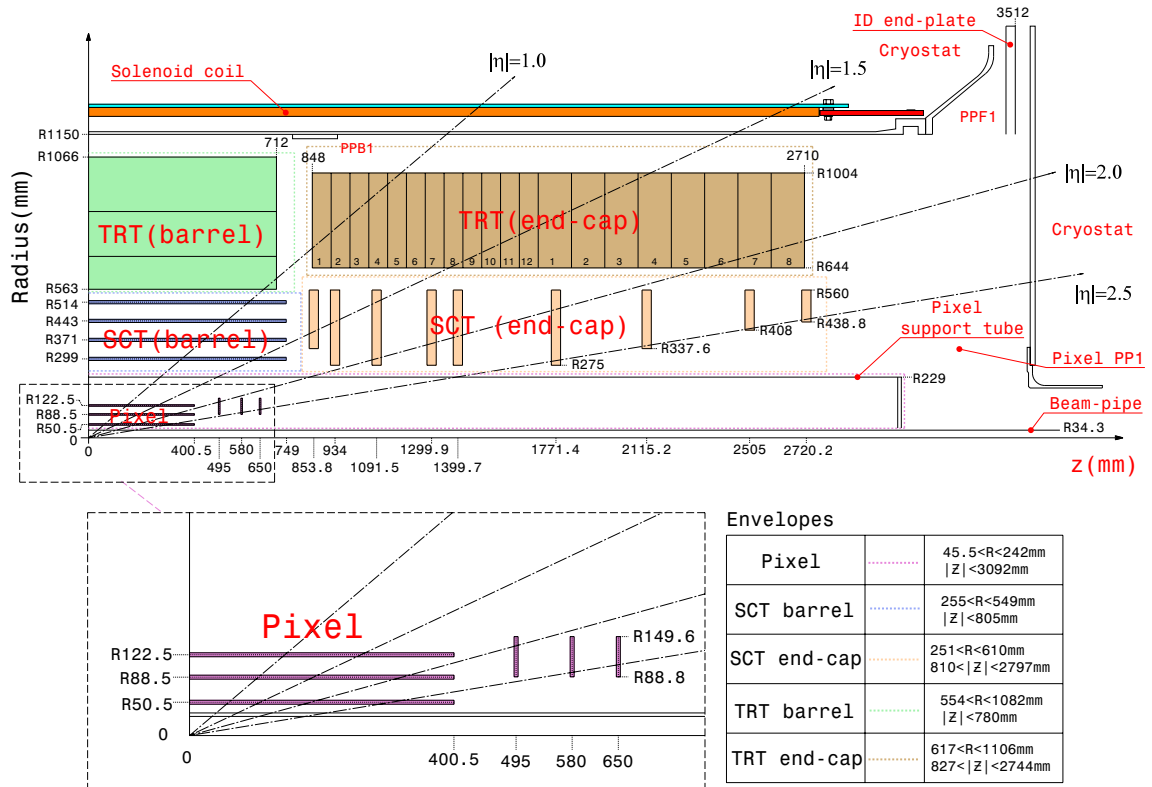
Figure 2.5: Plan view of a quarter-section of the ATLAS inner detector showing each of the major detector elements with its active dimensions and envelopes. The labels PP1, PPB1 and PPF1 indicate the patch-panels for the ID services. [2]

1442mm

430mm

Barrel Layer 2

Barrel Layer 1

Barrel Layer 0 (b-layer)

End-cap disk layers
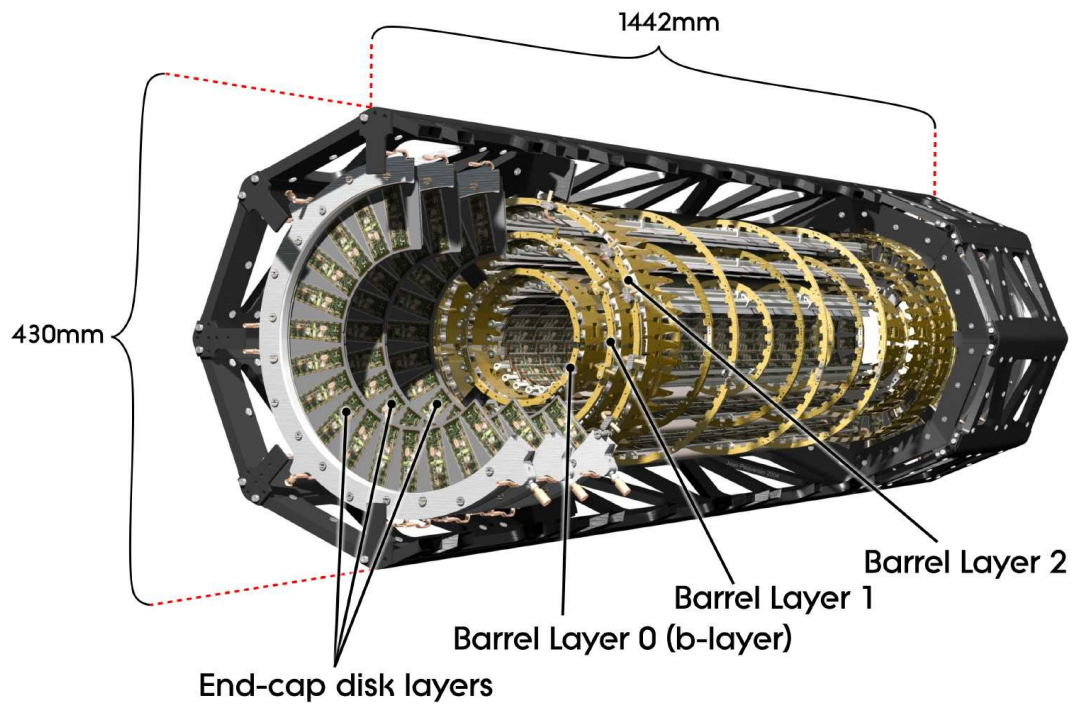
Figure 2.6: A perspective cut-away view of the pixel detector. The view shows individual barrel and end-cap modules, supported with their associated services on staves and disks within an octagonal support frame. [5]

exposed to very high levels of radiation. The pixel sensors and front end electronics were specifically designed to be as resistant as possible to damage from this radiation. The sensor is made with an n-type bulk with n^+-type implants on the readout side and p^+-type implants on the back side. Initially, the depletion region grows from the back side. Radiation damage will cause a gradual decrease in doping concentration in the bulk; this leads eventually to type inversion after which the depletion region grows from the read out side, and the doping concentration start increasing again. Leakage current also increases with radiation damage. The radiation damage effects are minimized by running the pixel detector in an operating range of $-5°C$ to $-10°C$. Despite the efforts to minimize the effect of radiation damage, it is expected that the innermost layer of the pixel detector will need to be replaced after running for three years at design luminosity.

(a) before type inversion   (b) after type inversion
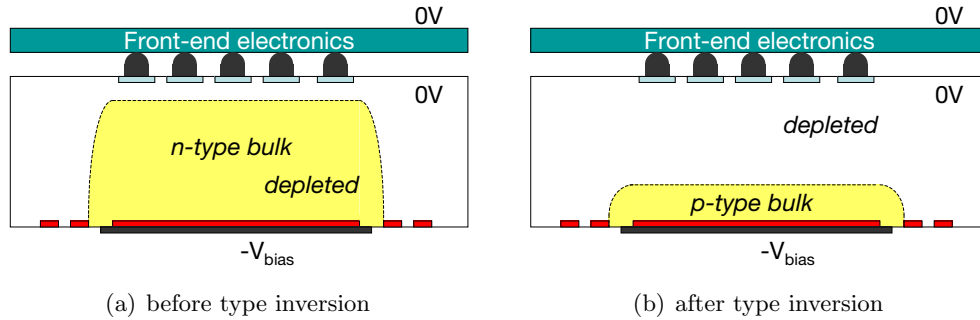
Figure 2.7: Comparison of depletion zones in n^+-in-n pixel sensors before (a) and after (b) type inversion. Before type inversion the electrical field grows from the backside and reaches the pixel implants (full depletion). After type inversion the depletion zone grows from the pixel side and allows operation even if the bulk is not fully depleted. [5]

Figures 2.8 and 2.9 show the distributions of residuals, defined as the distance from the hit to the fitted track, in the local x and y directions of the pixel module for the hit positions with respect to the fitted tracks in both Monte Carlo simulations and data. The estimated gaussian width of the distributions, FWHM/2.35, is a measure of the hit position resolution with the difference between MC and data coming primarily from misalignment [6]. The local x coordinate corresponds to the $r\phi$ direction, with widths of FWHM/2.35 = 9 μm and 15 μm respectively for the barrel and endcap. The local y is along the beam for the barrel modules and radial for the endcap modules with widths of FWHM/2.35 = 84 μm and 140 μm respectively. Hit and cluster positions for the entire inner detector were reconstructed from the raw data and used to find and fit tracks.
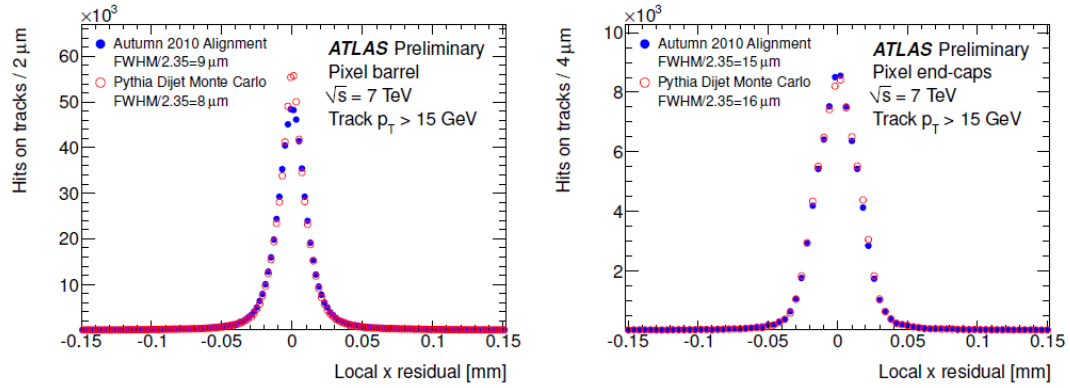
Figure 2.8: Plots showing hit-on-track residual distributions for the barrel (left) and endcaps (right) in the local x direction. The gaussian width of the distributions are estimated by FWHM/2.35 = 9 μm and 15 μm respectively [6].
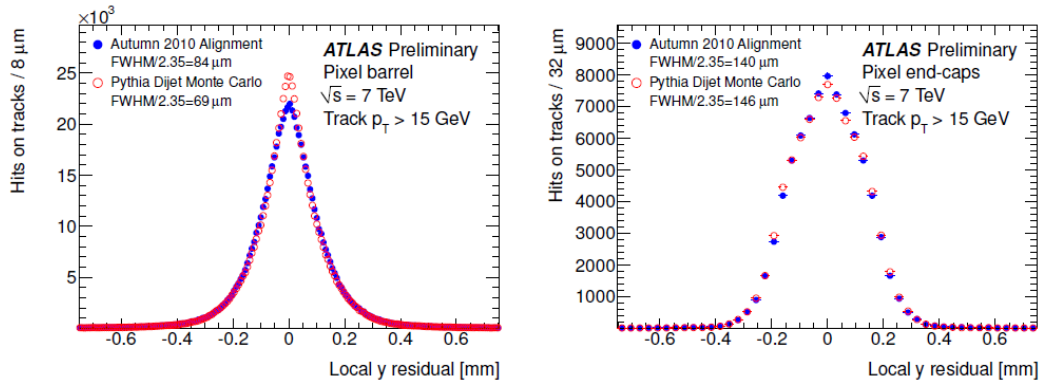
Figure 2.9: Plots showing hit-on-track residual distributions for the pixel barrel (left) and endcaps (right) in the local y direction. The gaussian width of the distributions are estimated by FWHM/2.35 = 84 μm and 140 μm respectively [6].
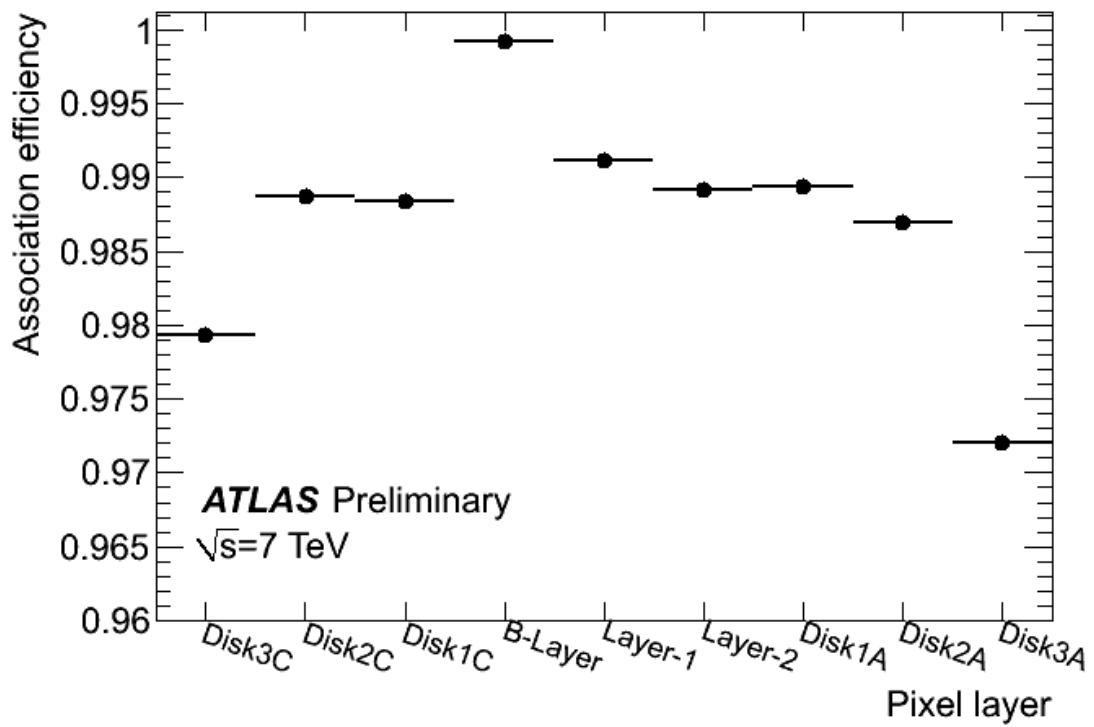
Figure 2.10: Efficiency for a track to have an hit associated when crossing a pixel detector layer. The average efficiency for all layers is 98.8% [7].

Figure 2.10 shows the association efficiency for the different layers of the pixel detector. The association efficiency is a measure of how likely a track crossing a pixel layer will have an associated hit in that layer. Dead modules are excluded from the calculation. The full efficiency in the B layer is due to the requirement of a B layer hit in the track selection. The average efficiency in all layers is 98.8%. As of June 11, 2012, 4.2% of pixel modules were disabled [32].

The communications system for both detector control and data acquisition uses optical links [33], also known as optoboards, designed and built at the Ohio State University. The optoboards receive optical control signals and convert them to electronic form before sending them to the detector modules. Electronic signals from the modules are converted to optical signals and relayed back to central ATLAS control. As part of my work for the ATLAS collaboration I worked on the testing and installation of the optoboards at CERN in 2006 and 2007.

2.3.2 Semiconductor Tracker

The SCT is made up of silicon strips that provide 6.3 million channels in 8 layers in the barrel region and 9 layers of discs in each endcap. The eight barrel layers are actually 4 double sided layers. The strips on each side of a layer are rotated with respect to each other by 40 μrad. This allows for precision measurements of tracks even in the direction along the strip length by combining the hit information from the two sides of each layer. Each strip is 12 cm long, and the strip pitch in the barrel is 80 μm and the mean pitch of the radial strips in the endcap is also $\sim$ 80 μm. The SCT operates at the same temperature as the pixel detector and has the same η and ϕ coverage, despite being at a larger radius. Details of the Inner Detector geometry can be found in Figure 2.5.

Figure 2.11 shows the distributions of residuals in the local x direction of the SCT module similarly to the pixel plots in the previous section. The local x coordinate corresponds to the $r\phi$ direction and is oriented across the strips. The widths are FWHM/2.35 = 25 μm and 30 μm respectively for the barrel and endcap.

Figure 2.12 shows the hit efficiency for the SCT for two different types of tracks, inner detector combined and SCT standalone. SCT standalone tracks seven SCT hits are required, not including the layer in question, while for ID combined tracks, only 6 SCT hits are required. Dead modules and chips are accounted for in the calculation. As of the summer of 2012 0.97% of SCT elements were disabled [32].

2.3.3 Transistion Radiation Tracker

The TRT is a straw tube detector that provides many hits per track ($\sim$ 36), but only provides $R - \phi$ information [34]. There are 351,000 readout channels. In the barrel region
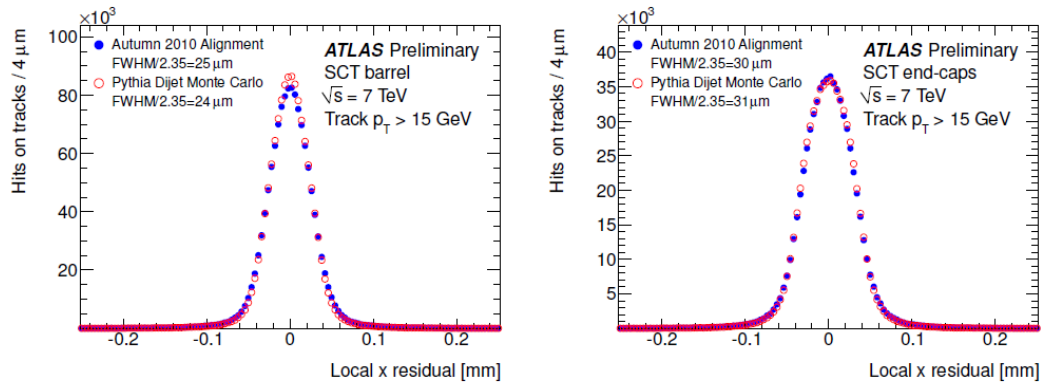
Figure 2.11: Plots showing hit-on-track residual distributions for the SCT barrel (left) and endcaps (right) in the local x direction. The gaussian width of the distributions are estimated by FWHM/2.35 = 25 μm and 30 μm respectively [6].

(a) (Barrel)
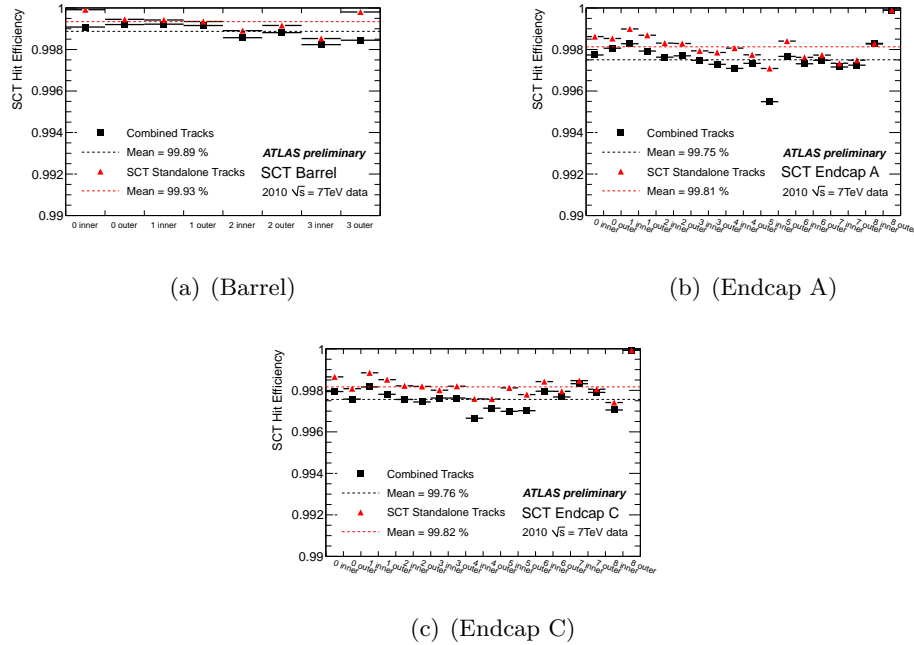
(b) (Endcap A)

(c) (Endcap C)

Figure 2.12: The intrinsic module efficiency is shown for the (a)barrel, (b)endcap A, and (c)endcap C regions. The average efficiencies for standalone tracks are 99.93%, 99.81%, and 99.82% respectively, and 99.89%, 99.75%, and 99.76% for combined tracks [8].

17

($|\eta| < 1$), the straws are aligned in the z direction and are interleaved with radiator fibers, while in the forward regions (out to $|\eta| < 2$) the straws are aligned radially and layers of straws are interleaved with radiator foils. The straws are 4 mm in diameter and made up of two multilayer films bonded back to back. The film is 25 μm of polyimide covered on one side by 0.2 μm of Al and 5 μm of graphite-polyimide, while the back side is coated with a 5 μm layer of polyurethane to heat seal the two films together. The straws were cut to length after fabrication to 37 cm for the endcap and 144 cm for the barrel. The wall of the straw serves as the cathode and has a resistance of < 300 Ω/m. The anode for each straw is a 31 μm diameter tungsten wire plated with a 0.5 to 0.7 μm gold layer. The anode resistance is about 60 Ω/m. The nominal gas mixture in the TRT is 70% Xe, 27% CO_2 and 3% O_2. Transition radiation photons are emitted by electrons when they hit the polypropylene fibers in the barrel region and the foils in the endcap region. The signals from this transition radiation have a much higher amplitude than the tracking signals from minimum ionizing charged particles moving through the straws. Separate high and low thresholds can be applied to distinguish these signals and help to identify electrons.
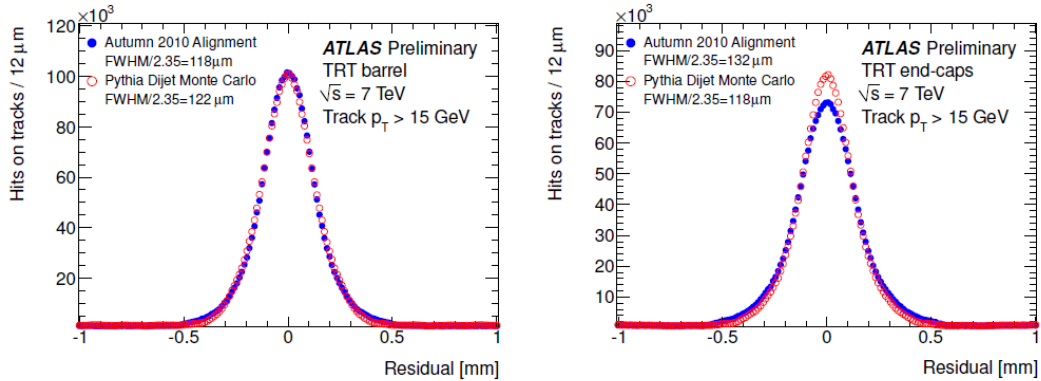
Figure 2.13: Plots showing hit-on-track residual distributions for the TRT barrel (left) and endcaps (right) in the local x direction. The gaussian width of the distributions are estimated by FWHM/2.35 = 118 μm and 132 μm respectively [6].

Figure 2.13 shows residual plots for the TRT analogous to the SCT and pixel plots in the previous sections. The local x coordinate corresponds to the $r\phi$ direction and is oriented across the straws. The widths are FWHM/2.35 = 118 μm and 132 μm respectively for the barrel and endcap.

The hit reconstruction efficiency in Figure 2.14 is defined as the number of straws with

(a) (Barrel) (b) (Endcap)
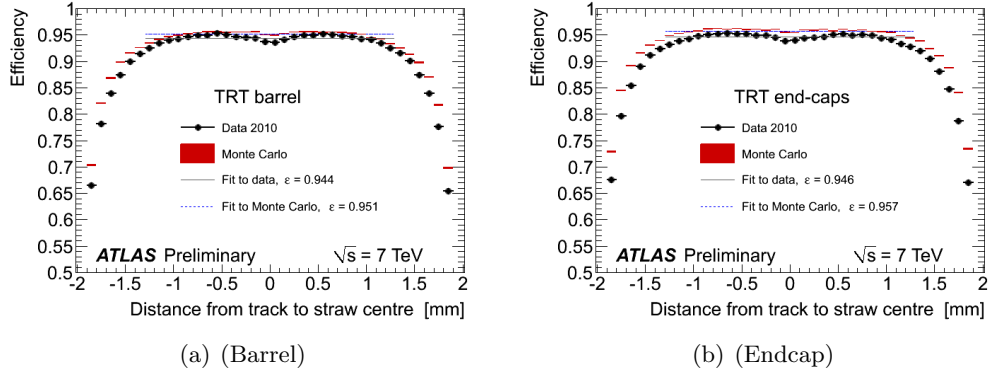
Figure 2.14: The plots above show the TRT hit reconstruction efficiency as a function of distance of closest approach of the track to the straw center. A linear fit to the central region in the data obtains an average efficiency of 0.944 in the barrel and 0.946 in the endcap [9].

a hit on track divided by the number of straws crossed by the track. Only straws between the first and the last straws with a reconstructed hit on the track are considered in the efficiency calculation (the first and last straws are excluded). Straws that were known to be non-functioning were excluded. A linear fit was performed on the data in the central part of the straw and obtained an average efficiency of 0.944 in the barrel and 0.946 in the endcap. As of the summer of 2012 2.4% of TRT channels were dead [35].

2.4 Calorimetry

Like the Inner Detector, the electromagnetic (EM) and hadronic calorimeters in ATLAS have both barrel and endcap components in addition to a forward calorimeter at high pseudorapidity. In contrast to the Inner Detector, the calorimeters need to absorb as much energy from incoming particles as possible. Ideally, all photons and electrons are stopped within the EM calorimeter and all hadrons and jets are stopped within the hadronic calorimeter. The EM calorimeter is more finely segmented in order to use details of the shower shapes to distinguish between photons, electrons and jets. Since essentially all electrons and photons are stopped before the end of the EM calorimeter, the hadronic calorimeter, at higher radius, does not need to be as finely segmented. Almost all hadronic jets are completely absorbed before they reach the edge of the hadronic calorimeter.

2.4.1 Liquid Argon Electromagnetic Calorimeter

The EM calorimeter uses a lead-liquid argon (LAr) detector technology. Energy deposited in the LAr cells ionizes the argon atoms, and the charge collected is proportional to the energy

Tile barrel   Tile extended barrel

LAr hadronic
end-cap (HEC)

LAr electromagnetic
end-cap (EMEC)

LAr electromagnetic
barrel

LAr forward (FCal)
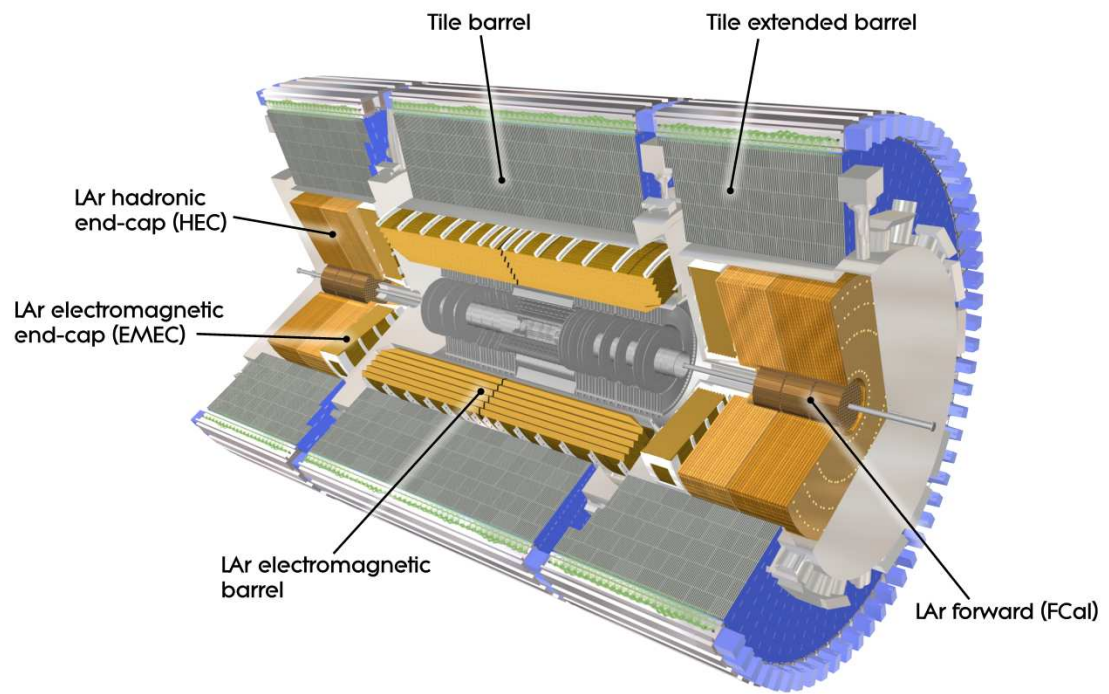
Figure 2.15: Cut-away view of the ATLAS calorimeter system. [2]
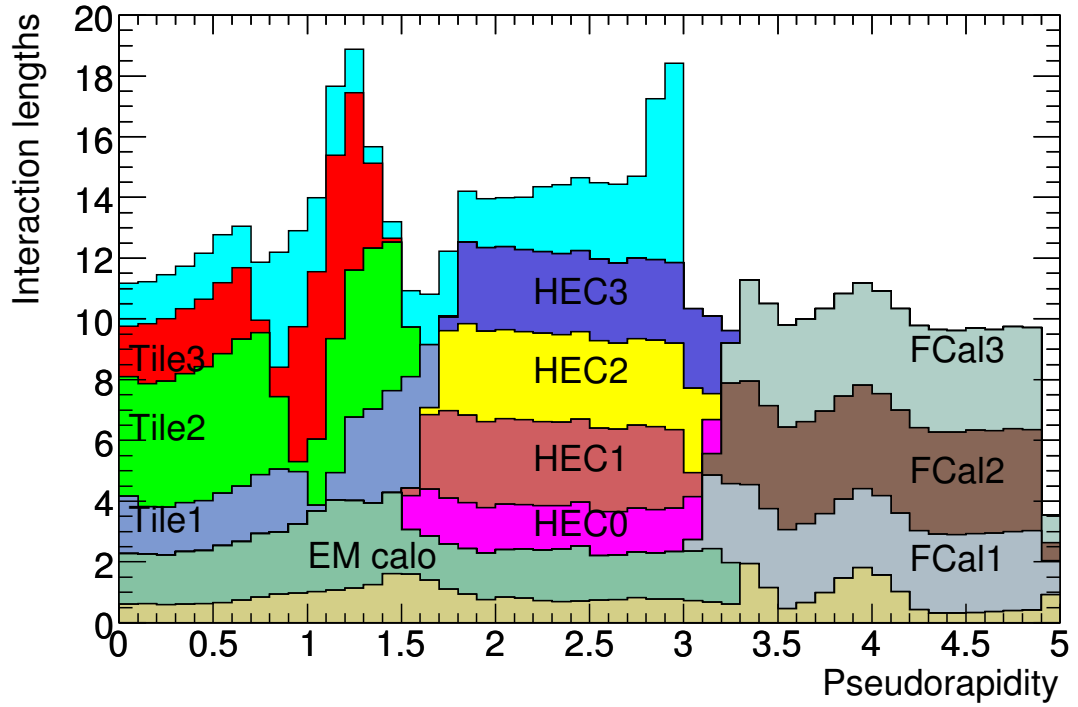
Figure 2.16: Cumulative amount of material, in units of interaction length, as a function of $|\eta|$, in front of the electromagnetic calorimeters, in the electromagnetic calorimeters themselves, in each hadronic compartment, and the total amount at the end of the active calorimetry. Also shown for completeness is the total amount of material in front of the first active layer of the muon spectrometer (up to $|\eta| < 3.0$). [2]

deposited. Lead is used as an absorber to help slow down the high energy electromagnetic particles. The area of the EM calorimeter matching the inner detector acceptance of $|\eta| < 2.5$ has three layers and high granularity for precision physics, at higher pseudorapidity there are only two layers and coarser granularity. The EM calorimeter uses an accordion geometry as shown in Figure 2.17. This geometry natually allows for full ϕ coverage without any cracks. In order to keep the liquid argon gap constant, the bending angles of the accordion have to change with radius.

The lead absorbers range in thickness from 1.13 mm to 2.2 mm depending on η. For mechanical stability they are glued to sheets of stainless steel 0.2 mm thick. The electrodes are located in the gap between absorbers and are made up of three copper sheets separated by insulating polyimide. The two outer copper layers are kept at high voltage and the signal is read out by the inner layer via capacitive coupling.

Of the three layers of the EM calorimeter, the first is the most finely segmented and the third has the coarsest segmentation, as it collects only the tail of the electromagnetic shower. There is a liquid argon presampler, 11 mm thick (5 mm in the endcap), in front of the first layer of the EM calorimeter. In the barrel this presampler layer is made of 64 identical sectors in ϕ. In the endcap there are 32 azimuthal sectors. The presampler detector is used to correct for the energy lost by electrons and photons upstream of the calorimeter.

Figure 2.18 shows the relative energy resolution for electron test beam data. The data are fit with a function of the form $\sigma_E/E = a/\sqrt{E} \oplus b$ where the $\oplus$ indicates a sum in quadrature. Values of $a = (10.1 \pm 0.1)\% \cdot \sqrt{\text{GeV}}$ and $b = (0.17 \pm 0.04)\%$ are obtained from the fit.

2.4.2   Hadronic Calorimeters

The hadronic calorimeters use multiple detector technologies. The barrel and extended barrel sections extend out to $|\eta| < 1.7$ and use scintillating tiles with steel as an absorber. The endcap uses copper-LAr and extends to $|\eta| < 3.2$. The forward calorimeter also uses LAr, but with both copper and tungsten absorbers and extends to $|\eta| < 4.9$.

The barrel regions use an optical readout system in which optical fibers run from each scintillator to photomultiplier tubes located at the outer edge of the hadronic calorimeter.

The hadronic endcap calorimeter (HEC) is made up of two wheels on either side of the interaction point. The inner wheels are made of 24 copper plates, each 25 mm thick, plus a 12.5 mm thick front plate. The outer wheels have a coarser sampling fraction with modules made of 16 copper plates, each 50 mm thick, plus a 25 mm thick front plate. The gaps between all plates are 8.5 mm.

Figure 2.20 shows the relative energy resolution measured during pion test beams. The data are fit by a function of the same form as the liquid argon electron test beam data

Cells in Layer 3
$\Delta\varphi \times \Delta\eta = 0.0245 \times 0.05$

Trigger Tower
$\Delta\eta = 0.1$

$2X_0$

$\eta = 0$

470 mm

$16X_0$

Trigger
Tower
$\Delta\varphi = 0.0982$

$4.3X_0$

1500 mm

$1.7X_0$
$\Delta\varphi = 0.0245 \times 4$
36.8mm×4
=147.3mm

Square cells in
Layer 2

$\Delta\varphi = 0.0245$

φ

$37.5mm/8 = 4.69$ mm
$\Delta\eta = 0.0031$

$\Delta\eta = 0.025$

Strip cells in Layer 1

η
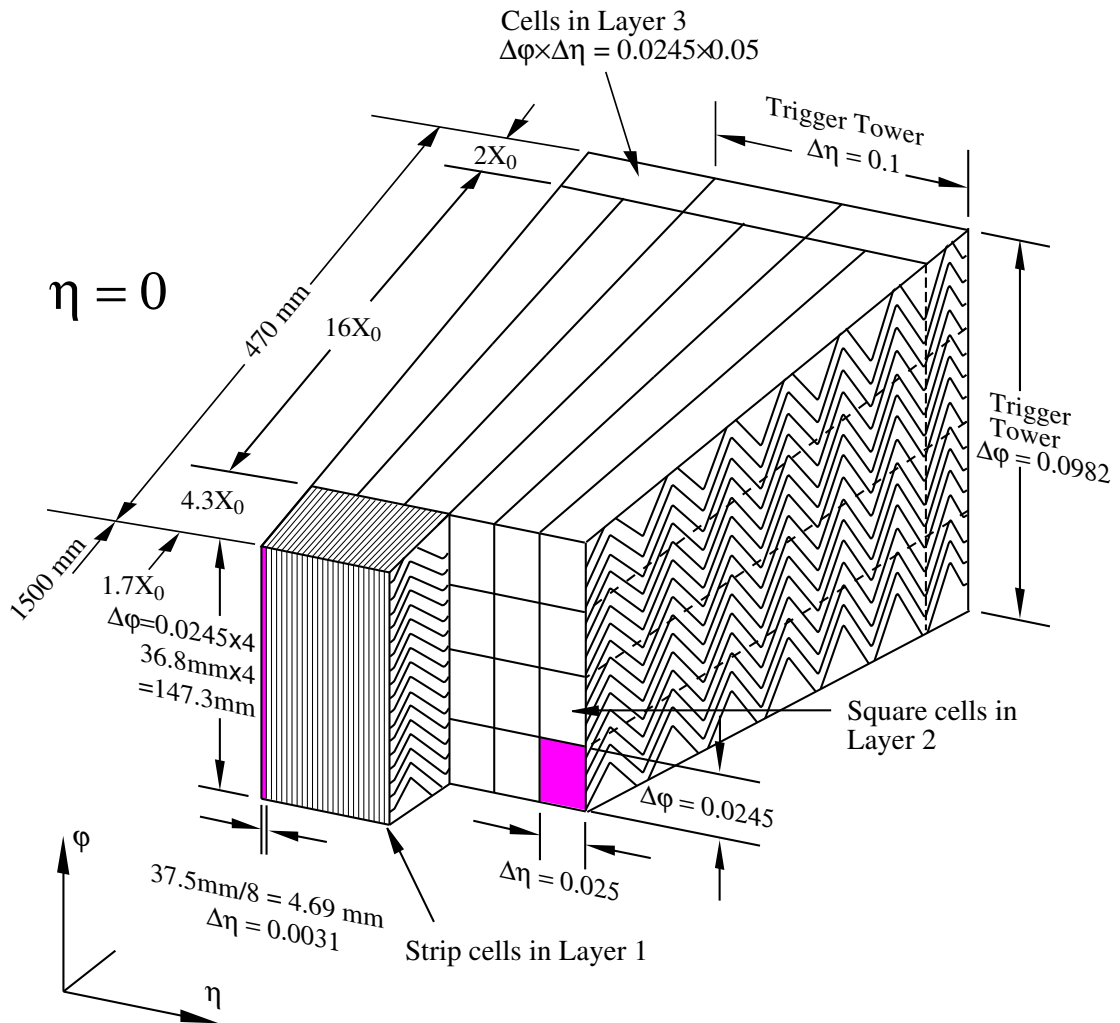
Figure 2.17: Sketch of a barrel module showing the granularity in eta and phi of the cells of each of the three layers and of the trigger towers. [2]
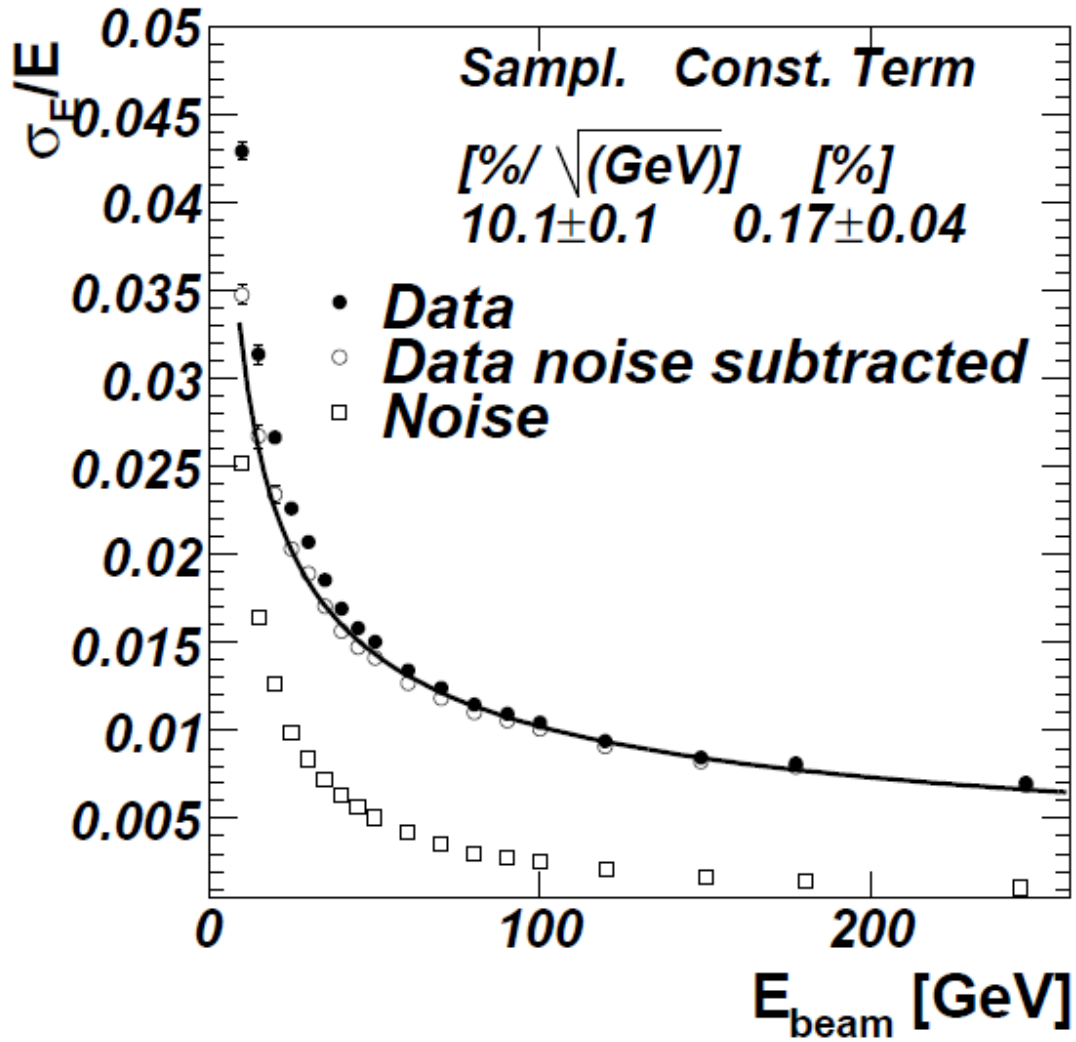
Figure 2.18: Relative energy resolution in the liquid argon calorimeter from electron test beam data. The data are fit with the function described in the text and values of $a = (10.1 \pm 0.1)\% \cdot \sqrt{\text{GeV}}$ and $b = (0.17 \pm 0.04)\%$ are obtained [10].
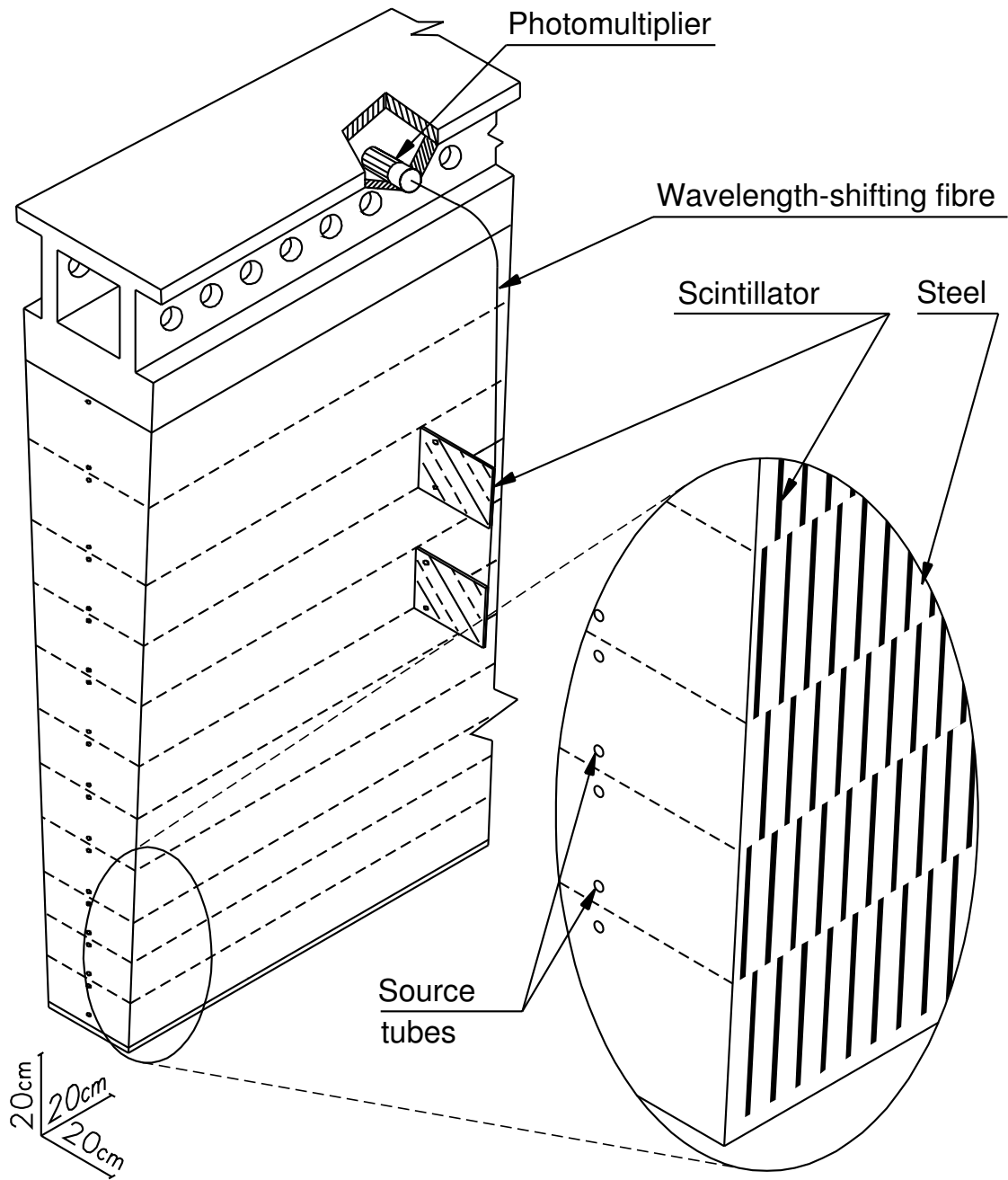
Figure 2.19: Schematic showing how the mechanical assembly and the optical readout of the tile calorimeter are integrated together. The various components of the optical readout, namely the tiles, the fibres and the photomultipliers, are shown. [2]
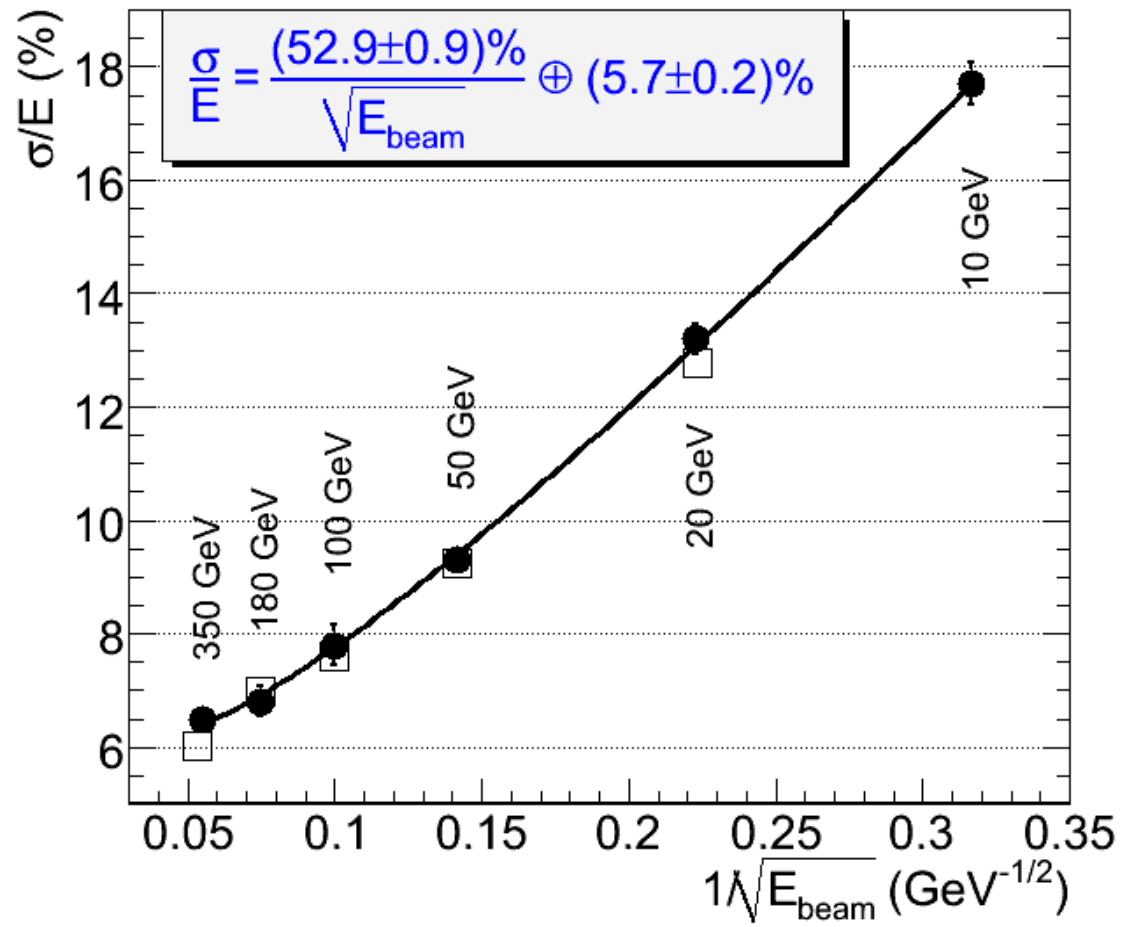
Figure 2.20: Energy resolution from pion test beams with parameters $a = (52.9 \pm 0.9)\% \cdot \sqrt{\text{GeV}}$ and $b = (5.7 \pm 0.2)\%$ [11].

yielding values of $a = (52.9 \pm 0.9)\% \cdot \sqrt{\text{GeV}}$ and $b = (5.7 \pm 0.2)\%$.

The forward calorimeter (FCal) is made up of 3 modules on each side. The innermost module is primarily an electromagnetic calorimeter while the two outer modules are hadronic.
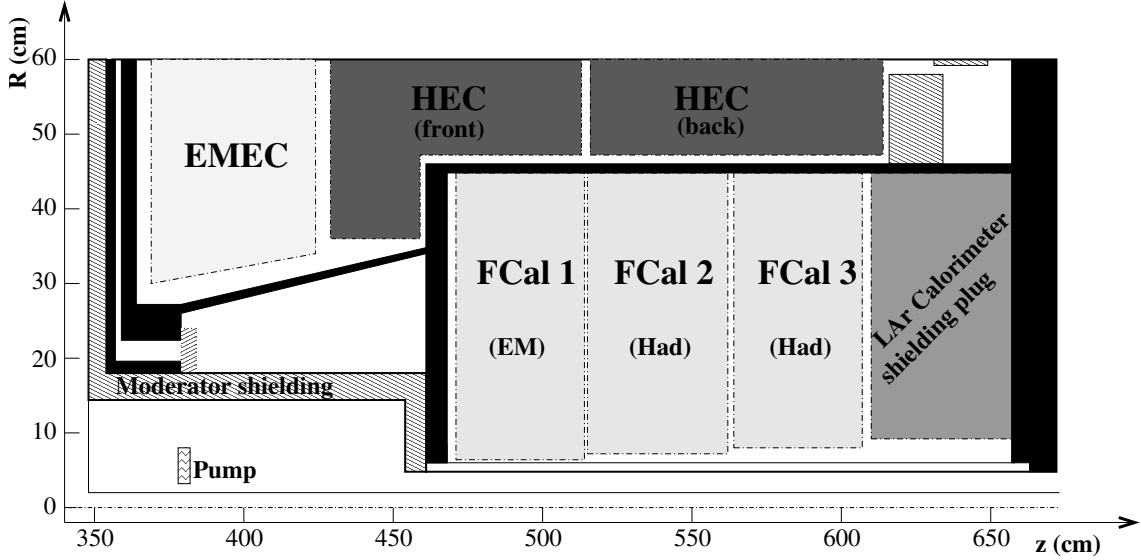
Figure 2.21: Schematic diagram showing the three FCal modules located in the end-cap cryostat. The material in front of the FCal and the shielding plug behind it are also shown. The black regions are structural parts of the cryostat. The diagram has a larger vertical scale for clarity. [2]

2.5 Muon System

The muon spectrometer is located outside the calorimeters in a toroidal magnetic field separated into barrel and endcap regions. For $|\eta| < 1.4$, the barrel toroid provides bending power and for $1.6 < |\eta| < 2.7$ tracks are bent by the endcap toroid. The transition region, $1.4 < |\eta| < 1.6$, is covered by a combination of the two. Several different detector types are used in the muon system.

Precision tracking is provided by monitored drift tubes (MDTs) in the central region and cathode strip chambers (CSCs) at higher pseudorapidities. The muon spectrometer delivers a transverse momentum resolution of approximately 10% for 1 TeV tracks and can supply reasonable measurements of momenta in a range from 3 GeV to 3 TeV.

The MDTs use a similar detection technology to the TRT, with the tube (diameter

29.970 mm) acting as a cathode and a wire running through the center of the tube as the anode. The MDTs use a gas mixture of 93% Ar and 3% CO_2. In the barrel region the MDT chambers are arranged in three layers of octants with each octant containing a large and a small chamber that overlap, giving continuous coverage in ϕ. While in the endcaps there are trapezoidal chambers arranged in large wheels.

At high pseudorapidity and nearer to the beamline, the particle flux becomes too high for the MDTs and CSCs must be used for precision tracking. The safe threshold for MDTs is 150 Hz/cm^2, while the CSCs can operate safely up to 1000 Hz/cm^2. The CSCs are multiwire proportional chambers with the central wire in each chamber pointing in the radial direction and the other wires in the chamber parallel to that. On each side there are eight chambers in each of two discs, with large chambers in one disc and small in the other. Each chamber is divided into four CSC planes, providing four measurements of η and ϕ for each track. The wires serve as anodes while cathodes are segemented into strips, with the strips perpendicular to the wires on one surface and and parallel to the wires on the other. The precision coordinate in a CSC is obtained by the relative measurement of charges induced on adjacent strips (the anode wires are not read out).

In addition to tracking detectors, the muon system has separate detectors for triggering. Resistive plate chambers (RPCs) and thin gap chambers (TGCs) are used in the barrel and endcap regions, respectively. The challenges for triggering detectors are different than for precision detectors. The granularity can be much coarser, but the response must be faster and robust against neutron and photon hits from background in the experimental hall.

The RPCs use parallel plates as electrodes, separated by a 2 mm gap filled with a gas mixture of $C_2H_2F_4$/Isobutane/SF_6 (94.7/5/0.3). High voltage is applied and avalanches form along ionizing tracks toward the anode. Each RPC module is made up of two units, and each unit has two parallel gas volumes. Most RPCs are attached to MDTs with equal dimensions, but since RPCs have a smaller volume than MDTs it is possible to put some RPCs in locations where MDTs will not fit (e.g. the feet region and the magnet ribs).

Like the CSCs the TGCs are multiwire proportional chambers. In addition to providing muon trigger capabilities they also complement the radial measurement of the MDTs with an azimuthal measurement.

Figure 2.23 shows the spatial resolution of the MDT chambers in the barrel region on side A. The resolution ranges from ~ 250 μm near the wire where it is dominated by the fluctuations in size and position of the primary ionization clusters to ~ 60 μm further from the wire where diffusion is more important [36].
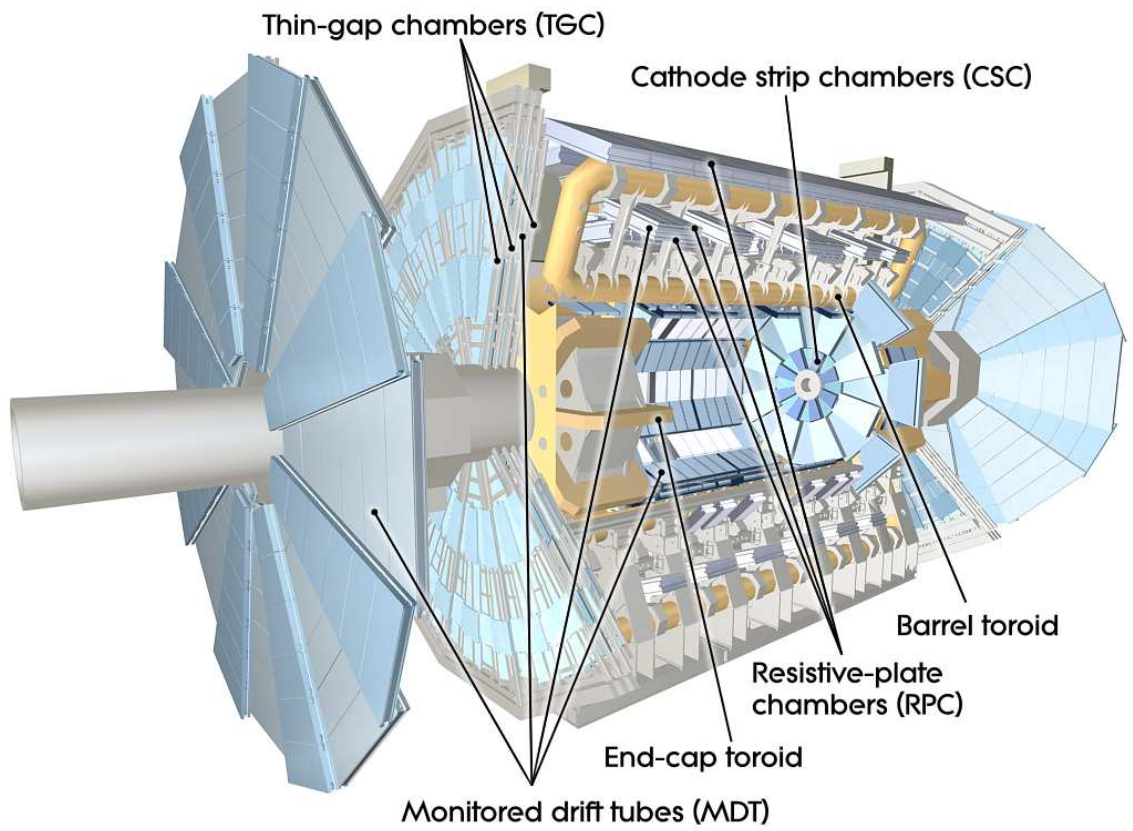
Figure 2.22: Cut-away view of the ATLAS muon system. [2]
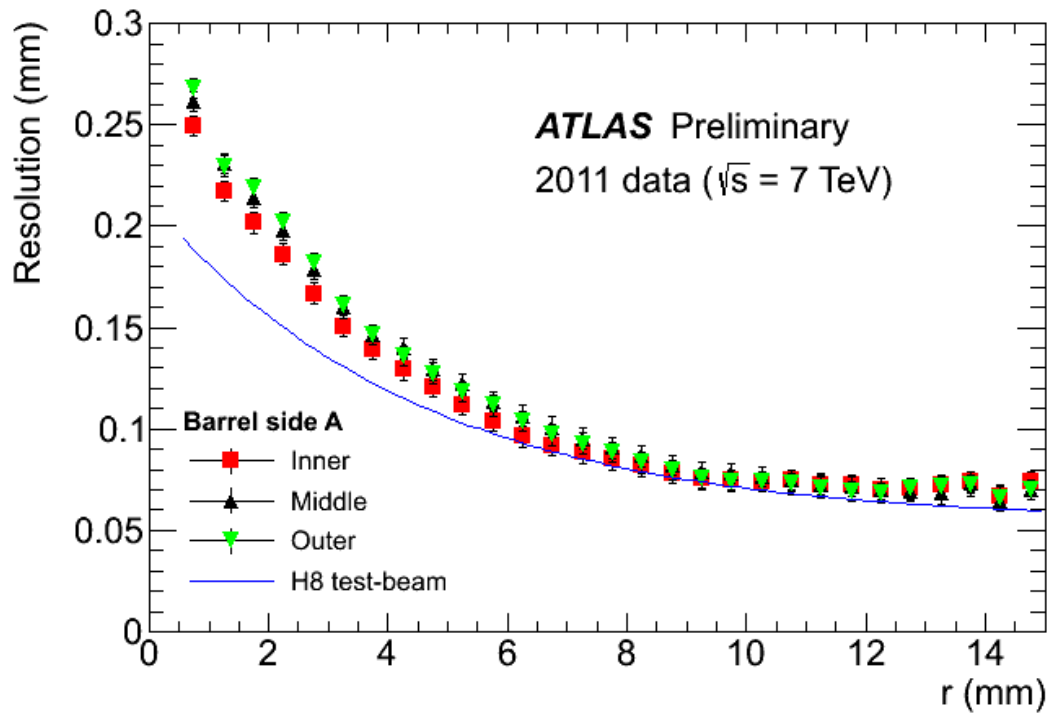
Figure 2.23: Spatial resolution of the MDT as a function of distance of the muon track from the wire for inner (red squares), middle (black triangles), and outer (green triangles) chambers of the muon spectrometer barrel side A.[12]

2.6 Trigger System

The trigger system in ATLAS is necessary to deal with the very high collision rate of approximately 40 MHz. There are three levels: L1, L2, and the event filter. L2 and the event filter are sometimes referred to as the high level trigger (HLT). Each level successive level takes input from the previous level and can apply additional selection criteria.

The L1 trigger needs to make a decision on whether to keep or throw away an event in less than 2.5 μs, so it uses a subset of detectors to search for high p_T leptons, photons and jets as well as large E_T^{miss} and total E_T. For a given set of running conditions (collision energy, luminosity, etc.) there can be a large number of different thresholds on different quantities applied as part of a trigger menu. Since L1 is limited to a maximum output of 75 kHz, some of the individual triggers on the trigger menu need to be prescaled. For example, a prescale of 0.1 would mean that only 1 out of 10 events that passed the trigger threshold would be sent to the next level. The L1 trigger also defines Regions-of-Interest (RoIs) in each event. These RoIs describe the geographical areas of the detector where interesting features were seen.

The L2 trigger takes each event sent on by the L1 trigger along with the RoI data and uses a more complete subset of the detector information to make a decision. This takes about 40 ms per event and reduces the rate to about 3.5 kHz.

The event filter is the final stage, with an average event processing time of four seconds and reduces the rate to 200 Hz. The raw event data is written to disk and processed to create the event summary data (ESD), analysis object data (AOD), and derived physics data (DPD) files in order of decreasing size.

2.7 Luminosity and Detector Protection

Luminosity is a measure of the number of collision events seen by the detector. It is expressed in units of inverse cross section. In order to measure the cross section for a particular process it is necessary to know the luminosity of the dataset in addition to the number of observed events. The accuracy and precision of the luminosity determination affects all physics measurements made by the ATLAS collaboration. The more precisely the luminosity is known, the lower the uncertainty on any given cross section measurement.

The luminosity of a pp collider can be expressed as

$$\mathcal{L} = \frac{\mu n_b f_r}{\sigma_{inel}}. \tag{2.2}$$

where μ is the number of inelastic interactions per crossing, n_b is the number of colliding bunch pairs, f_r is the machine revolution frequency, and σ_{inel} is the pp inelastic cross section.
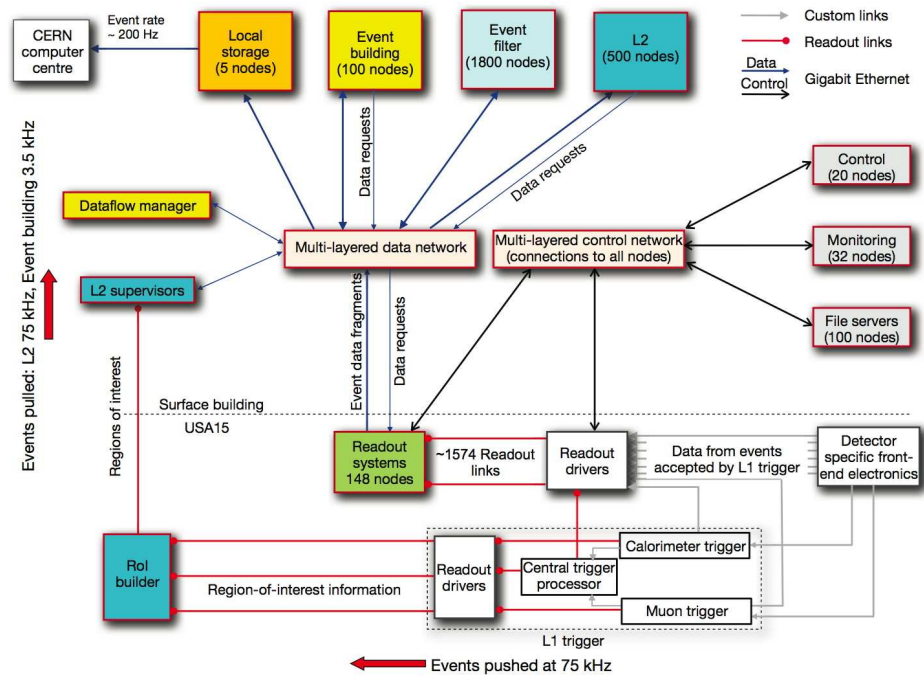
Figure 2.24: Block diagram of the ATLAS trigger and data acquisition systems. [2]

Given a particular detector and algorithm it is necessary to rewrite equation 2.2 as

$$\mathcal{L} = \frac{\mu_{vis} n_b f_r}{\sigma_{vis}} \tag{2.3}$$

where μ_{vis} is the interaction rate per bunch crossing measured by the detector and $\sigma_{vis} = \epsilon \sigma_{inel}$ where ϵ is the efficiency of the detector and algorithm [37].

The primary detector used in the 2011 and 2012 luminosity measurements was the beam conditions monitor (BCM). The BCM is made of eight detector modules, four on each side, located 184 cm from the nominal interaction point in z at a radius of 55 mm (a pseudorapidity of $\sim$4.2) [38]. Figure 2.26 depicts a BCM detector module as well as the beam pipe support structure on which the BCM is mounted. The BCM uses $\sim$1 cm^2 semiconducting diamonds to measure charged particle flux.

There are two luminosity algorithms used by the BCM. In the algorithm known as BCMH_EventOR an event will be counted if there is at least one hit on either side in one of the horizontally oriented modules. In BCMH_EventAND an event will be counted if there is at least one hit on each side of the detector. From the raw counts, N_{OR} and N_{AND}, accumulated in a certain time interval one can determine μ_{vis} using the following equations:

$$\frac{N_{OR}}{N_{BC}} = 1 - e^{-\mu_{vis}^{OR}} \tag{2.4}$$

$$\frac{N_{AND}}{N_{BC}} = 1 - 2e^{-(1+\sigma_{vis}^{OR}/\sigma_{vis}^{AND})\mu_{vis}^{AND}/2} + e^{-(\sigma_{vis}^{OR}/\sigma_{vis}^{AND})\mu_{vis}^{AND}} \tag{2.5}$$

where N_{BC} is the number of bunch crossings in the same time interval. σ_{vis} is determined using *Van der Meer (VdM)* scans as described in reference [39]. Figure 2.25 shows the output of the BCMH_EventOR algorithm over the course of a particular run.

The ATLAS detector is built to withstand a very harsh operating environment, however, beam accidents can happen that could damage or destroy its more sensitive components. In order to reduce the chances of this occurance there are several systems in place to detect anomalies in beam conditions and dump the beam if the situation reaches dangerous levels. The rate of false positives must be very low as dumping the beam unnecessarily wastes a significant amount of time (and money) for everyone involved. However, the system must catch every real dangerous situation, as losing a significant part of the detector could permanently cripple the ability of the ATLAS experiment to search for new physics.

In addition to beam loss monitors (BLMs) provided by the LHC around the entire ring, the ATLAS detector has two dedicated systems devoted to detector safety: its own BLM and the previously mentioned BCM.

The ATLAS BLM measures integrated particle flux over time scales of 40 μs to 80 s, and it sends an abort signal to the LHC if this exceeds a predefined threshold. There are seven ATLAS BLM modules located on each side of the interaction point located 65 mm
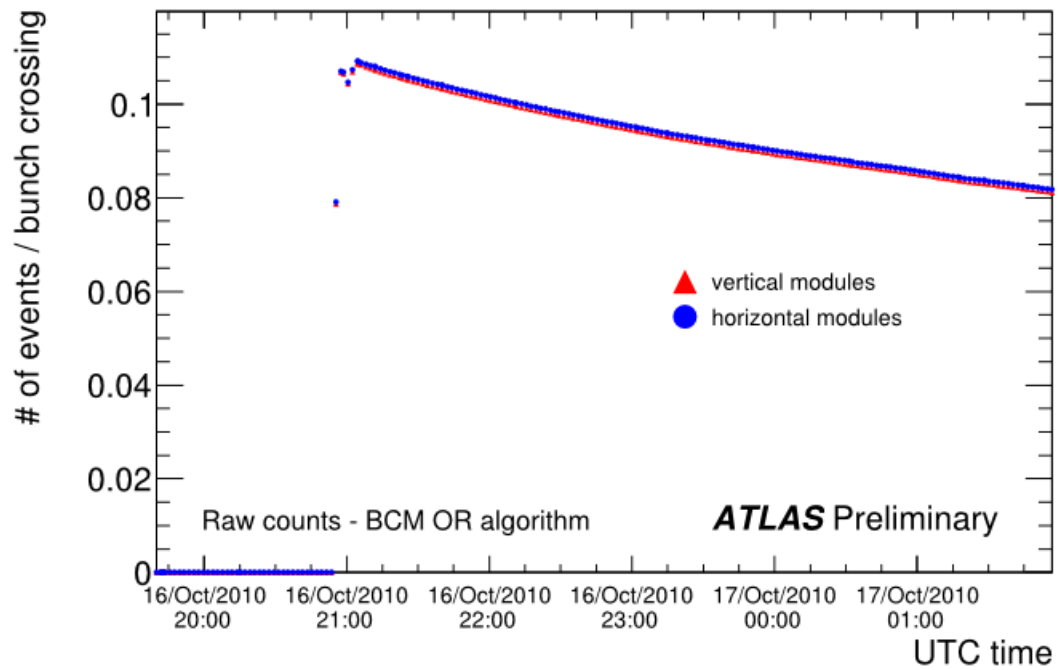
Figure 2.25: Average number of events per bunch crossing satisfying the OR algorithm condition versus time. For an event to satisfy the OR condition, it must contain a hit anywhere in BCM detector within the second half of the bunch interval. Event counts are averaged over all colliding bunches and scaled to one LHC turn [13].

from the beam at $z = 3450$ mm. The abort signal is sent if 3 or more modules on each side exceed the threshold.

In addition to the luminosity monitoring the BCM serves two other purposes. The primary purpose is to measure beam anomalies on much shorter timescales than the ATLAS BLM. The BCM can detect particle fluxes down to 1 minimum ionizing particle per cm^2 with a time resolution of less than 1 ns (see Figure 2.27. In principle it is also able to abort the beam if certain thresholds are exceeded, however, this capability has not been fully validated and is currently disabled. The BCM also records beam conditions leading up to and directly after every beam dump, whether planned or unplanned, and it classifies each dump as "clean" or "dirty". A dirty beam dump might require consultation with experts before allowing the beam to be reinjected. An example of what the BCM sees during a beam dump is shown in Figure 2.28. In 2010 I was Deputy Run Coordinator for the ATLAS BCM and BLM. My duties included making sure the BCM was running properly on a day to day basis and giving periodic status reports at the ATLAS Run Coordination meetings during the first year of 7 TeV running. I was also responsible for writing software for the BCM detector control system.

(a) A BCM Module.   (b) The BCM during installation.
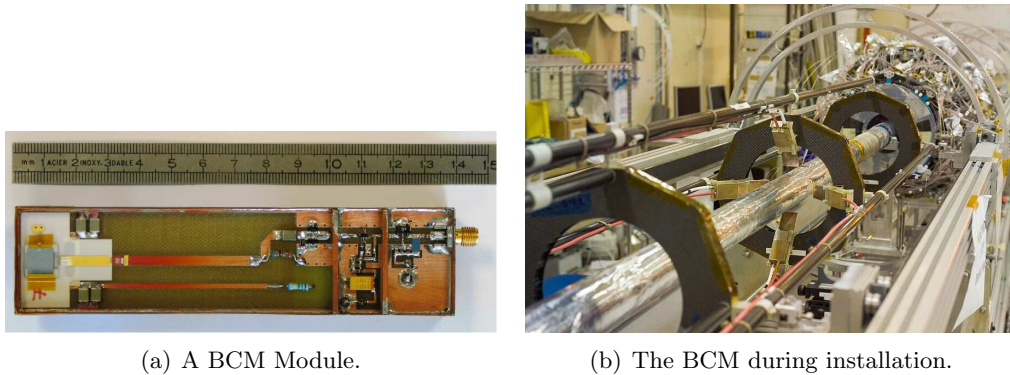
Figure 2.26: Left: Top view of a BCM module, showing the diamond sensors (left side of picture), the HV supply and signal-transmission lines, the two amplification stages and the signal connector (right side of picture). Right: Close-up view of one BCM station installed at 184 cm from the centre of the pixel detector, which can be seen at the far end of the picture. Each one of the four modules can be seen in position at a radius of 5.5 cm, very close to the beam-pipe. [2]
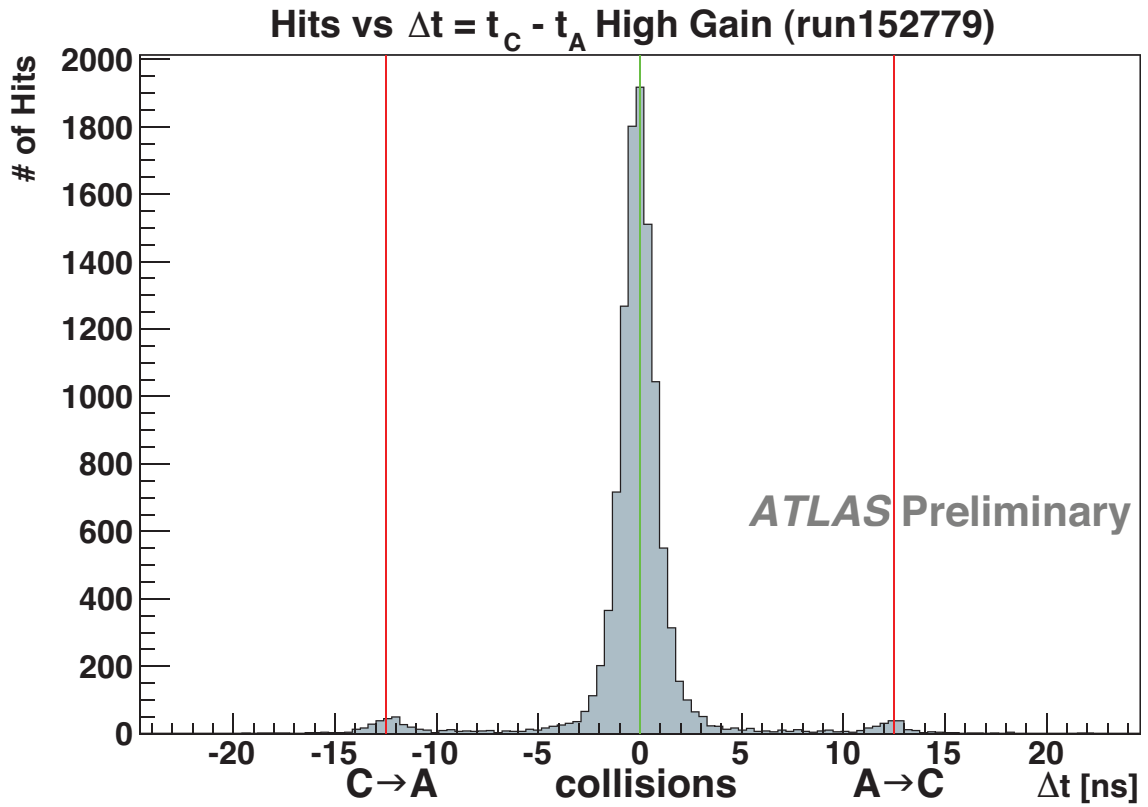
Figure 2.27: Distribution of events against difference of arrival times of hits on A and C side of BCM detector for run 152779. From difference of arrival times to both sides it is possible to distinguish collision and background coming from LHC beam 1 and beam 2. [13]
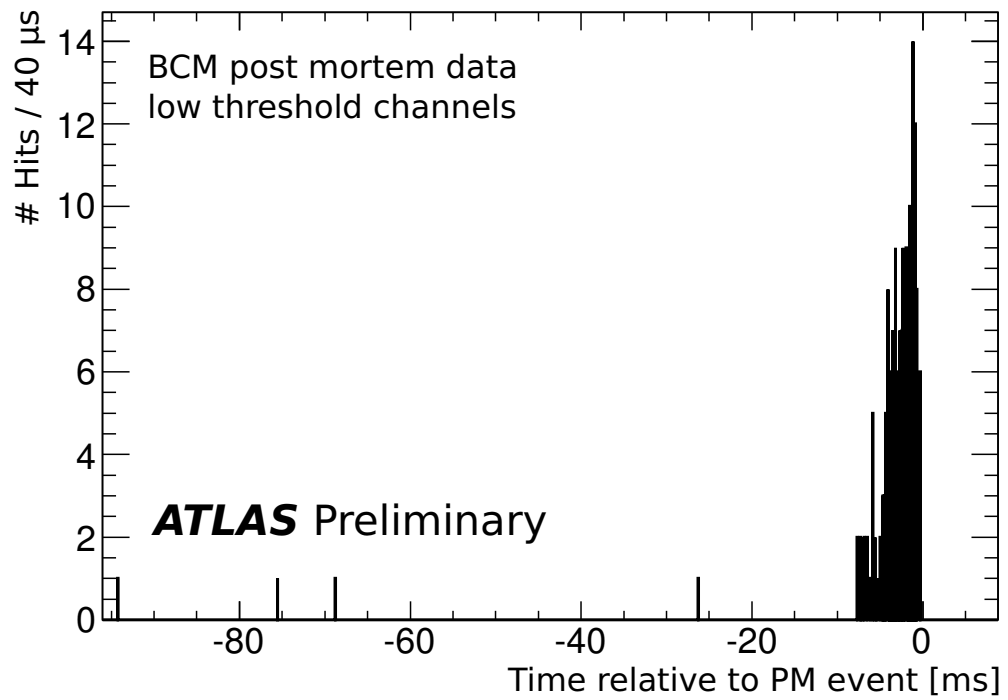
Figure 2.28: Signal seen at the LHC dump by ATLAS BCM on 26.3.2010 at 13:41 (Geneva local time). LHC was doing collimator studies at 3.5 TeV. Plot shows development of signal in low threshold channels from 90ms before to 10ms after the post mortem event. [13]

Chapter 3

THEORETICAL BACKGROUND - STANDARD MODEL

The current Standard Model of particle physics is an $SU(3)_C \otimes SU(2)_L \otimes U(1)_Y$ gauge theory that describes all known particles of matter and the interactions between them, except gravity. The unification of the electromagnetic and weak forces was achieved in the 1960s by Glashow, Weinberg, and Salam [40, 41, 42]. The principle of asymptotic freedom was first described in the 1970s by Gross, Wilczek and Politzer and QCD was added to the Standard Model to explain the strong force. The source of electroweak symmetry breaking and the origin of mass of the fermions and gauge bosons was not known (and still has not been confirmed), but the so-called Higgs mechanism (actually published nearly simultaneously by Higgs, Englert and Brout, and Guralnik, Hagen, and Kibble) was introduced in 1964 [43, 44, 45] and has been adopted by the Standard Model.

3.1 The Higgs Mechanism

Electroweak symmetry breaking in the Standard Model can be explained using the Higgs mechanism. Several examples that illustrate how this is accomplished are worked through below.

First an example of spontaneous symmetry breaking with a Lagrangian made up of simple kinetic and potential terms:

$$\mathcal{L} = \partial^\mu \varphi^* \partial_\mu \varphi - V(\varphi) \tag{3.1}$$

with the potential $V(\varphi)$ defined as

$$V(\varphi) = \mu^2 \left|\varphi\right|^2 + \lambda \left|\varphi\right|^4 \tag{3.2}$$

with a mass term proportional to μ^2 and a self-coupling term proportional to λ. λ must be positive for the potential to be bounded from below. φ is a complex scalar field of the form

$$\varphi = \frac{1}{\sqrt{2}}(\varphi_1 + i\varphi_2). \tag{3.3}$$

By minimizing V the vacuum state can be obtained.

$$V'(\varphi) = \mu^2 + \lambda(\varphi_1^2 + \varphi_2^2) = 0 \tag{3.4}$$

If $\mu^2 > 0$, V has a minimum only at $\varphi = 0$, and no symmetry is broken. However, if we require $\mu^2 < 0$, V is a minimum along a circle of radius v in the (φ_1, φ_2) plane

$$v^2 = \varphi_1^2 + \varphi_2^2 = \frac{-\mu^2}{\lambda}. \tag{3.5}$$

We now choose one of the minima, breaking the symmetry of the solutions, at $\varphi_1 = v, \varphi_2 = 0$ φ can be expanded around this vacuum state in terms of the real scalar fields σ and η

$$\varphi = \frac{1}{\sqrt{2}}(v + \sigma + i\eta). \tag{3.6}$$

We can use this to rewrite our Lagrangian, neglecting interaction terms as

$$\mathcal{L} = \frac{1}{2}\partial^\mu\sigma\partial_\mu\sigma - \frac{1}{2}2\lambda v^2\sigma^2 + \frac{1}{2}\partial^\mu\eta\partial_\mu\eta. \tag{3.7}$$

The form of this Lagrangian is that of a free Lagrangian for a massive σ and a massless η, with $m_\sigma = \sqrt{2\lambda}v$.

We can now apply this technique to a slightly more complicated situation, a theory with local gauge symmetry. Our Lagrangian must be invariant under transformations of the form $\varphi(x) \to \exp^{i\alpha(x)} \varphi(x)$. In order to make our Lagrangian gauge invariant the normal derivative is replaced by the covariant derivative

$$D_\mu = \partial_\mu + iqA_\mu. \tag{3.8}$$

The A_μ field from the covariant derivative transforms as $A_\mu \to A_\mu + \frac{1}{q}\partial_\mu\alpha(x)$ and adds another kinetic term to the Lagrangian

$$\mathcal{L} = D^\mu\varphi^* D_\mu\varphi - V(\varphi) - \frac{1}{4}F_{\mu\nu}F^{\mu\nu} \tag{3.9}$$

$$F_{\mu\nu} = \partial_\mu A_\nu - \partial_\nu A_\mu. \tag{3.10}$$

Applying spontaneous symmetry breaking in this situation results in massive scalar and vector bosons (σ and A_μ) and a massless scalar, η, however, the massless particle can be eliminated by choosing the unitary gauge. In this gauge $\varphi(x) = \frac{1}{\sqrt{2}}[v + \sigma(x)]$ and the

Lagrangian is

$$\mathcal{L} = \frac{1}{2}\partial^\mu\sigma\partial_\mu\sigma - \lambda v^2\sigma^2 + \frac{1}{2}q^2v^2 A_\mu A^\mu - \frac{1}{4}F_{\mu\nu}F^{\mu\nu} + \text{higher order terms.} \qquad (3.11)$$

The form of this Lagrangian implies a massive scalar σ and a massive vector A_μ. This is the Higgs mechanism that assigns mass to the electroweak vector bosons $(W^\pm, Z)$ when applied to the full electroweak Lagrangian. In that case there are three massive vector bosons (W) and one massless vector boson, γ, that have all been seen experimentally, but like the simpler theory, there is also a predicted massive scalar boson. This is the Higgs boson, with a mass $m_H = \sqrt{2\lambda}v$. The vacuum expectation value $v = \frac{2m_W}{g} = 246$ GeV is well known, but the Higgs self-coupling constant λ, and therefore the mass, is, within certain limits, a free parameter. Precision electroweak measurements have constrained the mass of a SM Higgs to be less than ~ 185 GeV at the 95% CL [46].

3.2 $Z\gamma$ production in the Standard Model

The production of $Z\gamma$ final states in the SM is described by the three Feynman diagrams in Figure 3.1. Standard Model production of $Z\gamma$ arises from two different processes, initial state radiation (ISR) and final state radiation (FSR). In ISR the photon is radiated by one of the quarks during Z production, while in FSR the photon is radiated by one of the charged leptons coming from the decay of the Z.

Figure 3.2 shows the cross sections for a variety of SM processes, including $Z\gamma$. The plot shows both the theoretical prediction and the measurement using 35 pb^{-1} of ATLAS data. The cross sections shown do not include the branching ratios of the vector bosons to leptons. All of the ATLAS results are in agreement with the Standard Model predictions within the uncertainties of the measurements. The goal of the analysis presented in the next chapter is to reproduce the measurement of the $Z\gamma$ cross section with 4.5 fb^{-1} of data.
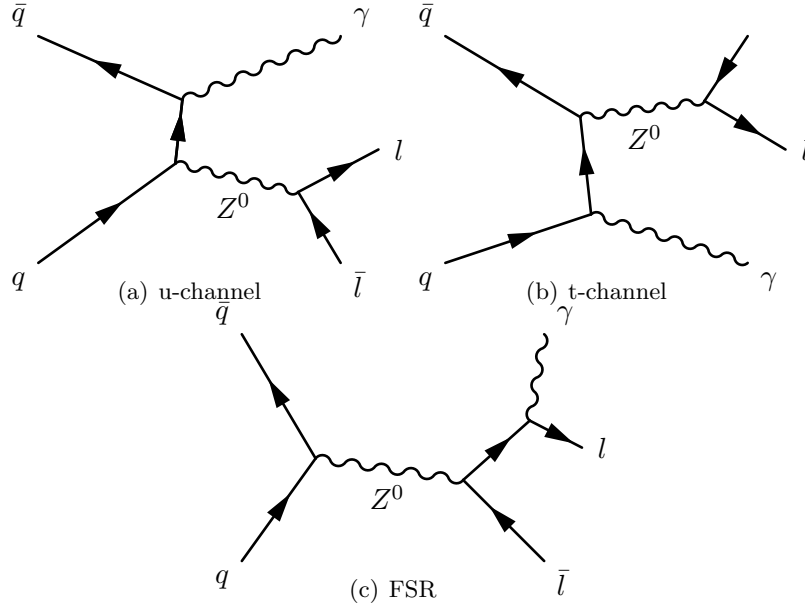
Figure 3.1: Feynman diagrams for Standard Model $Z\gamma$ production. Two diagrams contribute to ISR, u-channel and t-channel, and one to FSR.
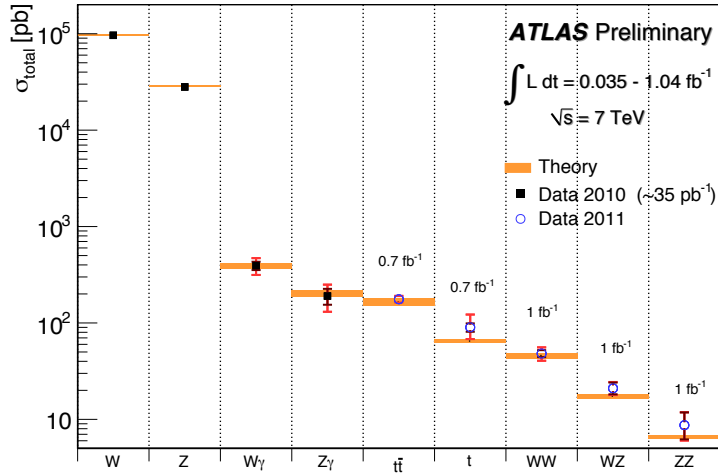
Figure 3.2: The W and Z vector boson inclusive cross sections and the $W\gamma$ and $Z\gamma$ diboson cross sections were measured with about 35 pb^{-1} of integrated luminosity from the 2010 dataset. The top quark pair production cross-section is based on a statistical combination of measurements using dilepton final states with 0.70 fb^{-1} of data and single-lepton final states with 35 pb^{-1} of data. The remaining measurements were made with the first ~ 1 fb^{-1} from the 2011 dataset. The dark error bar represents the statistical uncertainly. The red error bar represents the full uncertainty, including systematics and luminosity uncertainties. All theoretical expectations were calculated at NLO or higher [14].

41

Chapter 4

MEASURING THE STANDARD MODEL $pp \rightarrow Z + \gamma$ CROSS-SECTION

Obtaining a precise measurement of the production cross-section of a Z boson in association with a photon is important as a check on the Standard Model. This cross section is predicted by the Standard Model, and it can be be precisely calculated from the theory. Deviations from the predicted cross section could point to physics beyond the Standard Model. Previous ATLAS results shown in figure 3.2 are in agreement with the Standard Model within the uncertainties of the measurements, but with more data it is possible to increase the precision of a measurement. In addition to possible direct evidence of new physics, measuring this cross-section is important because it is a background to other process such as Higgs bosons or technicolor hadrons decaying to $Z + \gamma$.

4.1 Event Selection

In order to measure the cross-section, events containing a Z boson and a photon need to be identified. The event has to satisfy a high transverse momentum lepton trigger. This reduces the number of collision events that need to be analyzed in more detail because events that do not satisfy one of these triggers are very unlikely to contain leptons from Z decays. In order to maximize acceptance and efficiency, the lowest unprescaled single lepton trigger was used for each data period. Because the runs in later data periods had higher instantaneous luminosity, the momentum thresholds on the lowest unprescaled single lepton triggers were increased.

The $Z + \gamma$ candidate events consist of a pair of opposite sign, isolated leptons (either electrons or muons) and an isolated photon. The isolation requirement reduces the chance of counting a jet as a lepton or photon. The invariant mass of the lepton pair is required to be greater than 40 GeV and the transverse momentum of the photon has to be greater than 15 GeV. First the Z boson is reconstructed.

Periods	Run numbers	Dates	muon trigger	electron trigger
D - I	179710 - 186493	4/14 - 7/29	EF_mu18_MG	EF_e20_medium
J	186516 - 186755	7/30 - 8/4	EF_mu18_MG_medium	EF_e20_medium
K	186873 - 187815	8/4 - 8/22	EF_mu18_MG_medium	EF_e22_medium
L - M	188902 - 191933	9/7 - 10/30	EF_mu18_MG_medium	EF_e22vh_medium1

Table 4.1: 2011 data periods and lepton triggers.

- Select Z candidates (electron channel)

  - two "medium++" quality electron candidates with $p_T(e) > 25$ GeV [47]

  - the electron candidates must have opposite charge

  - the invariant mass of the electron pair M_{ee} must be greater than 40 GeV

- Select Z candidates (muon channel)

  - two muon candidates with $p_T(\mu) > 25$ GeV

  - the muon candidates must have opposite charge

  - invariant mass of the muon pair $M_{\mu\mu} > 40$ GeV

Once the event has passed the Z boson selection criteria, we then search for a photon candidate in the event. The selection cuts for the photon candidate are:

- $p_T(\gamma) > 15$ GeV

- not located in the regions of the LAr calorimeter that suffer from readout problems due to bad OTX or in the LAr hole.

- $| \eta(\gamma) |< 2.37$ (excluding the crack region $1.37 <| \eta(\gamma) |< 1.52$)

- $\Delta R(e/\mu, \gamma) > 0.7$, the distance between lepton and photon in (η, ϕ) space

- pass tight photon ID cut

- isolated : $EtCone30\_corrected(\gamma) < 6$ GeV (corrected for photon energy leakage and energy from underlying events)

The event counts after all selection cuts are given for a series of transverse momentum ranges in Table 4.2.

E_T^γ interval [GeV]	$Z(e^+, e^-)\gamma$		$Z(\mu^+, \mu^-)\gamma$	
	$N_{Jet} \geq 0$	$N_{Jet} = 0$	$N_{Jet} \geq 0$	$N_{Jet} = 0$
$15 \leq E_T^\gamma < 20$	705	576	997	817
$20 \leq E_T^\gamma < 30$	631	485	948	719
$30 \leq E_T^\gamma < 40$	226	154	349	243
$40 \leq E_T^\gamma < 60$	198	129	259	164
$60 \leq E_T^\gamma < 100$	105	73	151	99
$100 \leq E_T^\gamma < 1000$	40	15	50	21

Table 4.2: Total number of events observed in data passing all analysis selection cuts for the $Z + \gamma$ measurement in both electron and muon decay channels.

4.1.1 Muon Reconstruction and Identification

There are two primary independent algorithms used for muon reconstruction in ATLAS, STACO and MuID. For this analysis only STACO muons will be used. A STACO muon candidate is reconstructed by matching a track in the Inner Detector with a track in the Muon Spectrometer. There are three different levels of muon quality in order of increasing purity and decreasing efficiency: loose, medium, and tight. Only tight muons are used in this analysis.

The transverse momentum of the muon is required to be greater than 25 GeV. Since the trigger threshold is 18 GeV this ensures a high muon trigger efficiency. The muon must have a pseudorapidity of $|\eta| < 2.4$. There is an isolation requirement on the muon that requires that the transverse momentum sum of all tracks within a cone of 0.3 radians around the muon track be less than 15% of the transverse momentum of the muon itself.

4.1.2 Electron Reconstruction and Identification

The reconstruction of an electron candidate can be seeded either from the electromagnetic calorimeter or from the Inner Detector. The algorithm for reconstructing high transverse momentum electrons (which includes most electrons in this analysis) uses clusters in the calorimeter as seeds. These clusters are found using a sliding window mechanism. These clusters are then matched to tracks by comparing the η and ϕ of the cluster to that of the origin of the track. If a track is close enough in η and ϕ it is extrapolated into the calorimeter and the distance $(\Delta\eta, \Delta\phi)$ from the cluster is calculated. The track with the closest match is used to create the electron object. The electron can be classified as loose, medium, or tight depending on differences in shower shape variables, Inner Detector hit requirements, and the $(\Delta\eta, \Delta\phi)$ threshold allowed from the cluster. The tight electrons have the highest purity but relatively low efficiency, while the loose electrons have the highest efficiency but lower purity; the medium electrons sit between tight and loose in both efficiency and purity.

The electrons used in the cross-section measurement were required to pass the medium criteria.

The momentum threshold on the lowest unprescaled electron trigger is either 20 or 22 GeV, depending on the data period (see table 4.1. The transverse momentum of the selected electrons is required to be greater than 25 GeV which is consistent with the muon requirement and has a reasonably high trigger efficiency. The electron is required have a pseudorapidity of $|\eta| < 2.47$ excluding the transition region between calorimeters at $1.37 < |\eta| < 1.52$. The isolation requirement for an electron is that the transverse energy deposited in the calorimeter in a cone of radius 0.3 around the electron cluster is less than 6 GeV.

4.1.3 Photon Reconstruction and Identification

Photons in ATLAS can be either converted or unconverted. Converted photons produce a positron/electron pair somewhere inside the Inner Detector volume, thus leaving tracks. Unconverted photons do not leave tracks in the Inner Detector. Clusters are found in the electromagnetic calorimeter in the same way as for electrons. If the cluster has no associated track within certain limits in $(\Delta\eta, \Delta\phi)$ it is considered an unconverted photon. If there is a track associated with the cluster then it can be either an electron or a converted photon. The ambiguity between electrons and converted photons is resolved through differences in shower shape and track parameter variables. To separate photons from jets, the leakage into the hadronic calorimeter is used. Background photons from π^0 and η decays can be rejected with a calorimeter isolation cut.

In the data the photon transverse energy is corrected with an energy scale that is obtained from resonances such as $Z \to e^+e^-$, $J/\psi \to e^+e^-$ or E/P studies using isolated electrons from $W \to e\nu$ [47]. This correction is performed using a software tool developed by the ATLAS e/γ performance group. For the simulated events, the photon transverse energy is smeared using another software tool that accounts for difference in energy resolution compared to data.

Some of the shower shape variables used to determine photon quality are listed below. They will also be used in the data driven background esimation described later.

- R_{had}: ratio of ET in the first layer of the hadronic calorimeter to the ET of the EM cluster. In the pseudorapidity range $0.8 < |\eta| < 1.37$ which is not covered by the first hadronic layer, it is the ratio of the total hadronic E_T to the EM E_T.

- **EM Middle Layer Variables**:

    - R_η: ratio in η of cell energies in 3×7 versus 7×7 cells.
    - w_2: lateral width of the shower,

- R_ϕ: ratio in ϕ of cell energies in 3×7 versus 7×7 cells.

- **EM First (Strip) Layer Variables**:

  - w_{s3}: shower width for three strips around maximum strip,

  - w_{stot}: total lateral shower width,

  - F_{side}: fraction of energy outside a core of 3 central strips, but within 7 strips,

  - ΔE: difference between the energy of the strip with the second largest energy deposited and the energy of the strip with the smallest energy deposit between the two leading strips,

  - $Eratio$: ratio of the energy difference associated with the largest and second largest energy deposits over the sum of these energies.

A transverse momentum cut of 15 GeV is applied to the photon as well as requiring that the transverse energy deposited in the calorimeter in a cone of 0.3 radians around the photon candidate be less than 6 GeV. The pseudorapidity of the photon must be $|\eta| < 2.37$ excluding the same calorimeter transition region as for electrons.

4.2 Background Estimation

The primary background to this process comes from jets faking photons. Most of these events can be rejected using isolation and hadronic leakage cuts, however, some $Z + jets$ events still remain. This background can be estimated from data using the ABCD method (also known as the 2D sideband method). Using this method the data is plotted in two dimensions, one dimension is the photon isolation energy (EtCone40), the other is the photon identification quality.

The data is split into four regions

- Region A - $EtCone40 < 6$ GeV and the photon is "tight", signal region

- Region B - $EtCone40 > 7$ GeV and the photon is "tight", control region

- Region C - $EtCone40 < 6$ GeV and the photon is not "tight", control region

- Region B - $EtCone40 > 7$ GeV and the photon is not "tight", control region

The EtCone40 variable is the energy deposited in the calorimeter in a cone of radius 0.4 in (η, ϕ) space around the photon. A photon is considered tight if it passes a series of cuts on discriminating variables relating to hadronic leakage and shower shape in the first and second layer of the calorimeter. These cuts are determined by the ATLAS e/gamma performance group. For the purposes of this analysis a photon is considered not tight if it
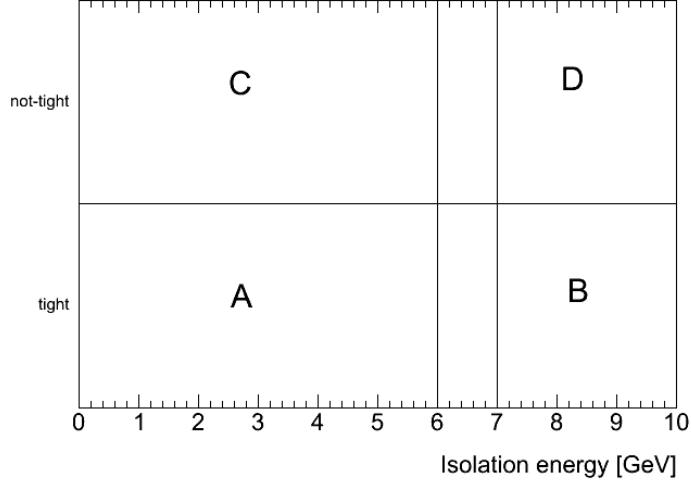
Figure 4.1: The 2 dimensions of the ABCD method.

passes all of the cuts related to hadronic leakage and the second calorimeter layer shower shape cuts, but fails at least 2 out of 4 of the first layer shower shape cuts.

Assuming that the two dimensions are uncorrelated and there is no signal leakage into any of the control regions, the ratio of events N_B/N_D is the same as the ratio N_A^{Bkgd}/N_C. However, there is signal leakage, and the two dimensions are not completely uncorrelated. This leads to a slightly more complicated formula:

$$N_A^{Z\gamma} = N_A - \frac{1}{R^{MC}} \frac{(N_B - c_B N_A^{Z\gamma})(N_C - c_C N_A^{Z\gamma})}{N_D - c_D N_A^{Z\gamma}} \tag{4.1}$$

Where $N_A^{Z\gamma}$ is the number of signal events in region A, and N_A is the total number of events observed in region A. This can be solved for the number of background events in region A:

$$N_A^{Zjet} = N_A - \frac{E(-1 - \sqrt{1 + F})}{G} \tag{4.2}$$

with

$$E = N_D + N_A c_D - N_B c_C / R^{MC} - N_C c_B / R^{MC} \tag{4.3}$$

$$F = \frac{4(c_B c_C / R^{MC} - c_D)(N_A N_D - N_C N_B / R^{MC})}{E^2} \tag{4.4}$$

$$G = 2(c_B c_C / R^{MC} - c_D) \tag{4.5}$$

c_X is the ratio of signal events found in region X to the number of signal events found in

47

region A as estimated using $Z\gamma$ Monte Carlo.

$$c_X = \frac{N_X^{MC_{Z\gamma}}}{N_A^{MC_{Z\gamma}}}$$
(4.6)

R^{MC} is a measure of the correlation in the background between the two dimensions. For the nominal background calculation it is set to one with variations accounted for with a systematic uncertainty.

$$R^{MC} = \frac{N_B^{Zjet} N_C^{Zjet}}{N_A^{Zjet} N_D^{Zjet}}$$
(4.7)

The distributions in the two dimensions of the ABCD method are shown in Figure 4.2.
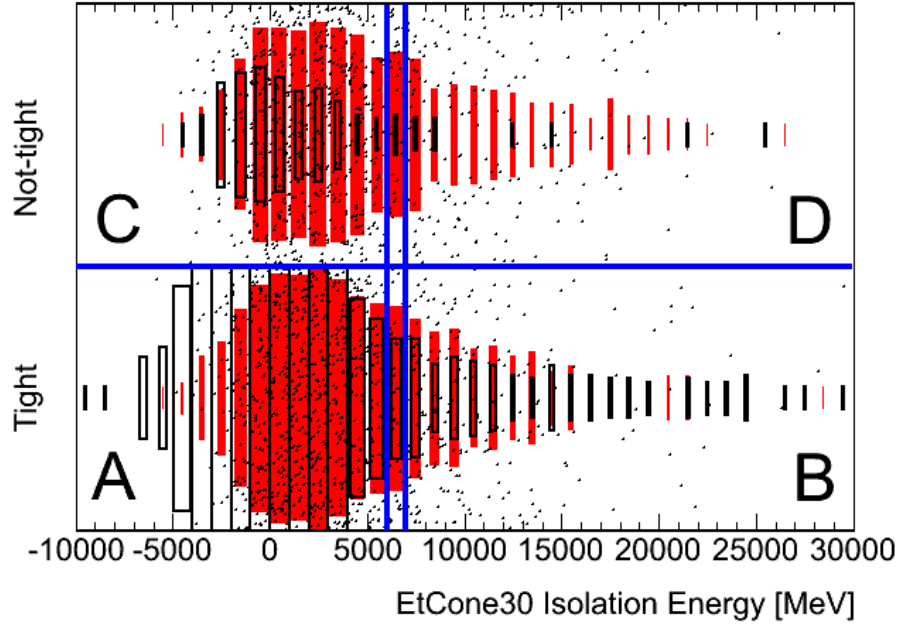
Figure 4.2: The red boxes are Z + jets MC, black boxes are $Z\gamma$ MC and black points are data.

Uncertainty on the background estimate is both statistical and systematic. Systematic error was estimated in several different ways. The systematic error from R^{MC} was calculated to be 1.49% for the muon case and 4.57% for the electron case. Changing the definition of "not tight" by requiring the photon candidate to fail either one out of four or two out of five first layer shower shape cuts yielded a maximum variation of 2.28% for the muon case and 4.37% for the electron case. The boundaries of the isolated and non-isolated regions

Region	$Z(e^+, e^-)\gamma$		$Z(\mu^+, \mu^-)\gamma$	
	N	c_X	N	c_X
A	1907		2756	
B	114	$(1.52 \pm 0.17) \times 10^{-2}$	197	$(1.67 \pm 0.15) \times 10^{-2}$
C	234	$(1.93 \pm 0.19) \times 10^{-2}$	432	$(9.25 \pm 0.36) \times 10^{-2}$
D	73	$(9.28 \pm 4.16) \times 10^{-4}$	83	$(2.19 \pm 0.53) \times 10^{-3}$

Table 4.3: Total number of events observed in data in the four regions of the ABCD method as well as the c_X parameters. Only statistical errors shown.

were varied up and down by 1 GeV, while maintaining the gap between the regions, yielding systematic error of 1.29% and 1.71% for muons and electrons respectively.

4.3 Efficiency

In order to accurately calculate the cross-section it is necessary to know how the number of leptons and photons identified in the final analysis relates to the number of leptons and photons originally generated in the collisions. The ratio of these numbers is the efficiency.

4.3.1 Trigger Efficiency

The trigger efficiency measures the likelihood of an event to fire the trigger as a function of lepton transverse momentum. Because an event that contains a Z has two leptons it is more likely to fire the trigger than an event with a single lepton. The trigger efficiency is calculated with respect to leptons that pass the offline selection cuts. Figure 4.3 shows the trigger efficiency for one of the triggers used in this analysis for single electrons as a function of transverse momentum. Figure 4.4 show similar plots for muons separately in the barrel and endcap regions.

4.3.2 Identification Efficiency

The lepton identification efficiency is determined from signal Monte Carlo. To correct for differences between MC and data the tag and probe method was used on data. The tag is a well identified lepton. For electrons the probe is a cluster in the electromagnetic calorimeter without the strict identification criteria, and for muons the probe is a low quality (loose) muon. The only requirement is that the dilepton invariant mass be at the mass of the Z. The data-driven efficiency is calculated by seeing how many probe leptons pass the selection criteria. Photon efficiency is also calculated from Monte Carlo simulations with corrections to shower shape variables to account for differences between data and MC.
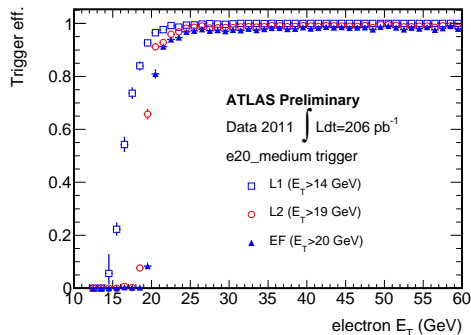
Figure 4.3: Electron trigger efficiencies for EF_e20_medium. [15]
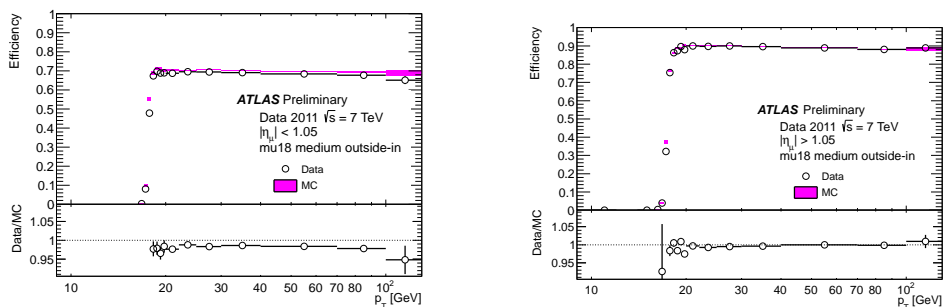
(a) Barrel

(b) Endcap

Figure 4.4: Muon trigger efficiencies for EF_mu18_medium. [16]

4.3.3 Systematic Error

Systematic error on the efficiency comes from a variety of sources including energy and momentum resolution, measurement of isolation, and differences in reconstruction and identification efficiencies between data and simulations. The dominant systematic in both the electron and muon channels comes from uncertainty on the photon identification efficiency. This was estimated to be 5% by the ATLAS e/gamma group [48]. Adding the different systematic error contributions in quadrature yielded 5.02% and 5.46% for the muon and electron channels, respectively. The photon identification efficiency is measured using three different data driven techniques. The first method uses a relatively pure photon sample obtained from radiative decays of the Z boson. The second method uses electrons from Z decays and exploits the similarity between electron showers and converted photon showers. The third method, known as the matrix method, uses track isolation to determine sam-

50

Systematic	$Z(e^+, e^-)\gamma$	$Z(\mu^+, \mu^-)\gamma$
Lepton ID	0.24%	2.12%
Lepton Energy (e) or momentum (μ) scale/resolution	0.01%	0.17%
Photon Energy scale/resolution	0.09%	0.15%
Lepton Isolation	0.33%	0.40%
Photon Isolation	0.24%	0.22%
Photon ID	5%	5%

Table 4.4: Contributions to systematic error on signal efficiency for electron and muon channels.

ple purity before and after the "tight" criteria are applied. The three methods apply to different, but overlapping, transverse energy ranges. The first method applies from 15 to 50 GeV, the second from 20 to 80 GeV, and the third from 20 to 300 GeV. In the overlapping regions the three methods provide consistent efficiencies within the uncertainty on the measurements. The combined uncertainty on the photon efficiency from all three methods depends on both the transverse energy and pseudorapidity of the photon candidate. The value ranges from 5% at low E_T to 1-2% at higher E_T and generally being larger at higher η. A conservative estimate of 5% for the entire range in E_T and η has been applied for the analysis presented in this thesis.

4.4 Cross-section calculation

The cross-section is calculated according to the following equation

$$\sigma_{pp \to l^+l^-\gamma}^{ext-fid} = \frac{N_{sig}^{Z\gamma}}{A_{Z\gamma} \cdot C_{Z\gamma} \cdot L} \tag{4.8}$$

$N_{Z\gamma}^{sig}$ is the number of events passing all the selection cuts after subtracting the number of background events estimated from the ABCD method. L is the integrated luminosity of the data being analyzed. $C_{Z\gamma}$ is the correction factor used to account for the trigger, reconstruction, and identification efficiences and is defined as the ratio of simulated signal events passing selection cuts to signal events generated in the kinematic and geometric fiducial phase space. $A_{Z\gamma}$, the acceptance factor, is calculated as the ratio of events generated in the fiducial region to the total number of events generated in the extended fiducial region. Since $N_{Z\gamma}^{sig}$ is a calculated number, its uncertainty is not simply equal to $\sqrt{N}$. The uncertainty on $N_{Z\gamma}^{sig}$ has been calculated by combining the uncertainty for each contribution to equation 4.2 with the assumption that the errors on N_A, N_B, N_C, N_D, C_B, C_C, and C_D are uncorrelated. The error on the number of data events in each the four regions

was assumed to be the square root of the number of events in each region. The errors on the signal leakage factors, C_X, were found by taking the sum in quadrature of the square root of the number of MC signal events in region A and region X. This results in a higher than expected statistical uncertainty on the cross section measurement. Since the analysis described in this thesis uses ~5 times the the data of the earlier ATLAS measurement the statistical error should be lower, but as seen in table 4.7 this is not the case.   The measured

Fiducial Cross Section		
Cuts	$e^+e^-\gamma$	$\mu^+\mu^-\gamma$
Lepton $E_t(p_T)$	$E_T^e > 25$ GeV	$p_T^\mu > 25$ GeV
Lepton η	$|\eta_e| < 2.47$ excluding $1.37 < |\eta_e| < 1.52$	$|\eta_\mu| < 2.4$
Boson mass	$m_{ee} > 40$ GeV	$m_{\mu\mu} > 40$ GeV
Photon	$E_T^\gamma > 15$ GeV	
	$|\eta_\gamma| < 2.37$	(excluding $1.37 < |\eta_\gamma| < 1.52$)
	$\Delta R(l,\gamma) > 0.7$	
	photon isolation fraction $\epsilon_h^p < 0.5$	
Extended fiducial Cross Section		
Cuts	$e^+e^-\gamma$	$\mu^+\mu^-\gamma$
Lepton $E_t(p_T)$	$E_T^e > 25$ GeV	$p_T^\mu > 25$ GeV
Lepton η	$|\eta_e| < 2.47$	$|\eta_\mu| < 2.47$
Boson mass	$m_{ee} > 40$ GeV	$m_{\mu\mu} > 40$ GeV
Photon	$E_T^\gamma > 15$ GeV	
	$|\eta_\gamma| < 2.37$	
	$\Delta R(l,\gamma) > 0.7$	
	photon isolation fraction $\epsilon_h^p < 0.5$	

Table 4.5: Definition of the fiducial regions where the measurements are performed and the extended region (common to all measurements) where the total cross sections are evaluated, where ϵ_h^p is defined at particle level as the ratio between sum of the energies carried by final state particles in the cone $\Delta R < 0.4$ around the photon and the energy carried by the photon.

values can be compared to theoretical predictions for the Standard Model.

4.5 Summary

The $pp \to Z + \gamma$ cross-section has been measured using 4.7 fb^{-1} of data from the ATLAS detector. It was found to be $1.26 \pm 0.07(stat.) \pm 0.07(syst.)$ pb when the Z boson decays to electrons and $1.24 \pm 0.07(stat.) \pm 0.11(syst.)$ pb when it decays to muons. These measure-

	$Z(e^+, e^-)\gamma$	$Z(\mu^+, \mu^-)\gamma$
N_{sig}	$1594 \pm 81(stat.) \pm 104(syst.)$	$2313 \pm 123(stat.) \pm 71(syst.)$
$A_{Z\gamma}$	$0.827 \pm 0.009(stat.)$	$0.912 \pm 0.009(stat.)$
$C_{Z\gamma}$	$0.330 \pm 0.005(stat.) \pm 0.018(syst.)$	$0.440 \pm 0.006(stat.) \pm 0.022(syst.)$

Table 4.6: Number of events in data after background subtraction with acceptance and correction factors for 4.7 fb^{-1}.

	$Z(e^+, e^-)\gamma$ [pb]	$Z(\mu^+, \mu^-)\gamma$ [pb]
Theory (MCFM)	$1.22 \pm 0.05(syst.)$	$1.22 \pm 0.05(syst.)$
ATLAS 1 fb^{-1}	$1.32 \pm 0.07(stat.) \pm 0.16(syst.)$	$1.27 \pm 0.06(stat.) \pm 0.15(syst.)$
This thesis 4.7 fb^{-1}	$1.26 \pm 0.07(stat.) \pm 0.07(syst.)$	$1.24 \pm 0.07(stat.) \pm 0.11(syst.)$

Table 4.7: Theoretical (from the MCFM generator) and measured extended fiducial cross-section times branching fraction. Luminosity errors are not included in the measured values and are 3.7% for the ATLAS 1 fb^{-1} result and 1.8% for the result presented in this thesis.

ments are in good agreement with the Standard Model prediction of $1.22 \pm 0.05(syst.)$ pb for each channel.

Chapter 5

Theoretical Background - Technicolor

5.1 Introduction

The Standard Model (SM) of particle physics does a very good job of describing reality as observed in particle physics experiments over the last several decades. However, there is one very important part of the SM that has not yet been observed. In order to account for electroweak symmetry breaking and the origin of mass (primarily the mass of the W and Z bosons, but also the fermion masses through a later extension), a massive scalar boson, known as the Higgs boson was introduced. The mass of this boson is not strictly determined by the theory, though there are constraints imposed through the implied effect its existence would have on various precision electroweak measurements.

While the Higgs boson is considered to be a part of the Standard Model, there are other theories that have been proposed that can account for electroweak symmetry breaking in different ways. One of the issues that the Higgs does not address is what is known as the hierarchy problem. The problem is that in the Standard Model there is no explanation for why the electroweak energy scale is so much lower than the Planck scale, or alternatively, why the mass of the Higgs boson is about 26 orders of magnitude below the Planck mass.

One set of theories that attempts to avoid the hierarchy problem while still explaining electroweak symmetry breaking is technicolor. Technicolor was first introduced in the 1970s [49, 26, 29]. It posits the existence of a new strong interaction analagous to QCD in which the electroweak energy scale arises naturally out of the theory rather than having to be put in by hand.

5.2 Symmetry breaking in QCD

As a precursor to the discussion of technicolor in the next section, it is interesting to look at a way to break electroweak symmetry without a new scalar Higgs field. This can be done

in a simplified model using QCD dynamics [50].

Let us assume an $SU(3)_c \otimes SU(2)_L \otimes U(1)_Y$ theory that contains one generation of massless quarks, u and d. The left and right handed quark fields are

$$Q_L^a = \begin{pmatrix} u^a \\ d^a \end{pmatrix}, u_R^a, d_R^a \tag{5.1}$$

where a is the color index and runs from 1 to 3. The left handed quarks are a doublet of $SU(2)_L$ and have weak hypercharge $Y = \frac{1}{3}$, while the right handed quarks are singlets and have weak hypercharge $Y = \frac{4}{3}$ and $Y = \frac{-1}{3}$ respectively.

Assuming the $SU(3)_c$ interaction is dominant the Lagrangian has an exact $SU(2)_L \otimes SU(2)_R$ chiral symmetry. In other words the the Lagrangian is invariant under independent rotations of the left handed and right handed components by independent 2×2 unitary matrices. At an energy scale $\sim \Lambda_{QCD}$ quark condensates, $\langle \bar{q}q \rangle$, are formed. The chiral symmetry $SU(2)_L \otimes SU(2)_R$ is broken, leaving the isospin flavor symmetry $SU(2)_V$. Because of this spontaneously broken symmetry three massless Goldstone bosons appear. In the full QCD theory these are pseudo-Goldstone bosons and are identified as the pions.

The pions are connected to the vacuum by the charged weak currents J_j^ν

$$\langle 0 \left| J_j^\nu \right| \pi_k(q) \rangle = i\delta_{jk} f_\pi q^\nu, \tag{5.2}$$

with the pion decay constant determined experimentally to be $f_\pi \approx 92.4$ MeV (this convention follows that used by Peskin and Schroeder [51] and differs by a factor of $\sqrt{2}$ from that used by the Particle Data Group [52]). In the simplified QCD examined here with massless u and d it is expected that f_π would be slightly smaller, and in the model of Quigg and Schrock it is estimated to be $f_\pi \approx 87$ MeV [50].

The $\langle \bar{q}q \rangle = \langle \bar{q}_L q_R + \bar{q}_R q_L \rangle \neq 0$ condensate links left and right handed quarks. The condensate will transform as a doublet of $SU(2)$ with weak hypercharge $|Y| = 1$. This also breaks the $SU(2)_L \otimes U(1)_Y$ symmetry to $U(1)_{EM}$.

In a process similar to the standard Higgs mechanism, the three massless Goldstone bosons become the longitudinal modes of the electroweak gauge bosons which acquire masses

$$M_W^2 = \frac{g^2 f_\pi^2}{4} \tag{5.3}$$

and

$$M_Z^2 = \frac{(g^2 + g'^2)f_\pi^2}{4} \tag{5.4}$$

with g and g' as the standard electroweak coupling constants. Taking the ratio between the Z and W masses

$$\frac{M_Z^2}{M_W^2} = \frac{(g^2 + g'^2)}{g^2} = \frac{1}{cos^2\theta_W} \tag{5.5}$$

we obtain the same relation as in the Standard Model formulation.

However, this isn't the end of the story. If you substitute the real-world values of the coupling constants g and g' into the expressions for the masses you obtain

$$M_W \approx 28 \text{ MeV} \tag{5.6}$$

and

$$M_Z \approx 32 \text{ MeV} \tag{5.7}$$

which are about 2800 times smaller than the real-world masses of the electroweak gauge bosons.

In addition to the problem of scale, this version of electroweak symmetry breaking through modified QCD dynamics does not give any clues about how to give mass to the fermions. In the following section we will discuss a set of theories, called technicolor, that attempt to deal with these issues while keeping the same essential structure of electroweak symmetry breaking through strong dynamics.

5.3 Technicolor

5.3.1 Minimal technicolor

As discussed in the previous section, a minimal technicolor theory that is just a scaled up version of QCD could explain electroweak symmetry breaking and give the appropriate masses for the W and Z bosons, but it would not explain the masses of the Standard Model fermions. However, it is still interesting to look at some of the consequences of such a theory.

Using simple scaling arguments we can derive expressions involving some general technicolor parameters [53].

$$F_T \sim v_0 \sqrt{\frac{1}{N_D}}; \quad \Lambda_T = \Lambda_{QCD} \frac{v_0\sqrt{3}}{f_\pi \sqrt{N_D N_T}}; \quad v_0 = 246 \text{ GeV} \tag{5.8}$$

Where F_T is analagous to f_π in QCD, N_D is the number of electroweak left handed doublets (with $2N_D$ right handed singlets) of techniquarks belonging to a gauge group $SU(N_{TC})$ (N_{TC} being the number of "colors" in the technicolor theory), and Λ_{TC} is the scale at which the technicolor interactions become strong. v_0 is the familiar electroweak vacuum expectation value.

In addition to the problem of fermion masses, minimal technicolor theories predict the existence of new massive particles (on the same order as the electroweak gauge bosons) and stable technibaryons, none of which have been seen experimentally. Precision measurements of electroweak parameters are also in conflict with predictions of these theories [54, 55].

5.3.2 Extended technicolor

Extended technicolor (ETC) was developed in order to account for the problems of minimal models discussed in the previous section. ETC posits the existence of a larger gauge group that contains the Standard Model, $SU(3)_c \otimes SU(2)_L \otimes U(1)_Y$, and technicolor, $SU(N_{TC})$, subgroups. Below some energy scale Λ_{ETC} only the technicolor and Standard Model gauge groups remain. Heavy ETC gauge bosons, corresponding to the broken generators of the ETC gauge group will mediate interactions among standard and technicolor fermions:

$$\bar{\alpha}_{ab} \frac{\bar{Q}\gamma_\mu \bar{T}^a Q \bar{Q}\gamma_\mu \bar{T}^b Q}{\Lambda_{ETC}^2} + \bar{\beta}_{ab} \frac{\bar{Q}\gamma_\mu \bar{T}^a \psi \bar{\psi}\gamma_\mu \bar{T}^b Q}{\Lambda_{ETC}^2} + \bar{\gamma}_{ab} \frac{\bar{\psi}\gamma_\mu \bar{T}^a \psi \bar{\psi}\gamma_\mu \bar{T}^b \psi}{\Lambda_{ETC}^2}. \tag{5.9}$$

The details of the α, β, and γ coefficents as well as the $\bar{T}$ operators depend on the specific ETC theory, but some general observations can be made. The α terms involve interactions among technifermions and can be manipulated such that the masses of pseudo-Goldstone bosons that arise will be high enough to not conflict with current experiment. The β terms, involving interactions between technifermions and Standard Model quarks and leptons, give rise to masses for the SM fermions. A natural scale for the quark and leptons masses can be derived:

$$m_{q,l} \sim \beta \frac{N_{TC}\lambda_{TC}^3}{\Lambda_{ETC}^2}. \tag{5.10}$$

In principle the observed hierarchy in fermion masses can be accounted for in the details of the ETC theory. Unfortunately, the γ terms cause a problem for realistic ETC models. These terms give rise to flavor changing neutral currents (FCNC) that would have an effect on quantities that have been well constrained by experiment. For instance, the experimental upper bound on the mass difference between K_L and K_S gives a lower bound on the ETC scale of $\Lambda_{ETC} \geq 10^3$ TeV. Using this lower bound and some reasonable estimates for the other parameters, we obtain an upper limit of ~ 100 MeV on the quark and lepton masses.

5.3.3 Walking technicolor

The problem of suppressing FCNC contributions while still accomodating the heavier quarks and leptons is at least partially addressed by a set of theories known as walking technicolor [56]. In standard ETC theories the technicolor coupling constant, α_{TC}, behaves like α_{QCD} in the Standard Model, i.e. it falls logarithmically above the energy scale Λ_{TC}. In contrast, the behaviour of α_{TC} in walking technicolor is such that in the range from Λ_{TC} to Λ_{ETC} its value is approximately constant. This requirement changes the expression given earlier for the quark and lepton masses to

$$m_{q,l} \sim \frac{\Lambda_{TC}^2}{\Lambda_{ETC}}. \tag{5.11}$$

This gives an approximate upper bound for quark and lepton masses of $\mathcal{O}(1\ \text{GeV})$. This is enough to account for all known leptons, and the first two generations of quarks. The bottom quark mass can possibly be accomodated (the estimates given are only at the order of magnitude level), but the top quark is certainly too heavy to be explained entirely by walking technicolor.

In order to account for the masses of the third generation of quarks a theory known as Topcolor Assisted Technicolor (TC2) has been developed [57, 58]. In this theory a small fraction of the mass of the top is provided by ETC and most of the mass is produced by topcolor dynamics at a scale of ~ 1 TeV.

5.3.4 Low-scale technicolor

It is interesting as an experimentalist to look at a particular type of walking technicolor theory known as low-scale technicolor (LSTC). It is possible to create a technicolor theory in which distinct sectors contribute to components of the full electroweak scale. In this case the lowest scale sector will produce phenomenology that is accesssible at LHC energies [59].

The phenomenology examined in this thesis is implemented in the so-called "LSTC straw man model" by the Pythia Monte Carlo generator [60]. This model reproduces the phenomenology of the lowest mass vector and pseudoscalar technihadrons in theories that have both a walking coupling constant, α_{TC} and topcolor interactions to produce the large mass of the top quark. Some important parameters of this model are N_{TC}, which determines the TC gauge group and is set to four, the charges Q_U and Q_D of the technifermions, which are defined such that $Q_U - Q_D = 1$, and the mixing angle, $sin\chi$, that links the lowest pseudoscalar bound states (these are the technipions but are not mass eigenstates) with the longitudinal weak bosons, $W_L^{\pm}$ and Z_L^0, and the mass eigenstates of the technipions

$$|\Pi_T\rangle = sin\chi\,|W_L\rangle + cos\chi\,|\pi_T\rangle\,; \quad sin\chi = F_T/F_\pi = 1/\sqrt{N_D}. \qquad (5.12)$$

F_T is the technipion decay constant and $F_\pi = 246$ GeV is the electroweak vacuum expectation value. The model used in the analysis presented in this thesis assumes $sin\chi = 0.333$ which fixes $F_T = 82$ GeV and $N_D = 9$.

Chapter 6

TECHNICOLOR SEARCHES IN PREVIOUS EXPERIMENTS

Early models of minimal technicolor and extended technicolor had fundamental problems arising from flavor changing neutral currents, the high mass of the top quark, and precision electroweak measurements [55, 54]. These problems are addressed by the addition of a walking coupling constant [56] and new interactions specific to the third generation of quarks (topcolor assisted technicolor). [57, 58] In order to investigate these theories experimentally a model describing the phenomenology accessible to recent accelerators (LEP, Tevatron, LHC), known as the Technicolor Straw Man model, was developed [61, 60].

It is difficult to directly compare LSTC results from different experiments because the phenomenology depends strongly on the parameters. The relationship of the technipion mass to the ρ_T/ω_T mass as well as the masses of the electroweak gauge bosons determines the relative strength of the different decay modes. In Figure 6.1 this problem is mitigated by showing the exclusion limits in the two dimensional space of $m[\rho_T/\omega_T]$ vs $m[\pi_T]$ [19]. The ATLAS results are based on ρ_T/ω_T decays to lepton pairs while the DØ results are from ρ_T/a_T to WZ and the CDF results are from ρ_T/a_T to Wπ_T where the technipion decays to two jets.

In Figure 6.2 an upper limit on cross-section times branching fraction as a function of the mass of the dilepton resonance is shown which ranges from 0.1 pb at a mass of 200 GeV down to 0.004 pb at 2 TeV, along with the LSTC theory predictions for a particular set of parameters that is excluded for masses less than 500 GeV.

By looking at a different decay mode that has not yet been examined at the LHC, the next chapter of this thesis attempts to provide a complementary analysis to those described here. Because the event kinematics and acceptance are not unique to LSTC, a model-independent upper limit on new high mass resonances decaying to $Z\gamma$ is also presented.
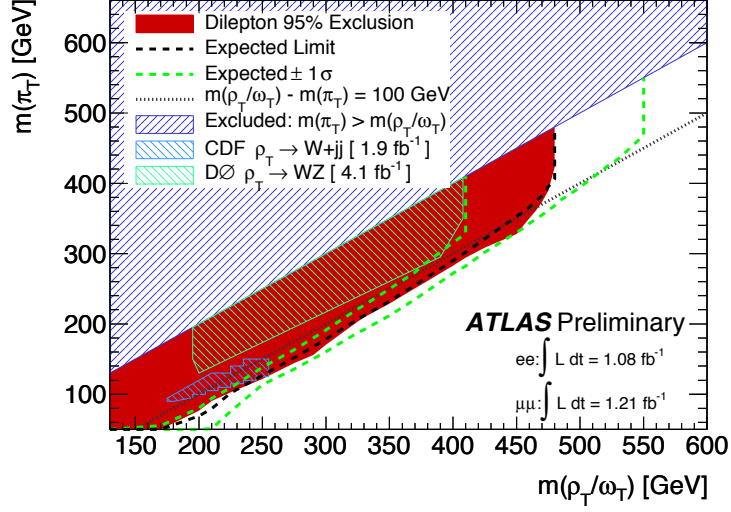
Figure 6.1: The 95% CL excluded region as a function of the assumed π_T and ρ_T/ω_T masses is shown in red. The dotted line corresponds to $m(\rho_T/\omega_T) - m(\pi_T) = 100$ GeV. The dashed line shows the expected limit with the green dashed lines showing the $\pm 1\sigma$ bands. The hashed region where $m(\pi_T) > m(\rho_T/\omega_T)$ is excluded by theory. Also shown are recent results from CDF [17] and DØ [18]. Figure from [19].
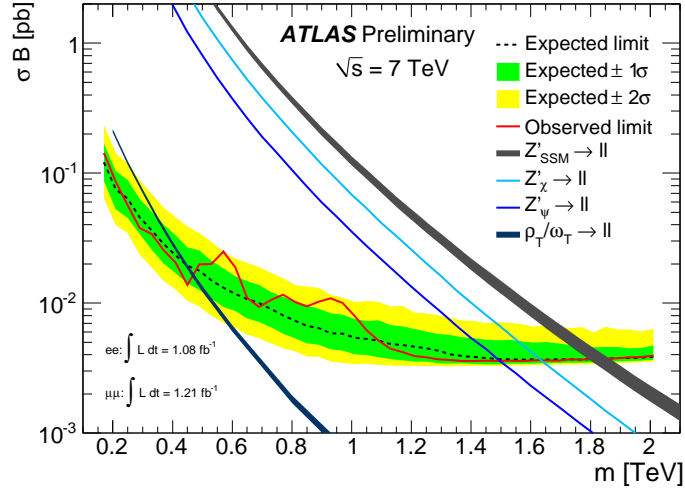
Figure 6.2: The expected and observed 95% CL limits on σB as a function of mass of ρ_T/ω_T for the combination of the dielectron and dimuon channels. Also shown are the theory predictions for the LSTC model, assuming $m(\rho_T/\omega_T) - m(\pi_T) = 100$ GeV [19].

Chapter 7

THE SEARCH FOR LOW-SCALE TECHNICOLOR IN ATLAS

7.1 Introduction

While the early, minimal technicolor models developed in the 1970s by Susskind and Weinberg have been ruled out by experiments, more recent technicolor theories are still consistent with current precision electroweak measurements. For this analysis the low scale technicolor (LSTC) model described in the previous chapter will be investigated. This model is especially interesting for ATLAS because it predicts the existence of technihadrons that can decay to Standard Model particles which will leave distinctive signals in the detector.

The analysis presented here is focused on the $Z+\gamma$ final state. There are two technicolor particles that can decay to $Z\gamma$, ρ_T and ω_T. The two resonances are nearly degenerate with ω_T making the dominant contribution.
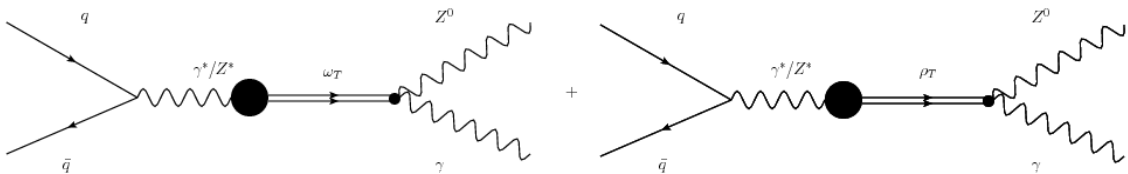
Figure 7.1: Feynamn diagrams for the technicolor to $Z\gamma$ processes.

7.2 Monte Carlo generation

Pythia was used to generate the Monte Carlo signal samples using the technicolor strawman framework. The parameters used for the generation of the LSTC signal Monte Carlo samples

are as follows:

- The number of techniquark doublets is set to $N_D = 9$. This leads to $F_T \approx 82$ GeV.

- The difference between the techniquark charges is taken to be $Q_U - Q_D = 1$.

- The mixing angle between the techniquarks is taken to be $\sin \chi = 0.333$.

- The ratio of technipion couplings is taken to be $\frac{g_{a_T \pi_T \pi_T}}{g_{\omega_T \pi_T \pi_T}} = 1$.

- The gauge group used is $SU(4)$.

The events were generated with generator filters for photons and leptons:

- The events must contain one lepton with $p_T(l) > 15$ GeV and $|\eta_e| < 3$.

- The events must contain one photon with $p_T(\gamma) > 15$ GeV and $|\eta_\gamma| < 3$.

A range of ρ_T/ω_T masses were generated running from $200 - 500$ GeV.

π_T Mass (GeV)	ρ_T Mass (GeV)	a_T Mass (GeV)	$\sigma \times$ BR (fb) $(Z\gamma)$	filter efficiency $(Z\gamma)$
105	200	225	23.8	0.83
170	300	330	5.0	0.90
240	400	440	1.8	0.93
300	500	550	0.8	0.95

Table 7.1: Parameters, cross sections and filter efficiencies for the signal points considered in this analysis.

An alternative set of parameters were also considered. These were chosen to be comparable to other technicolor searches in ATLAS, specifically in the WZ channel.

π_T Mass (GeV)	ρ_T Mass (GeV)	a_T Mass (GeV)	$\sigma \times$ BR (fb) $(Z\gamma)$	filter efficiency $(Z\gamma)$
120	200	225	61.2	0.83
220	300	330	15.4	0.90
320	400	440	5.6	0.93
420	500	550	2.2	0.95

Table 7.2: Alternative set of parameters used in the other ATLAS TC searches. In this case the mass of the $M(\pi_T) = M(\rho_T) - M(W)$.
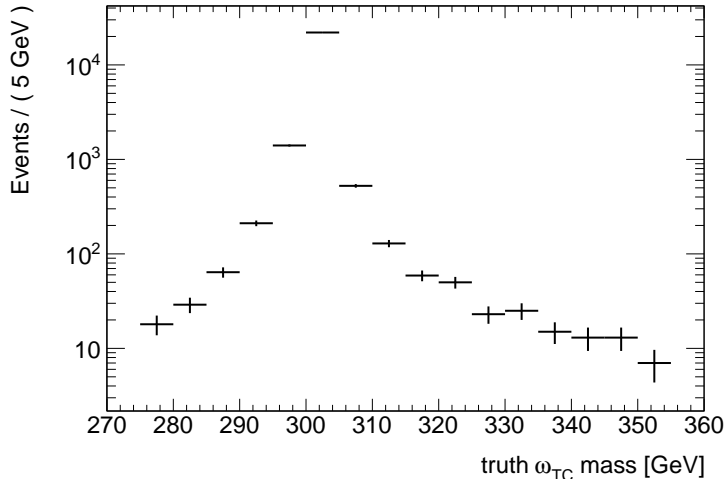
Figure 7.2: Invariant mass distribution of the $Z\gamma$ system at the truth level for the case where $M(\rho_T) = 300$ GeV.

Figure 7.2 shows the invariant mass distribution of the $Z\gamma$ system at the generator level for the sample where $M(\rho_T) = 300$ GeV. The width of the resonance is of order 1 GeV or less.

7.3 Event selection

Because the LSTC signal is a narrow high mass resonance, the transverse momentum of the photon is expected to be higher in the signal than in the background. In addition to the selection requirements used in the Standard Model cross-section measurement seen in section 4.1 the transverse momentum of the photon is required to be greater than 40 GeV.

The discriminating variable used to distinguish signal from background is the invariant mass of the $Z\gamma$ system.

7.4 Background determination

There are two primary backgrounds for the LSTC $Z\gamma$ signal. The largest is Standard Model continuum $Z\gamma$ production with a smaller contribution from $Z + jets$. The SM $Z\gamma$ is estimated from Monte Carlo simulations while the $Z + jets$ is estimated using the same data driven method described in the Standard Model cross-section analysis.

In order to compare the expected background to the data, two control regions are chosen:

- $M(Z\gamma) < 170$ GeV

- $15 < p_T^\gamma < 40$ GeV.

(a) $p_T(\mu)$

(b) $p_T(\gamma)$

(c) $M(Z\gamma)$
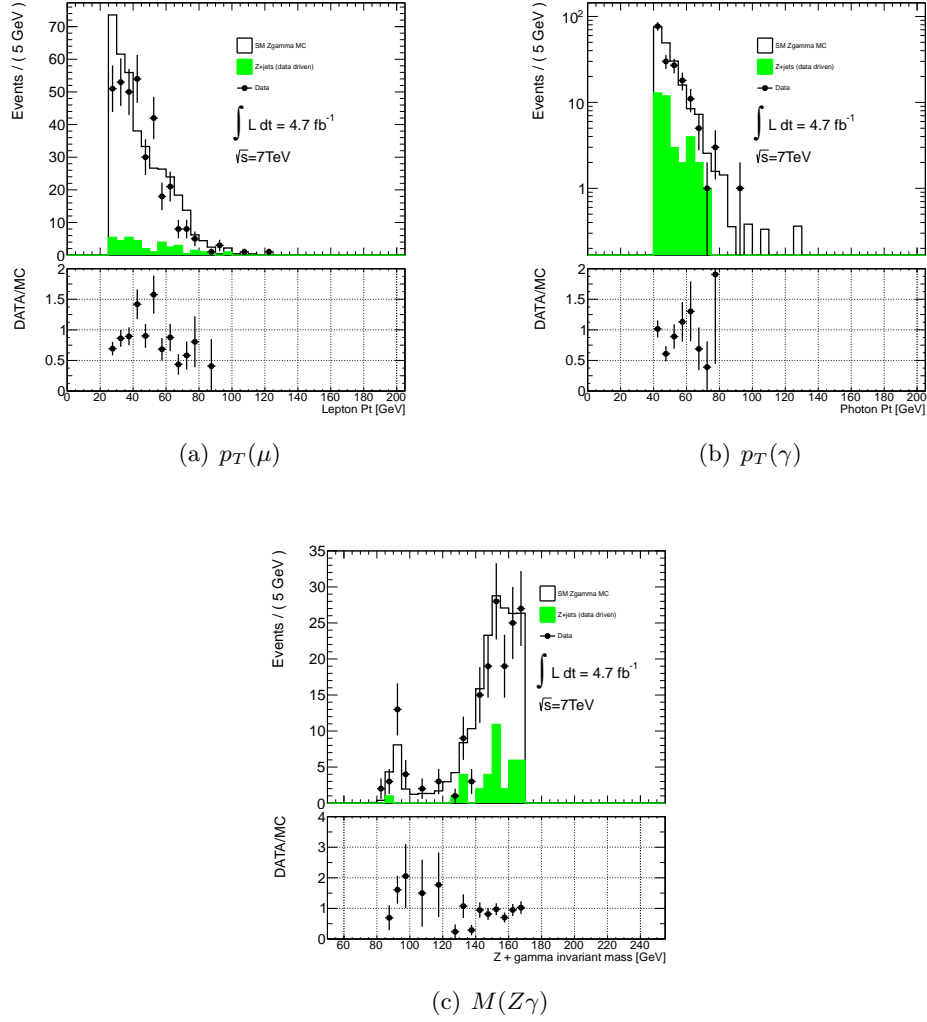
Figure 7.3: Kinematic distributions for the muon channel in the low mass control region.

It is expected that the control regions will be dominated entirely by the background processes, so ideally the expected background from Monte Carlo and data driven estimations match the data within reasonable bounds. Because of the limited statistics it is not possible to get exact agreement and the results shown allow for confidence that the background distributions are well understood.

(a) $p_T(e)$

(b) $p_T(\gamma)$

(c) $M(Z\gamma)$
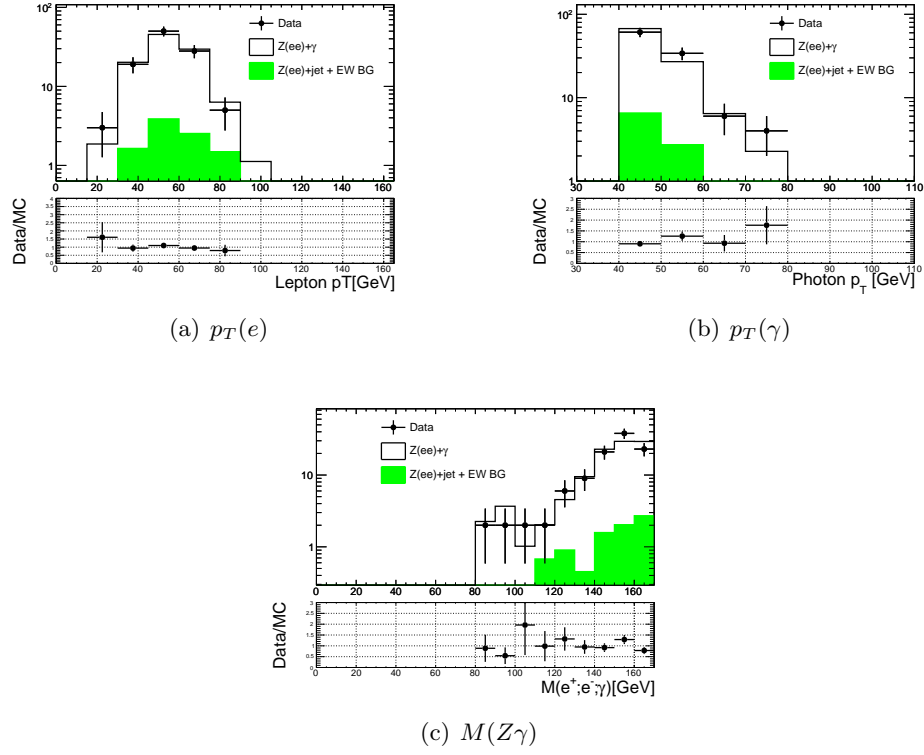
Figure 7.4: Kinematic distributions for the electron channel in the low mass control region.

7.5 Signal fitting

The signal fit is performed using a function that is the sum of a Gaussian and a Crystal Ball:

$$pdf_{\text{sig}} = (\beta) \times f_{CB}(m, \mu_{CB}, \sigma_{CB}, \alpha_{CB}, n_{CB}) + (1 - \beta) \times f_{Gaus}(m, \mu_G, \sigma_G) \tag{7.1}$$

Unbinned χ^2 fits are made using Roofit. A fit range of $\pm 4\sigma$ around the nominal signal mass is used, where σ is determined from a preliminary fit with a fixed range of ± 40 GeV. The means of the Crystal Ball and the Gaussian were constrained to be identical, and the width of the Gaussian and the n parameter of the Crystal Ball were both fixed after studies showed that allowing them to float did not strongly affect the quality of the fit.

Table 7.3 gives the fit parameters for all the signal masses considered as well as the acceptance. The acceptance is defined as the ratio of the number of reconstructed events that passed all selection cuts to the number of generated events in the extended fiducial region.

(a) $p_T(\mu)$

(b) $p_T(\gamma)$

(c) $M(Z\gamma)$
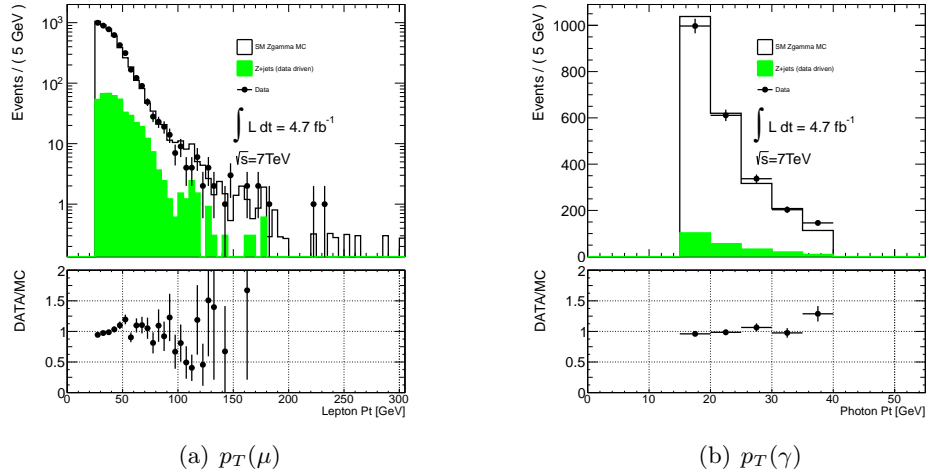
Figure 7.5: Kinematic distributions for the muon channel in the low $p_T(\gamma)$ control region.

7.6 Background fitting

The choice of 40 GeV as the cut on photon transverse momentum means that there is a kinematic turn on in the $Z\gamma$ invariant mass distribution between 140 and 170 GeV. Since the lowest signal mass that will be investigated is at 200 GeV the background will only be fit above 180 GeV. The background is fit using the sum of two exponentials:

$$pdf_{bkg} = e^{\alpha_1 m} + e^{\alpha_2 m} \tag{7.2}$$
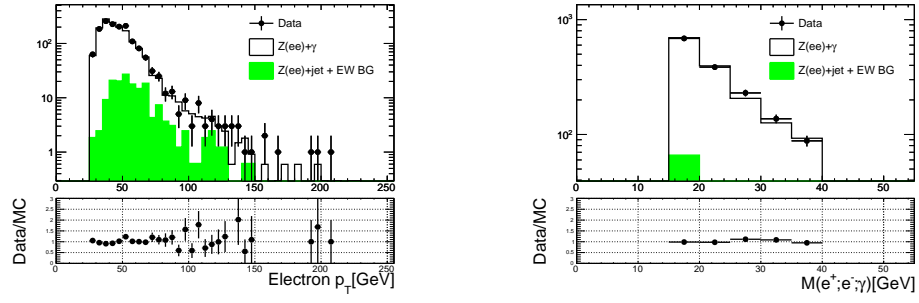
(a) $p_T(e)$

(b) $p_T(\gamma)$
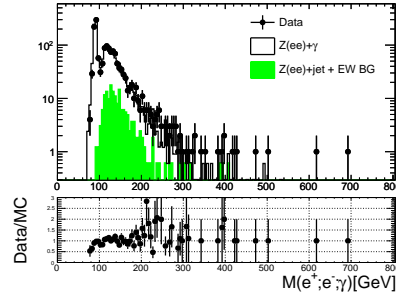
(c) $M(Z\gamma)$
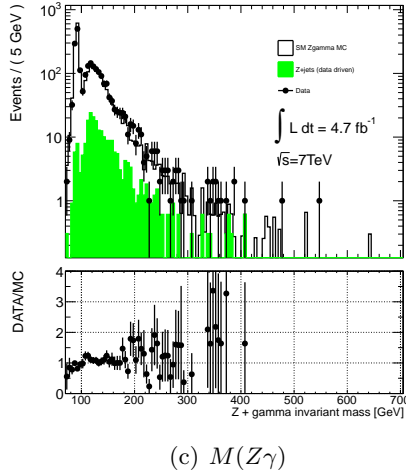
Figure 7.6: Kinematic distributions for the electron channel in the low $p_T(\gamma)$ control region.
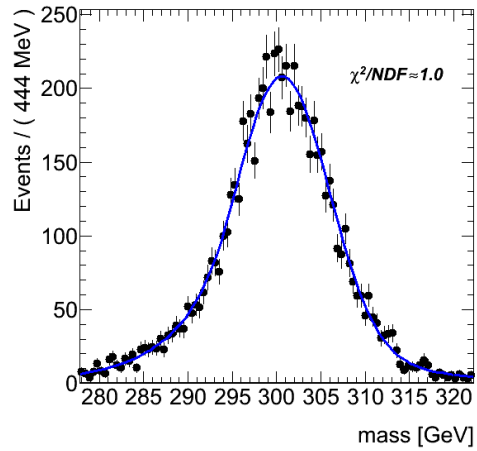
Figure 7.7: Monte Carlo signal mass distribution and fit for $M\rho_T = 300$ GeV.

Parameter	200 GeV	300 GeV	400 GeV	500 GeV
$\mu_{CB} = \mu_G$ [MeV]	200301 ± 62	300587 ± 103	400678 ± 131	500492 ± 181
σ_{CB} [MeV]	2807 ± 269	9551 ± 689	15110 ± 1445	19735 ± 1556
α_{CB}	1.034 ± 0.109	1.289 ± 0.119	1.369 ± 0.096	1.637 ± 0.251
n_{CB}	25	25	25	25
β	0.603 ± 0.108	0.712 ± 0.059	0.777 ± 0.056	0.682 ± 0.058
σ_G [MeV]	4657 ± 216	4905 ± 214	7379 ± 268	9173 ± 385
acceptance	0.610 ± 0.009	0.623 ± 0.008	0.630 ± 0.009	0.627 ± 0.008

Table 7.3: Fit parameters found for all the nominal signal TC samples in the muon channel.

Parameter	200 GeV	300 GeV	400 GeV	500 GeV
$\mu_{CB} = \mu_G$ [MeV]	199671 ± 107	299457 ± 108	399889 ± 103	499921 ± 109
σ_{CB} [MeV]	2971 ± 122	4774 ± 167	5546 ± 156	7070 ± 153
α_{CB}	0.898 ± 0.078	1.263 ± 0.089	1.329 ± 0.079	1.538 ± 0.094
n_{CB}	25	25	25	25
β	0.800 ± 0.043	0.874 ± 0.037	0.833 ± 0.035	0.877 ± 0.028
σ_G [MeV]	5075 ± 398	11552 ± 1502	13063 ± 1103	18120 ± 2043
acceptance	0.427 ± 0.008	0.457 ± 0.007	0.466 ± 0.007	0.483 ± 0.007

Table 7.4: Fit parameters found for all the nominal signal TC samples in the electron channel.

7.6.1 Systematic uncertainty

Systematic uncertainties on the signal samples were determined on the following:

- The lepton energy scale and resolution.

- The lepton identification efficiency.

- The photon energy scale and identification efficiency.

- The luminosity.

case	α_1	α_2	number of SM bkg
nominal μ	$(-1.8 \pm 0.08) \times 10^{-5}$	$(-7.9 \pm 0.68) \times 10^{-6}$	267 ± 7
nominal e	$(-1.7 \pm 0.10) \times 10^{-5}$	$(-8.4 \pm 0.81) \times 10^{-6}$	201 ± 8

Table 7.5: Fit parameters for the nominal Standard Model background fit.

(a) Fit   (b) Residual
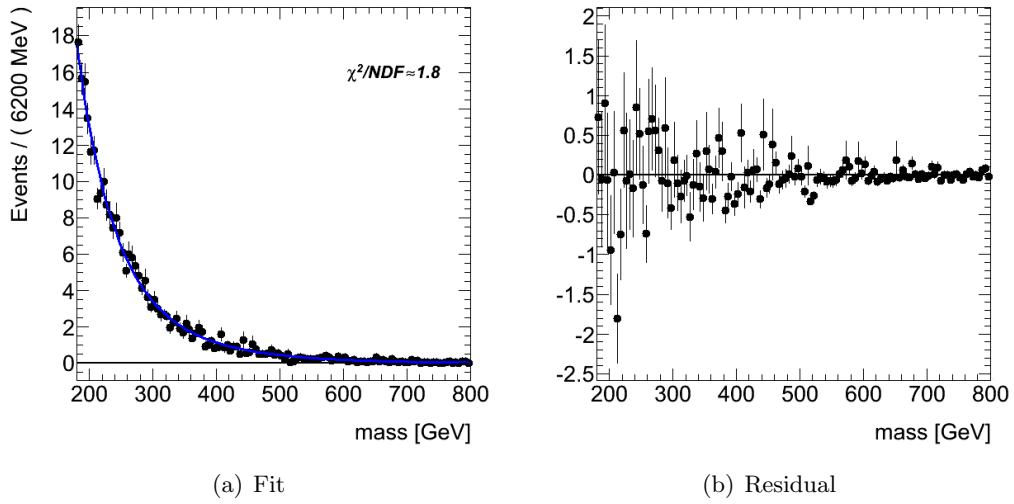
Figure 7.8: SM background for the muon channel.

(a) Fit   (b) Residual
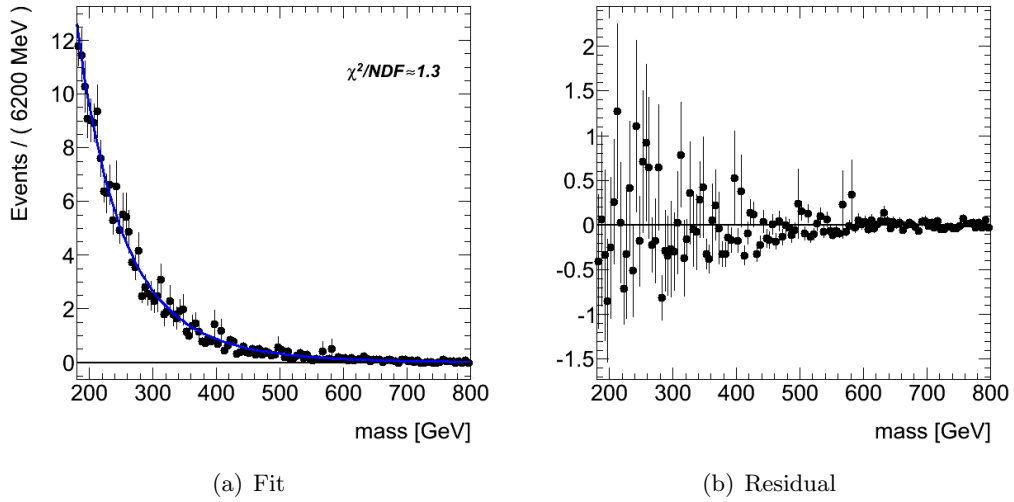
Figure 7.9: SM background for the electron channel.

For the background, they are not considered since they are either negligible or already accounted for in the degrees of freedom of the background *pdf*. The effects of the systematic uncertainties are calculated for both the signal rate and the position of the signal peak.

The contributions from the different systematics are summarized in tables 7.6 and 7.7. The effects of the energy scale uncertainties were determined by applying a shift (either

systematic	Event Up (%)	Event Down (%)	Peak Up MeV	Peak Down MeV
Lepton Energy Scale	0.0	0.01	2	0
Lepton Identification	0.25	0.25	0	0
Lepton Isolation	0.07	0.15	1	3
Photon Energy Scale	0.0	0.01	15	16
Photon Identification	5	5	0	0
Photon Isolation	0.19	0.24	3	4
Luminosity	1.8	1.8	0	0

Table 7.6: Systematic uncertainties for $M(\rho_\mathsf{T}) = 300$ GeV, for the muon channel.

systematic	Event Up (%)	Event Down (%)	Peak Up MeV	Peak Down MeV
Lepton Energy Scale	1.9	1.82	34	30
Lepton Identification	0.0	0.04	0	0
Lepton Isolation	0.44	0.38	5	8
Photon Energy Scale	0.06	0.0	31	17
Photon Identification	5	5	0	0
Photon Isolation	0.53	0.74	0	6
Luminosity	1.8	1.8	0	0

Table 7.7: Systematic uncertainties for the point where $M(\rho_\mathsf{T}) = 300$ GeV, for the electron channel.

up or down) to the lepton and photon transverse energies corresponding to a one sigma deviation from the central value and seeing the effect on the event yield and peak position in the signal Monte Carlo. The shifts depend on the kinematics of the event and are calculated using software tools supplied by the ATLAS e/γ performance and muon combined performance groups. The effect of isolation uncertainty was estimated in a similar fashion by applying a shift to the isolation energy or momentum (EtCone30 for photons and electrons, Ptcone30 for muons), but the shift was a constant 500 MeV (both up and down). The photon identification uncertainty was conservatively estimated at 5% based on studies of the ATLAS e/γ performance group [48].

7.7 Determination of upper limits

Two different methods will be used to extract upper limits on the $\rho_T/\omega_T \rightarrow Z\gamma$ cross section.

7.7.1 Feldman-Cousins method

The first method presented is a simple counting experiment. An upper limit on the number of signal events produced can be calculated using the prescription given by Feldman and Cousins [62] given the number of expected background events and the number of events observed in data. The ratio of that upper limit to the number of signal events predicted by Monte Carlo produces a quick and dirty estimate of the upper limit on the $\rho_T/\omega_T \to Z\gamma$ cross section times branching fraction.
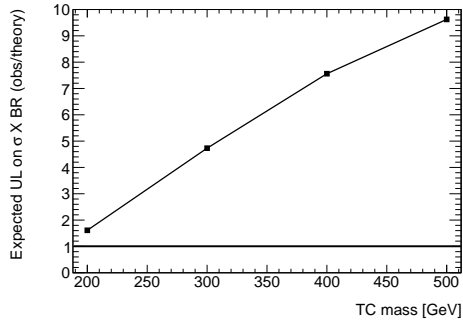
Figure 7.10: Expected upper limit at the 95% CL using the Feldman-Cousins method.

7.7.2 CL_s method

The Feldman-Cousins method described above is relatively crude and is intended mostly as a cross check on the more complex and sophisticated CL_s [63] method. The CL_s method is the standard recommended by the ATLAS collaboration. The method and the software used to calculate the CL_s upper limits were adapted from those used in the ATLAS $H \to \gamma\gamma$ analysis [64].

First, a "discovery" hypothesis test is performed to evaluate the compatibility between data and the null hypothesis, which assumes the existence of only Standard Model background processes. If the hypothesis test shows no significant excess in data, a limit on the $Z\gamma$ resonance production cross section will be set.

The compatibility between data and the null hypothesis is indicated by the p-value of a null hypothesis p_0. When an excess over the background is present in data, p_0 will be close to 0, indicating a significant discrepancy between data and the null hypothesis.

In the case of setting an exclusion limit, the hypothesis in question is a signal plus background hypothesis. It is tested against the background only hypothesis. As one is interested

to know for which level of signal the signal plus background hypothesis is excluded, various hypotheses on the strength of the signal are tested.

In the CL_s method, the confidence level is modified to take into account downward background fluctuations, and the modified p-value is quoted as CL_s. When CL_s is less than 0.05, the hypothesis in question is claimed to be excluded at the 95% CL.

In the following subsections, the details of the above procedure will be presented.

Test statistic

The test statistic used in this analysis is the profile likelihood ratio, which is the ratio of two maximized likelihood functions built from the signal plus background model.

The method used to extract the signal uses an unbinned maximum likelihood (ML) fitting technique. The likelihood is defined as

$$\mathcal{L}(\sigma_{Fid}, \boldsymbol{\theta}) = e^{-(N_S(\sigma_{Fid})+N_B)} \prod_{k=1}^{n} N_S(\sigma_{Fid}) f_S(\mathbf{x}_k; m_{TC}, \boldsymbol{\theta}_S) + N_B f_B(\mathbf{x}_k; \boldsymbol{\theta}_B) \qquad (7.3)$$

In the equation above, n is the number of entries in the fitted dataset $\mathbf{x}$ and each $\mathbf{x}_k$ represents one entry. In our case, each entry contains the value of $M_{Z\gamma}$ for the event considered. The quantities f_S and f_B are the probability density functions (*pdf*) for the signal and background component respectively. The number of background events is denoted N_B, and the number of signal events is expressed as $N_S(\sigma_{Fid})$, with σ_{Fid}, the fiducial cross section, being the parameter of interest.

The remaining ("nuisance") parameters in the signal and background *pdf* are denoted by the vectors $\boldsymbol{\theta}_S$ and $\boldsymbol{\theta}_B$ respectively.

In what follows the combined vector $\boldsymbol{\theta} = \boldsymbol{\theta}_S \cup \boldsymbol{\theta}_B$ will be used. The parameter m_{TC}, the ρ_T mass in the TC sample considered, is always fixed in the fits and therefore not included in the nuisance parameters. The floating parameters in the fit are σ_{Fid}, N_B and $\boldsymbol{\theta}$.

The test statistic for a discovery is defined as:

$$t_0 = -2ln\left(\frac{\mathcal{L}(\sigma_{Fid}, \hat{\boldsymbol{\theta}})}{\mathcal{L}(\sigma_{Fid} = 0, \hat{\hat{\boldsymbol{\theta}}})}\right) \qquad (7.4)$$

The test statistic for exclusion is defined as:

$$\tilde{q}_{\sigma_{Fid}} = \begin{cases} -2\,ln\frac{\mathcal{L}(\sigma_{Fid}; \hat{\hat{\boldsymbol{\theta}}})}{\mathcal{L}(0, \hat{\boldsymbol{\theta}})} & \hat{\sigma}_{Fid} < 0, \\ -2\,ln\frac{\mathcal{L}(\sigma_{Fid}, \hat{\hat{\boldsymbol{\theta}}})}{\mathcal{L}(\hat{\sigma}_{Fid}, \hat{\boldsymbol{\theta}})} & 0 \leq \hat{\sigma}_{Fid} \leq \sigma_{Fid}, \\ 0 & \hat{\sigma}_{Fid} > \sigma_{Fid} \end{cases} \qquad (7.5)$$

where σ_{Fid}, the fiducial signal cross section, is the strength parameter, $\hat{\sigma}_{Fid}$ is the fit favored σ_{Fid} value, $\hat{\boldsymbol{\theta}}$ is the collective denotation of the fit favored nuisance parameters values when

σ_{Fid} is constant in the fit, $\hat{\theta}$ is the collective denotation of the fit favored nuisance parameters values when σ_{Fid} is also free in the fit.

Generation of pseudo-data

Pseudo datasets are generated under a *pdf* corresponding to a certain hypothesis. To find the expected confidence level and extract a CL_s limit, requires the generation of background-only pseudo datasets.

When a pseudo dataset is generated, all parameters in the *pdf* are fixed to their nominal values. The expected numbers of events is given by a random number from a Poisson distribution around the central values $N_S(\sigma_{Fid})$ and N_B^{exp}.

The treatment of nuisance parameters used for systematic uncertainties follows the "unconditional ensemble" prescription: for each pseudo dataset the central values of the constraints are drawn from their *pdf*, and these values are used in the calculations of $\mathcal{L}$ and $\tilde{q}_{\sigma_{Fid}}$.

Determination of p-value

After fitting a dataset (either real data or pseudo-data), values of $\tilde{q}_{\sigma_{Fid}}$ are computed for various values of σ_{Fid} where pseudo datasets are generated, denoted as σ'_{Fid}. For a given σ'_{Fid} at a chosen LSTC mass m_{TC}, calculating $\tilde{q}_{\sigma_{Fid}}$ for each pseudo dataset generated under signal plus background hypothesis leads to a distribution of $\tilde{q}_{\sigma_{Fid}}$, $f(\tilde{q}_{\sigma_{Fid}}|\sigma_{Fid} = \sigma'_{Fid})$. A p-value for the dataset tested is defined as

$$p_{\sigma'_{Fid}} = \int_{\tilde{q}_{\sigma'_{Fid},obs}}^{\infty} f(\tilde{q}_{\sigma_{Fid}}|\sigma_{Fid} = \sigma'_{Fid}) \, dq_{\sigma_{Fid}} \tag{7.6}$$

where $\tilde{q}_{\sigma'_{Fid},obs}$ is the test statistic value calculated from the dataset tested. Such a p-value is also quoted as p_{s+b}.

Definition of exclusion limit

The CL_s method is used to compute the confidence level (CL). The CL_s limit claims exclusion at the 95% CL when $CL_s = 0.05$. The CL_s is defined as:

$$CL_s = \frac{p_{s+b}}{1 - p_0} \tag{7.7}$$

where p$_0$ is the integrated value of the background-only distribution from 0 to q$_{\sigma_{Fid}}^{obs}$. 1-p$_0$ is also referred as the confidence level of background-only hypothesis (CL_b).

Interpolation of Limit

When the limit setting CL_s is decided, to find its 95% exclusion limit, an iteration over values of σ_{Fid} is performed. This is usually done by scanning a predefined set of values to identify a small interval $[\sigma_{Fid}^{low}, \sigma_{Fid}^{high}]$ containing σ_{Fid}^{up} which satisfies the requirement stated in Section 7.7.2, and estimating the crossing point using a linear interpolation.

Here one uses σ_{Fid} values ranging from 0 to 100 fb, in step of 0.1 fb for the $Z\gamma$ search.
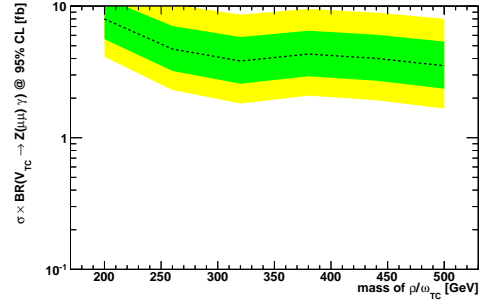
7.7.3 Expected limits

The expected limits for the $Z\gamma$ channel are given in Figure 7.11. In the model suggested by K. Lane ω_T masses up to ~ 330 GeV could be excluded. With the parameters from the other ATLAS TC searches, one can expect to exclude the production of ω_T and ρ_T in the $Z\gamma$ final states in almost the entire mass range considered (up to ~ 500 GeV). While the analysis described here uses fit parameters extracted from LSTC signal Monte Carlo, the upper limit on cross section times branching ratio is also applicable to any similarly narrow resonance.

7.7.4 Observed limits
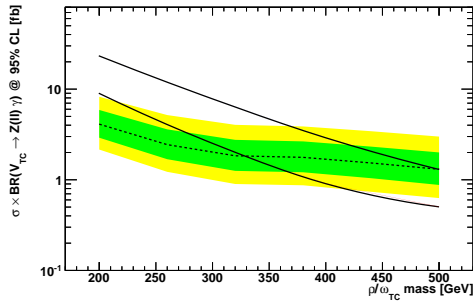
The observed limit on cross section times branching fraction of $\rho_T/\omega_T \to Z\gamma$ where the Z decays to electrons or muons is shown on Figure 7.12. The model based on K. Lane's parameters is excluded for masses from 200 to 280 GeV and the model used in other ATLAS technicolor searches is excluded for masses from 200 to 480 GeV.
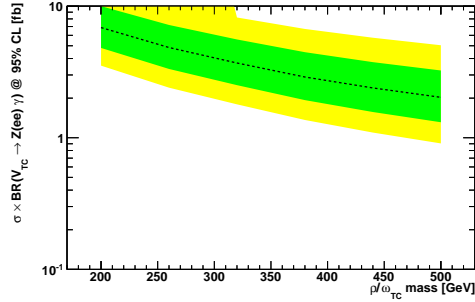
(a) Limit from electron channel only.

(b) Limit from muon channel only.

(c) Limit from the combined electron and muon channels.

Figure 7.11: Expected limits on the cross section times branching ratio for new resonances decaying to $Z\gamma$ where the Z decays to leptons. The line in black is the expected limit, the yellow and green band are the 1 and 2σ errors. The two other lines are the theoretical cross sections for the ATLAS compatible search (blue) and for the parameters suggested by K. Lane (red).

Figure 7.12: Measured limits for the $Z\gamma$ channel. The solid black line is the expected limit, the yellow and green band are the 1 and 2σ errors. The dashed line is the observed limit with the full 2011 7 TeV dataset. The two other lines are the theoretical cross sections for the ATLAS compatible search (blue) and for the parameters suggested by K. Lane (red).
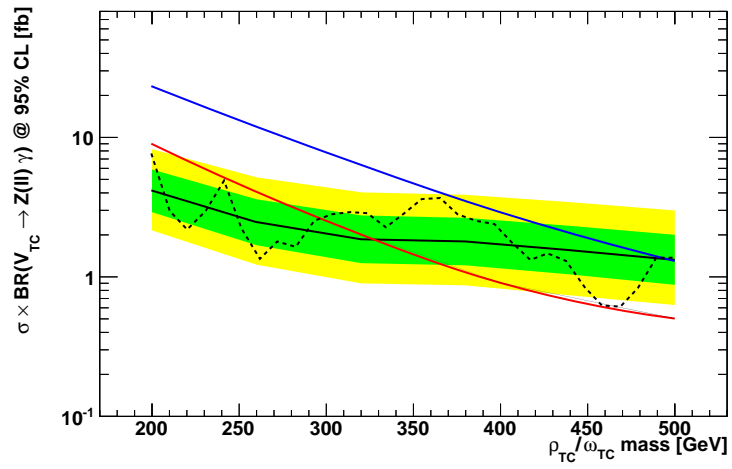
Chapter 8

CONCLUSIONS

This thesis has examined the problem of electroweak symmetry breaking both in the Standard Model and in technicolor theories. The cross-section times branching fraction for the production of $Z\gamma$ final states in the SM was measured, and limits on the production of new technicolor particles were calculated using $4.7fb^{-1}$ of 7 TeV data from the ATLAS experiment.

The Standard Model cross section times branching fraction was measured to be $1.26 \pm 0.07(stat.) \pm 0.07(syst.)$ pb when the Z boson decays to electrons and $1.24 \pm 0.07(stat.) \pm 0.11(syst.)$ pb when it decays to muons. These are in good agreement with the Standard Model prediction of $1.22 \pm 0.05(syst.)$ pb for each channel.

The production of ρ_{T} and ω_{T} decaying to $Z\gamma$ is excluded for masses from 200 to 280 GeV in the model suggested by K. Lane from 200 to 480 GeV in the model used by other ATLAS technicolor searches. In addition to the limits on the specific models presented here, the analysis also puts an upper limit on the cross section times branching fraction of any similarly narrow resonance decaying to $Z\gamma$ for masses between 200 and 500 GeV.

In addition to the analyses described here, I was also involved in other work for the ATLAS collaboration. In 2006 and 2007 I helped with the testing and installation of the optical links for the ATLAS pixel detector. In 2010 I was the Deputy Run Coordinator for the ATLAS Beam Conditions Monitor and wrote software for the BCM detector control system.

Bibliography

[1] File:Standard_Model_of_Elementary_Particles.svg, 2006. Used under the Creative Commons Attribution 3.0 Unported license. http://creativecommons.org/licenses/by/3.0/.

[2] The ATLAS experiment at the CERN large hadron collider. *Journal of Instrumentation*, 3(08):S08003, 2008.

[3] Peter Jenni et al. ATLAS high-level trigger, data-acquisition and controls. Technical Report ATLAS-TDR-016, CERN, Geneva, 2003.

[4] A. Djouadi, J. Kalinowski, and M. Spira. HDECAY: A Program for Higgs boson decays in the standard model and its supersymmetric extension. *Comput.Phys.Commun.*, 108:56–74, 1998.

[5] G Aad et al. ATLAS pixel detector electronics and sensors. *Journal of Instrumentation*, 3(07):P07007, 2008.

[6] Alignment of the ATLAS Inner Detector Tracking System with 2010 LHC proton-proton collisions at $sqrts = 7$ TeV. Technical Report ATLAS-CONF-2011-012, CERN, Geneva, Mar 2011.

[7] ATLAS pixel public results TWiki. accessed June 2012.

[8] ATLAS SCT public results TWiki. accessed June 2012.

[9] ATLAS TRT public results TWiki. accessed June 2012.

[10] M. Aharrouche et al. Energy linearity and resolution of the ATLAS electromagnetic barrel calorimeter in an electron test-beam. *Nuclear Instruments and Methods in Physics Research Section A: Accelerators, Spectrometers, Detectors and Associated Equipment*, 568(2):601 – 623, 2006.

[11] P. Adragna et al. Testbeam studies of production modules of the ATLAS Tile Calorimeter. *Nuclear Instruments and Methods in Physics Research Section A: Accelerators, Spectrometers, Detectors and Associated Equipment*, 606(3):362 – 394, 2009.

[12] ATLAS muon system public results TWiki. accessed June 2012, ATLAS-PLOT-MUON-2011-006, ATLAS-PLOT-MUON-2012-001.

[13] BCM and BLM performance plots. Technical Report ATLAS-PLOT-INDET-2010-003, CERN, Oct 2010.

[14] ATLAS combined summary plots TWiki. accessed July 2012.

[15] Efficiencies of electron/photon triggers using early 2011 data: Approval for PLHC2011. Technical Report ATL-COM-DAQ-2011-032, CERN, Geneva, May 2011.

[16] Performance of the ATLAS muon trigger in 2011. Technical Report ATL-DAQ-PROC-2012-008, CERN, Geneva, Jun 2012.

[17] T. Aaltonen et al. Search for technicolor particles produced in association with a W boson at CDF. *Phys. Rev. Lett.*, 104:111802, Mar 2010.

[18] V. M. Abazov et al. Search for a resonance decaying into WZ boson pairs in $p\bar{p}$ collisions. *Phys. Rev. Lett.*, 104:061801, Feb 2010.

[19] ATLAS collaboration. Search for technihadrons in pp collisions at sqrts=7 TeV with the ATLAS detector. Technical Report ATLAS-CONF-2011-125, CERN, Geneva, Sep 2011.

[20] ALEPH Collaboration, DELPHI Collaboration, L3 Collaboration, OPAL Collaboration, and The LEP Working Group for Higgs Boson Searches. Search for the standard model Higgs boson at LEP. *Physics Letters B*, 565(0):61 – 75, 2003.

[21] TEVNPH Working Group. Combined CDF and D0 search for standard model Higgs boson production with up to $10.0 fb^{-1}$ of data, 2012.

[22] Combined search for the standard model Higgs boson using up to 4.9 fb^{-1} of pp collision data at with the ATLAS detector at the LHC. *Physics Letters B*, 710(1):49 – 66, 2012.

[23] CMS Collaboration. Combined results of searches for the standard model Higgs boson in pp collisions at $\sqrt{s} = 7$ TeV. *Physics Letters B*, 710(1):26 – 48, 2012.

[24] Observation of an excess of events in the search for the Standard Model Higgs boson with the ATLAS detector at the LHC. Technical Report ATLAS-CONF-2012-093, CERN, Geneva, Jul 2012.

[25] Observation of a new boson with a mass near 125 GeV. Technical Report CMS-PAS-HIG-12-020, CERN, Geneva, July 2012.

[26] Leonard Susskind. Dynamics of spontaneous symmetry breaking in the Weinberg-Salam theory. *Phys. Rev. D*, 20:2619–2625, Nov 1979.

[27] Stephen P. Martin. A supersymmetry primer, 1997.

[28] S. Dimopoulos and S. Raby. Supercolor. *Nuclear Physics B*, 192(2):353 – 368, 1981.

[29] Estia Eichten and Kenneth Lane. Dynamical breaking of weak interaction symmetries. *Physics Letters B*, 90(1-2):125 – 130, 1980.

[30] Estia Eichten and Kenneth Lane. Low-scale technicolor at the Tevatron and LHC. *Physics Letters B*, 669(3-4):235 – 238, 2008.

[31] Dan Green. *At the Leading Edge: The ATLAS and CMS LHC Experiments.* World Scientific Publishing Company, feb 2010.

[32] K. Reeves. ATLAS SemiConductor Tracker and Pixel Detector: Status and Performance. Presented at ICHEP 2012, 2012.

[33] K.K. Gan, W. Fernando, P.D. Jackson, M. Johnson, H. Kagan, A. Rahimi, R. Kass, S. Smith, P. Buchholz, M. Holder, A. Roggenbuck, P. Schade, and M. Ziolkwoski. Optical link of the ATLAS pixel detector. *Nuclear Instruments and Methods in Physics Research Section A: Accelerators, Spectrometers, Detectors and Associated Equipment*, 570(2):292 – 294, 2007.

[34] E Abat et al. The ATLAS TRT barrel detector. *Journal of Instrumentation*, 3(02):P02014, 2008.

[35] M. Markus. Inner Detector status. Presented during ATLAS week June 2012, 2012.

[36] C. Adorisio et al. System test of the ATLAS muon spectrometer in the H8 beam at the CERN SPS. *Nuclear Instruments and Methods in Physics Research Section A: Accelerators, Spectrometers, Detectors and Associated Equipment*, 593(3):232 – 254, 2008.

[37] Luminosity determination in pp collisions at sqrt(s) = 7 TeV using the ATLAS detector in 2011. Technical Report ATLAS-CONF-2011-116, CERN, Geneva, Aug 2011.

[38] V Cindro et al. The ATLAS Beam Conditions Monitor. *Journal of Instrumentation*, 3(02):P02004, 2008.

[39] Luminosity determination in pp collisions at $\sqrt{s} = 7$ TeV using the ATLAS detector at the LHC. *The European Physical Journal C - Particles and Fields*, 71:1–37, 2011.

[40] Sheldon L. Glashow. Partial-symmetries of weak interactions. *Nuclear Physics*, 22(4):579 – 588, 1961.

[41] A. Salam and J.C. Ward. Electromagnetic and weak interactions. *Physics Letters*, 13(2):168 – 171, 1964.

[42] Steven Weinberg. A model of leptons. *Phys. Rev. Lett.*, 19:1264–1266, Nov 1967.

[43] Peter W. Higgs. Broken symmetries and the masses of gauge bosons. *Phys. Rev. Lett.*, 13:508–509, Oct 1964.

[44] F. Englert and R. Brout. Broken symmetry and the mass of gauge vector mesons. *Phys. Rev. Lett.*, 13:321–323, Aug 1964.

[45] G. S. Guralnik, C. R. Hagen, and T. W. B. Kibble. Global conservation laws and massless particles. *Phys. Rev. Lett.*, 13:585–587, Nov 1964.

[46] M W Grunewald(ed). Precision electroweak measurements and constraints on the standard model. Technical Report CERN-PH-EP-2010-095, CERN, Dec 2010. Comments: 18 pages, Prepared from Contributions to the 2010 Summer Conferences.

[47] Electron performance measurements with the ATLAS detector using the 2010 LHC proton-proton collision data. *The European Physical Journal C - Particles and Fields*, 72:1–46, 2012. 10.1140/epjc/s10052-012-1909-1.

[48] Measurements of the photon identification efficiency with the ATLAS detector using 4.9 fb^{-1} of *pp* collision data collected in 2011. Technical Report ATL-COM-PHYS-2012-408, CERN, Geneva, Apr 2012. internal note, not yet reviewed.

[49] Steven Weinberg. Implications of dynamical symmetry breaking. *Phys. Rev. D*, 13:974–996, Feb 1976.

[50] Chris Quigg and Robert Shrock. Gedanken worlds without Higgs fields: QCD-induced electroweak symmetry breaking. *Phys. Rev. D*, 79:096002, May 2009.

[51] Michael E. Peskin and Dan V. Schroeder. *An Introduction To Quantum Field Theory (Frontiers in Physics)*. Westview Press, 1995.

[52] J. Beringer et al. *Phys. Rev. D*, 86:010001, 2012.

[53] Christopher T. Hill and Elizabeth H. Simmons. Strong dynamics and electroweak symmetry breaking. *Physics Reports*, 381(4-6):235 – 402, 2003.

[54] J. Erler and P. Langecker. Electroweak model and constraints on new physics. *Eur. Phys. J. C*, 15:95–109, 2000. 10.1007/BF02683406.

[55] Michael E. Peskin and Tatsu Takeuchi. Estimation of oblique electroweak corrections. *Phys. Rev. D*, 46:381–409, Jul 1992.

[56] Thomas Appelquist, Dimitra Karabali, and L. C. R. Wijewardhana. Chiral hierarchies and flavor-changing neutral currents in hypercolor. *Phys. Rev. Lett.*, 57:957–960, Aug 1986.

[57] Christopher T. Hill. Topcolor assisted technicolor. *Physics Letters B*, 345(4):483 – 489, 1995.

[58] Kenneth Lane and Estia Eichten. Natural topcolor-assisted technicolor. *Physics Letters B*, 352(34):382 – 387, 1995.

[59] Kenneth Lane and Estia Eichten. Two-scale technicolor. *Physics Letters B*, 222(2):274 – 280, 1989.

[60] Kenneth Lane and Stephen Mrenna. Collider phenomenology of technihadrons in the technicolor straw man model. *Phys. Rev. D*, 67:115011, Jun 2003.

[61] Kenneth Lane. Technihadron production and decay in low-scale technicolor. *Phys. Rev. D*, 60:075007, Sep 1999.

[62] Gary J. Feldman and Robert D. Cousins. Unified approach to the classical statistical analysis of small signals. *Phys. Rev. D*, 57:3873–3889, Apr 1998.

[63] A L Read. Presentation of search results: the CL s technique. *Journal of Physics G: Nuclear and Particle Physics*, 28(10):2693, 2002.

[64] Observation of an excess of events in the search for the Standard Model Higgs boson in the gamma-gamma channel with the ATLAS detector. Technical Report ATLAS-CONF-2012-091, CERN, Geneva, Jul 2012.

Appendix A

SUPPLEMENTARY PLOTS
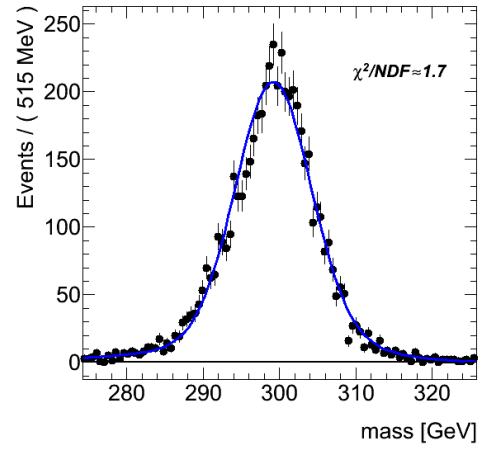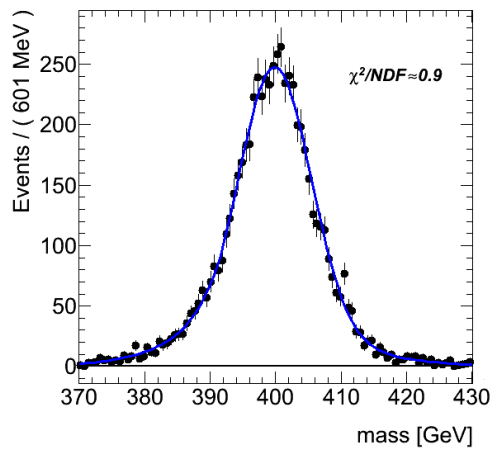
A.1   LSTC search
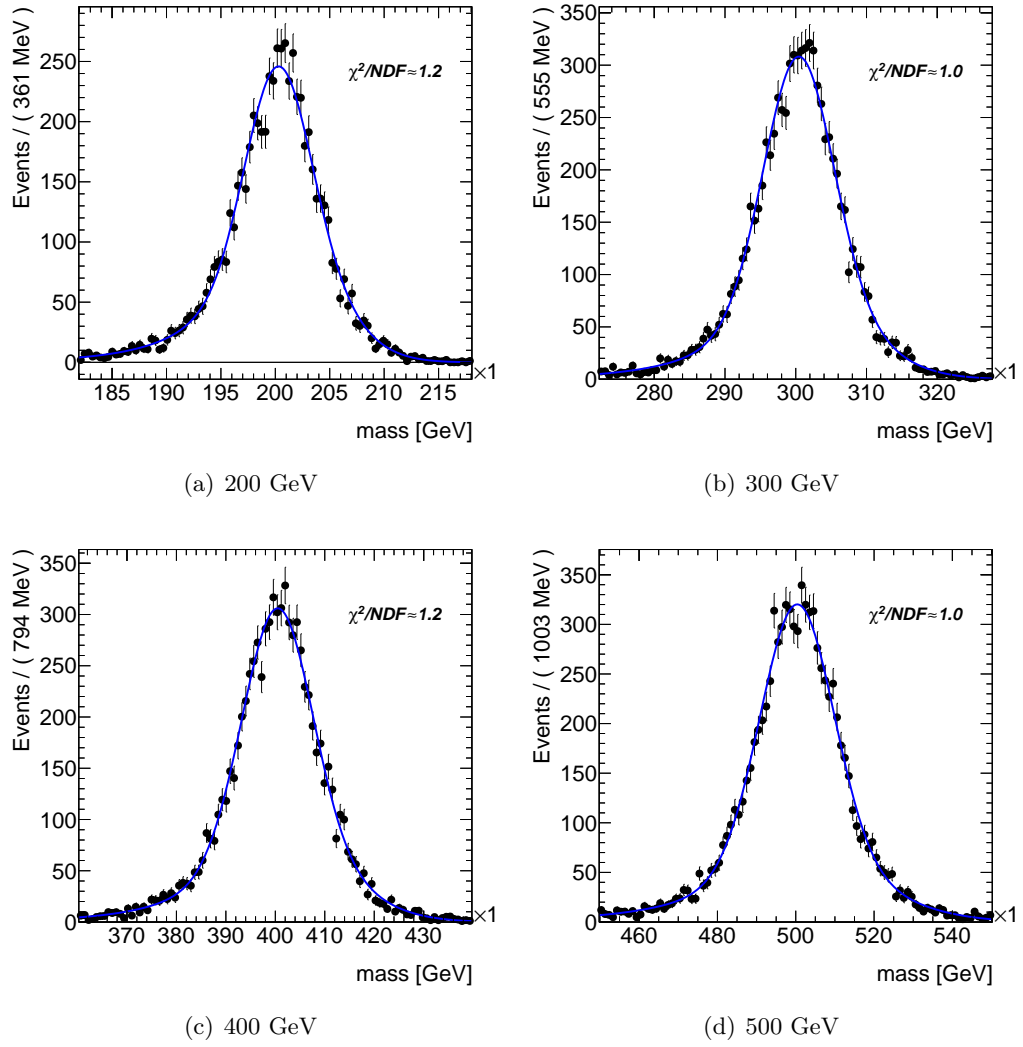
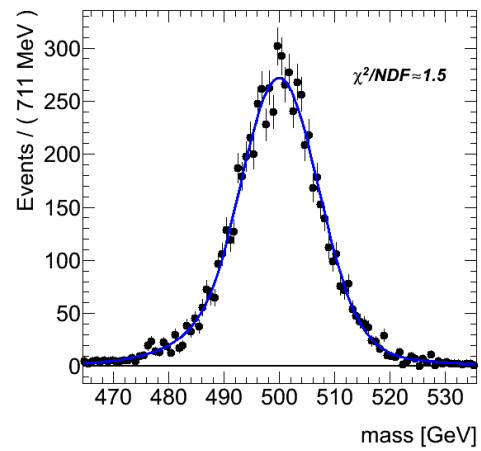Figure A.1: Fits of LSTC MC signal distributions from the muon channel.
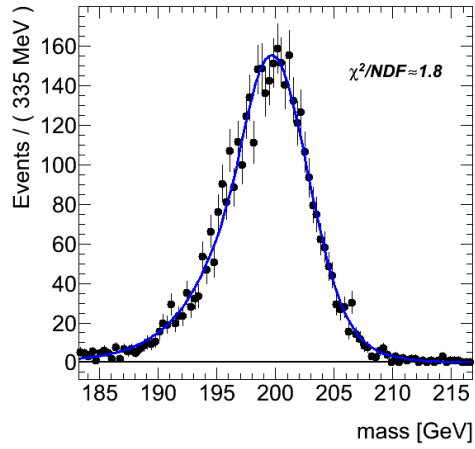
(a) 200 GeV

(b) 300 GeV

(c) 400 GeV

(d) 500 GeV

Figure A.2: Fits of LSTC MC signal distributions from the electron channel.